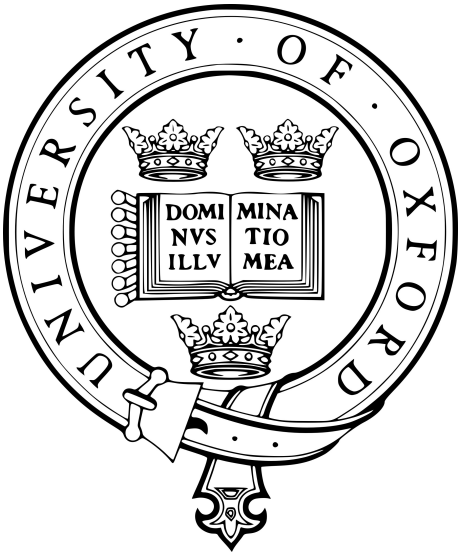


# Colloidal particles for confocal microscopy and optical tweezing

Yanyan Liu

New College

University of Oxford

Supervisor: Professor Roel P. A. Dullens

A thesis submitted for the degree of

*Doctor of Philosophy*

Trinity Term 2017

# Abstract

A novel colloidal model system is developed for the purpose of achieving simultaneous three-dimensional (3D) confocal imaging and optical tweezing of impurity probe particles embedded in a dense material of colloidal host particles. First, the colloidal host particles are developed from 3-trimethoxysilyl-propyl-methacrylate (TPM), and the solvent mixture is tuned to match the refractive index and the density of the particles. A sedimentation-diffusion equilibrium profile of the TPM particles was imaged in 3D to establish suitability of the system for 3D confocal laser scanning microscopy, and to study its phase behaviour and particle dynamics. Then, core-shell particles, which consist of a high refractive index core and a TPM shell, are synthesised to be used as the impurities. The versatility of the two-step coating procedure with TPM has been demonstrated on several core materials, and the optical properties of the core-shell particle are established using digital holographic microscopy and their optical trapping strengths. Together with the TPM host particles, the core-shell particles are shown to be suitable impurity probes in dense colloidal materials, as they can be manipulated using optical tweezers in all three-dimensions, whilst the structure and dynamics of the surrounding host particles can be imaged simultaneously using fast confocal laser scanning microscopy. Subsequently, to demonstrate the capability of the TPM-based colloidal model system, the depletion potential of a pair of core-shell probe particles embedded in a sea of TPM host particles has been measured using optical tweezing. This is derived from comparing the direct pair potential between the core-shell particles in a TPM refractive index matching solvent, and the potential of mean force for the core-shell particles embedded in a dense fluid region of the TPM host particles. Direct visualisation of the liquid structures of the TPM host particles in the binary system around the probe particles has been linked to the form of the depletion potential, and its oscillatory nature as a function of the particle separation. Lastly, the formation of colloidal dumbbell particles is discussed. The dumbbell formation has been rationalised in terms of the total surface energy of droplet formation on spherical surfaces and the calculations are compared with experimental results from coating various seed particles with TPM. Using optically anisotropic dumbbell particles and tuning the refractive index of the dispersion medium, a preliminary two-trap experiment has been conducted which shows unusual trapping behaviour when a time-delayed feedback trapping trajectory has been applied.

# Declaration

This thesis is submitted for the degree of Doctor of Philosophy in Physical and Theoretical Chemistry at the University of Oxford. No part of this thesis has been accepted or is currently being submitted for any degree, diploma, certificate, or other qualification in this University or elsewhere. This thesis is wholly my own work, except where indicated.

# Contents

**Abstract** **i**

**Declaration** **iii**

**1 Introduction** **1**

1.1 Colloidal model systems . . . . . 2

1.2 Optical tweezing of colloidal systems . . . . . 3

1.3 Three-dimensional imaging and optical tweezing in colloidal systems . . . . . 3

1.4 Scope of the thesis . . . . . 4

**2 Background and experimental methods** **7**

2.1 Colloids . . . . . 8

2.2 Synthesis of colloidal particles . . . . . 8

2.3 Properties of colloidal particles . . . . . 9

2.3.1 Particle interactions . . . . . 9

2.3.2 Brownian motion . . . . . 12

2.4 Experimental methods . . . . . 15

2.4.1 Particle characterisation . . . . . 15

2.4.2 Optical microscopy . . . . . 18

2.4.3 Optical Tweezing . . . . . 21

2.4.4 Particle detection and Image analysis . . . . . 23

**3 Colloidal TPM particles for three-dimensional confocal microscopy** **25**

3.1 Introduction . . . . . 26

3.2 Background . . . . . 27

3.2.1 TPM Synthesis pathway . . . . . 27

3.2.2 Three-dimensional confocal scanning microscopy . . . . . 28

3.2.3 Particle stabilisation in non-polar solvents . . . . . 29

3.3 Experimental methods . . . . . 30

3.3.1 Materials . . . . . 30

3.3.2 Particle Synthesis . . . . . 30

3.3.3 TPM characterisation using SLS . . . 31
3.3.4 Refractive index determination . . . 31
3.3.5 Solvent transfer . . . 32
3.3.6 Confocal microscopy and image analysis . . . 34
3.4 Results and discussion . . . 34
3.4.1 TPM Synthesis and characterisation . . . 34
3.4.2 Refractive index of TPM particles . . . 37
3.4.3 Confocal microscopy study of sedimentation equilibrium of TPM . . . 38
3.4.4 Dynamics of TPM particles as a function of height . . . 44
3.5 Conclusions . . . 46

**4 Core-shell particles for simultaneous three-dimensional imaging and optical tweezing 47**
4.1 Introduction . . . 48
4.2 Experimental methods . . . 49
4.2.1 Materials . . . 49
4.2.2 Preparation of seed particles . . . 50
4.2.3 Core-shell particle synthesis . . . 50
4.2.4 Digital holographic microscopy . . . 51
4.2.5 Confocal microscopy and optical tweezing . . . 51
4.3 Results and discussion . . . 52
4.3.1 Particle characterisation . . . 52
4.3.2 Controlling core size and shell thickness . . . 55
4.3.3 Digital holographic microscopy and optical trapping . . . 58
4.3.4 Simultaneous three-dimensional confocal microscopy and optical tweezing . . . 59
4.4 Conclusions . . . 62

**5 Direct measurement of the depletion potential in a binary mixture 65**
5.1 Introduction . . . 66
5.2 Background . . . 67
5.2.1 Pair potential . . . 67
5.2.2 Depletion interaction . . . 68
5.2.3 Potential of mean force . . . 69
5.3 Experimental methods . . . 71
5.3.1 Sample preparation . . . 71
5.3.2 Optical tweezing and confocal microscopy . . . 71
5.3.3 Image processing . . . 72
5.4 Results and discussion . . . 73
5.4.1 Direct pair potential measurement . . . 73
5.4.2 Potential of mean force measurement . . . 76

5.4.3 Depletion potential . . . 78
5.4.4 Structure of the host particles . . . 79
5.5 Conclusions and outlook . . . 82

**6 Development of optically anisotropic dumbbells 85**
6.1 Introduction . . . 86
6.2 Background . . . 87
6.2.1 Surface energy of a droplet . . . 87
6.2.2 Optical trapping of optically Janus dumbbells . . . 89
6.3 Experimental methods . . . 89
6.3.1 MF-TPM dumbbell synthesis . . . 89
6.3.2 Titania-TPM dumbell synthesis . . . 90
6.3.3 TPM-TPM particle synthesis with PVP . . . 90
6.3.4 Optical tweezing of MF-TPM dumbbell particles . . . 90
6.4 Results and discussion . . . 91
6.4.1 Surface energy . . . 92
6.4.2 Effect of total TPM volume on surface energy . . . 95
6.4.3 Effect of seed particle size on surface energy . . . 96
6.4.4 Effect of contact angle on surface energy . . . 96
6.4.5 Total surface energy as a function of droplet number . . . 99
6.4.6 Optical tweezing of dumbbell particles . . . 99
6.5 Conclusion and outlook . . . 102

**Appendix 105**
A List of abbreviations . . . 105
B Surface energy calculation derivations . . . 107
C Description of videos . . . 109

**Bibliography 122**

**List of publications 123**

**Acknowledgements 125**

# Chapter 1

# Introduction

Pure materials are rarely found in nature. Almost all materials contain some level of impurities, which either occur naturally or have been introduced to modify the properties of the product or process [1–3]. A large amount of effort has been put into the study of many of these altered processes, as they are crucial to many topics such as polymer processing [4], mineralogy [5], pharmaceutical industry [6], semiconductor [7], and protein crystallisation [8]. The presence of impurities strongly affects the macroscopic properties of a material. For instance in crystallisation [9–13], impurities directly determine the crystal grain size, which is related to the strength the material [14–18]. With the increasing addition of impurities in a relatively large crystal, the crystallites decrease in size and the material strengthens (Hall-Petch effect) [14, 15]. Yet if the grains continue to decrease in size, the material will eventually decrease in strength (reverse Hall-Petch effect) [16–18]. As such, the size of grains is crucial for explaining phenomena such as superplasticity and embrittlement [1, 3, 19].

In order to exploit the effect of impurities on the properties of materials, and for the designing of new materials, we need to understand the fundamental reasons behind the structural and dynamic processes in materials containing impurities. These include systems containing dopants [19], precipitates [20]) or solute atoms [1]. Although impurities are widely found in nature, long standing problems in condensed matter such as crystallisation and glass formation have typically been studied in 'pure' or single-component systems [1, 21, 22]. The presence of impurities can promote, frustrate or suppress crystallization completely (glass formation) [9–12]. This means that the properties of materials can be tuned, by the addition of impurities, from large crystal grains to polycrystalline systems (powders) with smaller grains and finally to glasses whose grain size is on the order of the particle size. Therefore by controlling the impurity quantity, a new perspective can be gained on the interplay between crystallisation, polycrystallinity and glass formation.

However, because the impurities in crystals, powders and glassy systems are always embedded in

dense bulk phases, it is cumbersome to study them experimentally. This has been done in atomic and molecular crystals and glasses using techniques such as high resolution transmission electron microscopy [23] and scattering experiments [24–26]. However due to the short length and time scales in atomic and molecular systems, direct real-time imaging of the structure and the dynamics is very difficult.

## 1.1 Colloidal model systems

Colloidal dispersions, in which particles of the size range between $\sim 10nm$ and several microns are dispersed in a continuous solvent phase, provide a unique model system for studying impurities in crystals and liquids. Colloids are widely found in nature, e.g. in opals, crystals and bacterial suspensions, but also in many industrial processes such as paint, toothpaste and India ink. Other examples include emulsions, gels and aerosols. The term 'colloid' was first coined by Thomas Graham in 1861 [27], and is derived from the Greek word for glue ('$\kappa o \lambda \lambda \alpha$'). Graham deduced the approximate upper and lower size bounds of the microparticles in his 'pseudosolutions' from their slow diffusion rates and their lack of sedimentation. These are now used as the defining length scales for the colloidal domain, and is not specific to any material.

Conveniently, colloids can be used as a model system for atomic and molecular matter. Despite their larger size, they are still small enough to undergo Brownian motion. This was first discovered by the botanist Robert Brown in 1827 [28], who described the random motion of the colloidal particles induced by collisions with the thermally agitated solvent molecules [29]. As such, Brownian motion enables the colloidal particles to explore all available phase space, as is the case in atomic and molecular systems, and so they exhibit similar phase behaviours as their atomic counterparts [30, 31]. Furthermore, the shapes and materials of colloids can be adjusted during their synthesis, giving a wide variety of shapes including rods [32, 33], cubes [34], peanuts [35], and dumbbells [36, 37]. Likewise the particle interaction can be altered, via the addition of salt or depletant [29], or by external magnetic or electric fields [38–41], or by designing patchy particles with specific directional interactions [42]. Together, colloids offer a wide range of choice for the study of fundamental issues such as self-assembly [37, 43], melting transitions [38, 44], liquid crystalline phases [13], and glasses [45].

Aside from using colloids as model systems, they also have a wide range of applications in food processing [46,47], optical materials [48], drug delivery [49], and physiology [50]. In particular, colloidal systems are very promising for the development of photonic materials [51, 52]. It is also highly relevant for the production of ceramic films with well-defined properties [53]. The structure of the colloidal crystal is fundamental to both of the above examples, and therefore precise control of the self-assembly of the colloids is crucial. As self-assembly in colloidal systems occur via nucleation, recrystallisation and

crystal growth, it is important for us to understand the role that the impurities play so that new photonic and ceramic materials can be successfully designed and manufactured in the future.

## 1.2 Optical tweezing of colloidal systems

Another key advantage of studying colloidal materials, e.g. colloidal solids, is that they are considered as "soft" materials [29] and can be easily manipulated using a range of external fields including optical tweezers [54]. The 'softness' of colloidal materials can be rationalised by examining the Young's modulus for an atomic crystal and for a colloidal crystal. Since the Young's modulus scales as an energy per unit volume, if we consider both the energy and the length scale of the two systems, we can see that for an atomic system, the typical energy is $\sim 1eV$ with a length scale in $\mathring{A}$ngstroms, whereas for a colloidal system, the typical energy of the order $k_BT$ with a length scale in microns. By comparison, the Young's modulus for a colloidal material is smaller by approximately a factor of $10^{12}$, therefore it is much easier to shear and distort colloidal systems than their atomic counterparts. Hence we can for example use a highly focused laser beam (an optical tweezer) to trap and manipulate particles inside dense colloidal materials. Indeed, optical tweezing has been used extensively in soft matter to study a wide range of problems, including optical sorting [54] and microrheology [55, 56]. This is particularly exciting for the study of the effect of impurities in bulk, as the impurity particles can be trapped and manipulated using optical tweezers to exert small external forces on their colloidal host material. The effects of this on the surrounding colloidal material provide insight into the role of impurities in crystal growth and impurity drag [13, 57], and glass formation [22, 58–60].

## 1.3 Three-dimensional imaging and optical tweezing in colloidal systems

Given their relatively large length scale, colloidal systems can be readily imaged using optical microscopy [61]. Whilst this is straightforward in 2D, even in the presence of impurities [62, 63], it is much more challenging in 3D. This is particularly problematic for densely packed colloidal systems, partly due to the relatively poorer resolution in $z$ (along the optical axis), and partly due to the interference of the out of focus light with the signals in the imaging plane [61]. However this is vastly improved by matching the particle's refractive index to the solvent mixture, and combined with powerful 3D imaging techniques such as confocal microscopy, we are able to study directly the complex structural and dynamic properties inside a 3D colloidal material. This single-particle resolution in real time and space allows unprecedented access to a range of condensed matter phenomena such as crystallisation, glass jamming, and gels [9, 11, 12, 22].

While both 3D confocal imaging and 3D optical tweezing have been achieved individually in colloidal systems [54, 61, 64], combining these techniques to achieve simultaneous yet independent imaging and optical manipulation in impurity doped colloidal systems is very challenging. One method of establishing this is by positioning two objectives nose-to-nose on opposite sides of the sample, where one provides the optical trapping and the other the imaging [65]. This mechanically decouples the trapping plane and the imaging plane, thereby allowing independent imaging of optically trapped colloidal particles in 3D. However this setup has limited access to the sample and requires a thin sample volume. Other approaches include the use of wavefront engineering and computer feedback [66–68], and digital refocusing [69, 70], although their application to simultaneous 3D imaging and optical tweezing is also limited. Recently this problem has been elegantly resolved by refocusing of the imaging plane remotely and thus separating it from the trapping plane [71]. This enabled decoupled and simultaneous three-dimensional imaging and optical manipulation when imaging through a single objective.

In addition, however, simultaneously and independently performing 3D confocal imaging and tweezing also puts extremely high demands on the colloidal system. The problem arises from the fundamental conflicting requirements for 3D confocal imaging and optical tweezing [65, 71–74]. While 3D visualisation requires optical transparency of the colloidal sample, optical tweezing and manipulation requires a refractive index mismatch between the probe particles and solvent. Furthermore, it is desirable for the particle interactions between the probe particles and its surrounding host particles to be identical. A possible solution would be a core-shell probe particle that has a shell material chemically identical to that of the host colloidal particles. Ideally we require the core's size and refractive index to be tuned sufficiently for reliable optical trapping, yet interferes minimally with the visualisation of the surrounding host sample, whilst the shell remain optically transparent. If this could be be achieved then it provides a very rewarding approach and opens up a huge range of possibilities for investigating the relation between the presence of impurities and the (micro)mechanical properties of glasses, polycrystals, and many other impurity doped colloidal systems.

## 1.4 Scope of the thesis

The central aim of this thesis is to develop a colloidal model system that enables simultaneous 3D confocal imaging and optical tweezing of impurity probe particles embedded in dense colloidal materials. Subsequently the application of this colloidal model system is explored, along with the development and optical tweezing properties of optically anisotropic dumbbell particles.

We begin in Chapter 3 by introducing the key concepts and experimental techniques that underly the experiments presented in this thesis. Particular focus has been given to confocal microscopy and

optical tweezing, and the relevant colloidal physics, including colloidal synthesis, particle interactions and dynamics. The experimental techniques used for the characterisation of the colloidal particle have also been introduced, along with image processing and particle tracking.

Chapter 3 describes the development of the colloidal host system for the purpose of 3D confocal imaging, using particles made from 3-trimethoxysilylpropylmethacrylate (TPM). Factors influencing the synthesis of the TPM particles are investigated, and the particles are characterised using a combination of optical microscopy, static light scattering (SLS), and scanning electron microscopy (SEM). The process required for creating a refractive index and density matching TPM colloidal system is detailed, and its imaging capability is demonstrated by the observation of the sedimentation-diffusion equilibrium profile in 3D.

Next, the development of core-shell particles with TPM shells and tuneable core material and shell thickness is reported in chapter 4. The core-shell probe particles are synthesised in a two-step coating of the core particles using TPM via an intermediate raspberry particle stage [37], and we demonstrate the independent control of the core size and the shell thickness. In addition, the adjustable optical properties of the core particle is shown using different core materials and they are characterised using digital holographic microscopy (DHM) and optical tweezing. The suitability of the core-shell particles as probe particles when embedded in a refractive index matching dispersion of TPM host spheres is demonstrated by dragging a single core-shell particle in several trajectories through a dense crystalline sample, whilst the surrounding 3D system is imaged by confocal microscopy.

Chapter 5 make use of the TPM-based binary colloidal system that has been developed in chapters 3 and 4 to measure the total interaction potential (of mean force) between a pair of large core-shell particles embedded in a dense fluid phase of small TPM spheres. This is contrasted with the direct pair potential measured for a pair of core-shell particles immersed in a TPM refractive index matching medium. Both potentials were obtained by measuring the displacement of the core-shell particles from the expected trap separation distance and the trapping strengths. The form of the depletion potential between the particle pair is also obtained using the direct pair potential and the potential of mean force. Lastly, the independent yet simultaneous trapping and imaging of the binary system in 3D allows for direct visualisation of the host particle structure around the core-shell particles. These are used to explain and interpret the form of the depletion potential of probe particles embedded in a dense fluid phase of host particles.

Lastly, in Chapter 6, the formation of multi-lobed raspberry particles and single-lobed dumbbell particles are examined. By considering the total surface energies of these systems, we compare the numerical calculations with experimental outcomes, and attempt to rationalise the formation of these particle morphologies. Based on these results, optically anisotropic dumbbell particle were developed.

These are then dispersed in a solvent with intermediate refractive index to the two sides of the dumbbell particle and are subjected to optical tweezing experiments. As well as displaying unusual trapping behaviour of the dumbbell particle, preliminary results from a time-delay feedback experiment using two optical traps show unusual rotational particle dynamics, which may provide insight on the mutual information between the particle trajectory and the trap's position.

# Chapter 2

# Background and experimental methods

ABSTRACT

This chapter introduces some of the key concepts underlying colloid science and the experiments presented in this thesis. In particular, colloidal synthesis, particle interactions and dynamics are discussed. The principles of experimental techniques such as confocal microscopy and optical tweezing are also described here, along with the other techniques used for the characterisation of colloidal particles, including static light scattering, digital holographic microscopy and scanning electron microscopy. Finally, image analysis such as particle detection and tracking are also introduced.

## 2.1 Colloids

Colloids, or colloidal dispersions, is a biphasic system which consists of a finely dispersed phase, the colloidal particles, in a continuous dispersion medium, the solvent. Colloidal particles have a typical size range between $\sim 10nm$ and several microns. Colloidal systems are widely found in nature, such as in opals, clays and fog, as well as in many industrial products, e.g. paint, toothpaste and ice-cream. In this thesis, we focus on the solid-like colloidal particle that are dispersed in a continuous liquid medium.

## 2.2 Synthesis of colloidal particles

Fundamentally, particles in the colloidal domain can be prepared using two approaches: dispersion and condensation [29, 75]. Dispersion is a top-down method, where macroscopic materials are broken down into smaller components, e.g. by comminution, emulsification or suspension-polymerisation [76]. In contrast, condensation is a bottom-up method, where molecular species nucleate and form a new phase by exceeding the solubility limit. Two of the most commonly used strategies of synthesising colloidal particles via condensation are: emulsion polymerisation and dispersion polymerisation.

Both emulsion and dispersion polymerisation grow polymers from monomers that are weakly soluble in a continuous medium, which contains the dissolved initiator [76]. As the polymer grows, its solubility decreases, until a critical molecular mass is reached, triggering spontaneous nucleation (precipitation). The nuclei grow by accumulating polymers from the continuous phase, or by reacting directly with the remaining monomers using the free radicals on their surface. Emulsion polymerisation is typically carried out in aqueous mediums and the particles formed are usually stabilised by electrostatic interactions (See Section 2.3.1). In contrast, dispersion polymerisation is typically conducted in non-aqueous mediums, and steric stabilisers are usually required to prevent particle coagulation.

The size-distribution of a batch of particles depends on the length of time that nucleation occurs in a given reaction. This time-window is controlled by the duration that the concentration of the precipitating species stays above the critical supersaturation limit [77]. At the start of a reaction, the insoluble polymer species rapidly increases in concentration until the critical saturation level is reached (Fig. 2.1). At this point, nucleation occurs spontaneously whilst the polymer concentration continues to increase, which in turn rapidly increases the rate of nucleation. This continues until both rates are balanced, near the maximum limit of supersaturation. After this, the polymer concentration starts to fall, eventually taking

it below the critical supersaturation level as shown in Fig. 2.1. This causes the nucleation to cease. The concentration of the polymer continues to fall in order to feed the growth of the nuclei formed. This continues until the concentration of the polymer approaches its solubility point in the medium, as indicated by the saturation line in Fig. 2.1, where further particle growth ceases. The nuclei formed can be grown in size indefinitely, providing that the subsequent addition of reactants maintains the concentration of the polymer below the nucleation threshold and above the critical solubility point. As such, the number of particles synthesised in a reaction is determined by the initial nucleation stage, and the final size of the particles is determined by the availability of the polymer above the saturation concentration. Therefore the smaller the time-window for the nucleation event, the more uniform the particles will be in size (Fig. 2.1). Typically monodisperse colloids are classified as having a polydispersity (standard deviation divided by mean size) of between 2% and 6% [78].

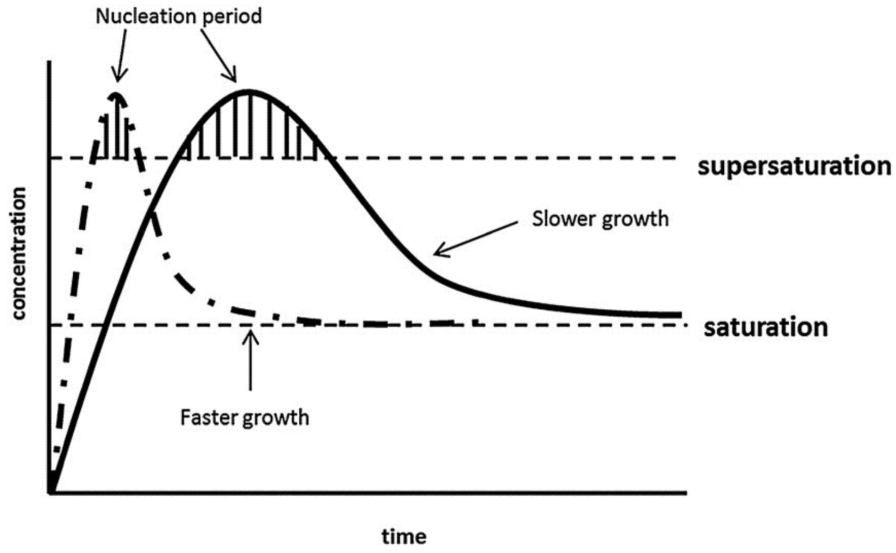


*Figure 2.1: LaMer diagram for two different courses of nucleation and growth [79]. Shorter nucleation periods lead to more monodisperse particles.*

## 2.3 Properties of colloidal particles

### 2.3.1 Particle interactions

Colloidal particles interact in different ways, depending on the exact system. Solvation and steric forces may also contribute towards the interaction between colloids. The most common description of colloidal interactions is the Derjaguin-Laudau-Verwey-Overbeek (DLVO) theory, which describes the pair potential

of two interacting particles $W_{DLVO}$ as a function their separation distance $r$:

$$W_{DLVO}(r) = W_{vdW}(r) + W_{el}(r). \tag{2.1}$$

The interplay between the van der Waals attraction, $W_{vdW}$, and the electrostatic repulsion, $W_{el}$, determines the total interaction of particles in a colloidal dispersion.

**Van der Waals potential**

The van der Waals interaction originates from the non-permanent, fluctuating and instantaneously induced dipoles between two neighbouring atoms or molecules. It has the form of $w(r) \propto -1/r^6$ and is short ranged. To estimate the van der Waals interaction between two large particles, Hamaker (1937) assumed pairwise additivity of all the dispersion forces between the molecules in the particles, and neglected retardation [80]. For two identical spheres of radius $R$ separated by a surface to surface distance $r$, where $r << R$, the van der Waals potential is:

$$W_{vdW}(r) = -\frac{AR}{12r}, \tag{2.2}$$

where A is the Hamaker constant [81]. Note that the summation of molecular pair potentials resulted in a dependence on the particle size, and caused the interaction to decay more slowly as a function of the separation distance (c.f. $1/r^6$). Also, for two identical bodies dispersed in a medium, the van der Waals force is always attractive due to a positive Hamaker constant A.

To account for the non-validity of the additivity assumption in condensed media, Liftshitz (1956) used quantum field theory to treat the large bodies as continuous media [81]. The van der Waals expressions that were derived previously remain valid, however the Hamaker constant is now calculated in terms of the bulk properties of the materials (i.e. dielectric constants and refractive indices). For instance, for two identical phases 1 interacting across a medium 2, the Hamaker constant [81] is:

$$A = \frac{3}{4}k_BT\left(\frac{\epsilon_1 - \epsilon_2}{\epsilon_1 + \epsilon_2}\right)^2 + \frac{3h\nu_e}{16\sqrt{2}}\frac{(n_1^2 - n_2^2)^2}{(n_1^2 + n_2^2)^{3/2}}. \tag{2.3}$$

In non-polar systems, the role of the dielectric term is only of the order of 1% [82], reducing Eq. 2.3 to:

$$A \approx \frac{3h\nu_e}{16\sqrt{2}}\frac{(n_1^2 - n_2^2)^2}{(n_1^2 + n_2^2)^{3/2}}. \tag{2.4}$$

This means that if index-matching is achieved across phase 1 and medium 2, then the van der Waals interaction between two bodies of phase 1 can be minimised.

### Eletrostatic potential

The surfaces of particles are often charged, especially in high dielectric mediums, by rapid dissociation of surface groups or adsorption of ions. The electrostatic repulsion acts against the van der Waals attraction and can prevent particles from aggregating. For two point charges ($q_1$ and $q_2$) separated by a distance $r$ in a medium of dielectric constant $\epsilon_r$, the Coulomb potential is $w(r) = (q_1 q_2)/(4\pi\epsilon_0\epsilon r)$. From this we would expect a long range interaction decaying as a function of $1/r$. However the electrostatic forces between particles are screened by counter-ions present in the medium. Some are bound closely to the particle surface in a Stern layer, whilst others are bound loosely in the diffuse electric double layer. The typical length scale for the decay of the surface charge is characterised by the Debye length, $\kappa^{-1}$ [29, 81]. For two spherical particles of size $\sigma$, separated by a distance $r$, the screened electrostatic potential is [83]:

$$W_{el}(r) = \begin{cases} +\infty, & \text{for } r \leq \sigma. \\ Z^2 k_B T \lambda_B \dfrac{\exp(\kappa\sigma)}{(1+\kappa\sigma/2)^2} \dfrac{\exp(-\kappa r)}{r}, & \text{otherwise.} \end{cases} \tag{2.5}$$

Here, $Z$ is the number of charges at the particle surface, and $\lambda_B$ is the Bjerrum length, which is the distance when electrostatic interactions between two charges is of the order $k_B T$. Note that Eqn. 2.5 has the form of a Yukawa potential, with $W \propto e^{-mr}/r$ for separation larger than the particle diameter, and infinite repulsion at contact, reflecting the hard-sphere nature at contact.

As the ionic strength of the solution increases, the electrostatic interaction is better screened and the Debye length falls. Without the presence of the electric double-layer, the repulsive interaction between two charged particles act over much larger distances, as is sometimes seen in low dielectric mediums [84]. However in a high dielectric and highly ionic media, the diffuse double layer screens the particle surface effectively, making the particles appear ‘neutral’ over long distances. Yet as soon as the particles are brought close enough for their charged double-layers to interact, repulsive forces will be experienced.

### 2.3.2 Brownian motion

Brownian motion of colloidal particles was first observed in 1827 by the Scottish botanist Robert Brown whilst studying plant pollens [28]. It provided early evidence for the molecular kinetic theory, which predicted that the random movements of particles were caused by the collisions of molecules in the surrounding medium, due to thermal agitation. The theory of Brownian motion was formalised by Einstein in 1905 [85], and was subsequently confirmed by the experimental works of Perrin in 1908 [86].

Brownian motion is a stochastic process, therefore the mean of the total displacement is always equal to zero. However the mean of the square of the displacement depends on the number of steps taken by the particle, and is therefore proportional to time, $t$. For a very dilute suspension of colloids, the Brownian motion of a single particle in $n$ dimensions can be characterised by its mean-squared-displacement (MSD):

$$\langle r^2(t) \rangle = 2nD_0t, \tag{2.6}$$

where $D_0$ is the translational diffusion coefficient at infinite dilution, and $n$ is the dimensionality. Einstein has shown that the diffusion coefficient is given by the ratio of thermal energy and the friction coefficient $\xi$ [85]:

$$D_0 = \frac{k_BT}{\xi}. \tag{2.7}$$

For a spherical particle, $\xi = 6\pi\eta R$, with $\eta$ being the viscosity of the dispersion medium. Combining this with Eqn. 2.7, we get an expression for the diffusion coefficient, which is inversely proportional to the size of the particle and the viscosity of the solvent. This is known as the Stokes-Einstein equation [85]:

$$D_0 = \frac{k_BT}{6\pi\eta R}. \tag{2.8}$$

A useful way of quantifying the extent of Brownian motion by a particle is by defining the characteristic time scales. For translational diffusion in 3D, the Brownian time, $\tau_B$, represents the typical time needed for a particle to explore across its own diameter, $\sigma$,

$$\tau_B = \frac{\sigma^2}{6D_0} \sim \frac{\eta R^3}{k_BT}. \tag{2.9}$$

As well as translational diffusion, particles also undergo rotational diffusion. Analogous to trans-

lational diffusion (Eqn. 2.6), the rotational diffusion is characterised by the angular MSD:

$$\langle \theta^2(t) \rangle = 2nD_{0,r}t, \tag{2.10}$$

with $D_{0,r}$ the rotational diffusion coefficient, and $n$ the number of axes involved for the rotation. Eqn. 2.7 can also be applied to find the rotational diffusion coefficient, however, the rotational Stokes friction factor has to be used instead. For a sphere, $\xi_r = 8\pi\eta R^3$, and so the rotational diffusion coefficient is:

$$D_{0,r} = \frac{k_B T}{8\pi\eta R^3}. \tag{2.11}$$

Similarly for the rotational diffusion, the rotational relaxation time $\tau_R$ refers to the typical time required for a particle to significantly change from its initial orientation. It has the same particle radius dependence as its translational counterpart shown in Eqn. 2.9. For rotations in 3D, the rotational relaxation time of a freely diffusing particle is [87]:

$$\tau_R = \frac{1}{2D_{0,r}} \propto \frac{\eta R^3}{k_B T}. \tag{2.12}$$

Thus for a freely diffusing particle in water at room temperature with a radius $R = 1\mu m$, $\tau_B$ would be $\sim 0.8$s, and $\tau_R$ would be $\sim 3$s.

The thermal energy of a particle also competes with its gravitational energy so that a sedimentation diffusion equilibrium will form. The decay of the resulting particle density profile is characterised by the gravitational height, $z_0$, as:

$$z_0 = \frac{k_B T}{\Delta\rho v_p g}, \tag{2.13}$$

where $\Delta\rho$ is the density difference between the particle and the solvent, $v_p$ is the volume of the particle, and $g$ is the acceleration due to gravity. If $z_0$ is large, then the thermal energy of the colloidal particles keeps them in suspension. Otherwise, if $z_0$ is small, the particles would sediment towards the bottom of the sample chamber and its diffusion against gravity is limited.

**Phase behaviour**

Analogous to atomic and molecular systems, colloids also exhibit phase behaviour. As they undergo Brownian motion, they scan the phase space in a similar way to atoms and molecules, thus rendering

them thermodynamically equivalent to atoms and molecules. The interactions are typically given by a Yukawa potential, as seen in Eqn. 2.5.

In the case where the Debye length $\kappa^{-1}$ is much smaller than the particle diameter $\sigma$, the potential can be approximated by that of a hard-sphere system: the particles have zero interactions everywhere unless at the point of contact, where the potential becomes infinitely repulsive. This makes the hard-sphere phase transition athermal and entropy driven, and the sole control parameter is the number density $n$. Typically in colloidal systems, the particle number density is represented using the volume fraction $\phi$, which is related to the number density by $\phi = nv_p$, with $v_p$ being the volume of a particle. In terms of phase behaviour, the volume fraction can be considered as the inverse of temperature. Past simulations [88] have shown that the freezing and melting transitions of 3D hard sphere system occur at $\phi = 0.494$ and 0.545, respectively (Fig.2.2). Between $0.494 < \phi < 0.545$, both fluid and crystalline phases coexist, and providing that the system is at equilibrium, the crystal phase will persist from $\phi = 0.545$ until the maximal close packing of spheres at $\phi = 0.740$. In 1986, Pusey and van Megen successfully demonstrated the $\phi$-dependent phase behaviour in polymethylmethacrylate (PMMA) colloids [30], though a scaling factor was required to map the observed phase-transition points to those of an effective hard-sphere system.

In reality, however, all colloidal systems have varying degrees of softness depending on the particular form of the inter-particle potential [89]. A soft interaction increases the effective diameter of the particles and hence lowers the $\phi$ at which the freezing transition actually occur. Depending on the extent of the charge repulsion, the fluid phase may crystallise into body-centred-cubic crystals at large $\kappa^{-1}$ instead of the usual faced-centred-cubic crystals for small $\kappa^{-1}$ [90]. Finally, as well as the contribution from the soft interactions, particle polydispersity and non-sphericity can also alters the phase diagrams significantly [91, 92].

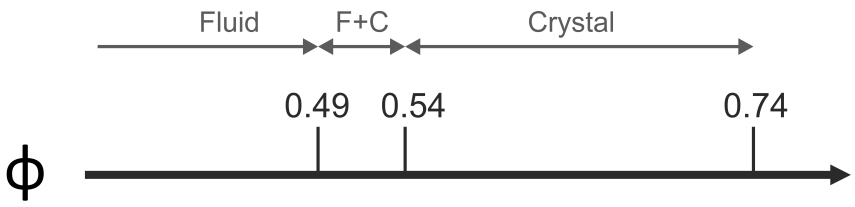


*Figure 2.2: Phase diagram for a 3D hard-sphere system.*

## 2.4 Experimental methods

In this thesis, we develop colloidal model systems for the use in microscopy (CLSM and brightfield) and optical tweezing experiments. We will first introduce the techniques used to characterise the colloidal particles (static light scattering, scanning electron microscopy, digital holographic microscopy), and then the main experimental techniques of confocal laser scanning microscopy and optical tweezing. Lastly, the method for image analysis and particle tracking are demonstrated.

### 2.4.1 Particle characterisation

#### Light scattering

Laser light scattering is one of the most widely used methods of collecting structural and dynamic data from colloidal suspensions [61,93–95]. It collects ensemble data and gives average information regarding the sample. There are two main types of light scattering experiments: static light scattering (SLS) and dynamic light scattering (DLS). SLS measures the intensity of the scattered light as a function of the scattering vector

$$\mathbf{k} = 4\pi n/\lambda \sin(\theta/2), \tag{2.14}$$

where $\theta$ is the scattering angle, $\lambda$ the wavelength of the incident light, and $n$ the positive integer spacings. SLS is particularly useful for elucidating the overall size and polydispersity of single particles. In comparison, DLS measures the fluctuation in the scattered light that is caused by Brownian motion of the particles, and provide information about the typical diffusion time as well as the average particle size. However it is worth noting that for larger and heavier particles with sedimentation rates similar or greater than their average Brownian time, the results from DLS becomes less reliable. Instead, information regarding their size and polydispersity can be deduced using SLS. A dilute sample is required so that the minima in the scattering pattern (Fig. 2.3) is not obscured by multiple scattering in the sample.

For a typical SLS experiment, a sample is dispersed in deionised water and diluted until minimal scattering is visible to the eye. ~2ml of this is added to a clean borosilicate glass tube (Fisherbrand 10x75mm), which is capped and inserted into the sample holder of the ALV/CGS-3 Compact Goniometer System. A SLS experiment is usually conducted for angles between $20 - 120^\circ$ at $1^\circ$ or $2^\circ$ intervals using a 632.8nm laser light source. Given that the particles in this thesis are mostly in the Mie scattering

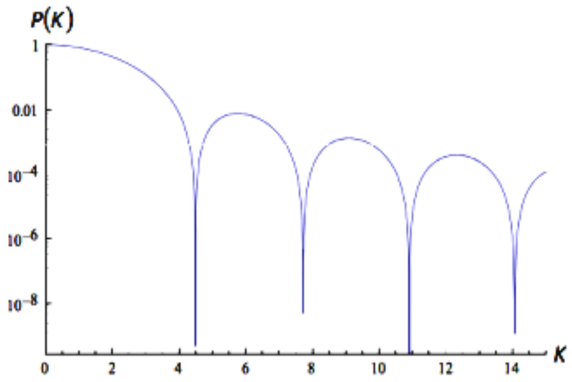


*Figure 2.3: A calculated example of the scattering pattern observed for a dilute sample of monodisperse spheres, showing the decay of the form factor $P(\boldsymbol{K})$ as a function of the scattering vector $\boldsymbol{K}$, which depends on the angle of observation [93].*

regime ($r \sim \lambda_{SLS}$), results from Mie-theory calculations are used to fit the experimental data by eye to find the average particle radius and polydispersity. The data from Mie calculations are provided using the Miescat4.exe software by Dr. A. Imhof (Utrecht University), which also gives results for the core-shell particle scattering.

### Scanning electron microscopy

Scanning electron microscopy (SEM) is typically used to observe objects in the colloidal size range. It uses a focused beam of high energy electrons to detect the surface topography of a sample. The beam is directed using magnetic lenses and the surface of the specimen is scanned systematically to generate a final image on the computer. The strength of the signal detected at each point reflects any topological or compositional differences that may exist in the sample. The use of the electron beam requires the SEM to operate under vacuum, therefore samples have to be thoroughly dried before imaging. Also, depending on the size of the particles and the surface conductivity, sputter-coating may be required to avoid over-charging of the surfaces and improve resolution. Two of the most common types of signal detection in SEM are: Backscattered electron (BSE) and Secondary electron (SE). BSE are the deflected primary electrons by the sample and are very high in energy, ideal for differentiating material compositions. SE is more suitable for studying the topography and surface of the samples, as they are formed by inelastic scattering and are much lower in energy.

All of the SEM images in this thesis are taken using a JSM-6010LV scanning electron microscope under high vacuum. The samples are prepared by placing a dilute droplet ($\sim 50\mu l$) onto a silicon chip of

5x5mm and is left to dry thoroughly before mounted on the sample holder. All images are taken using the InTouchScope software in SE imaging mode. When required, Quorum SC7620 Sputter Coater was used to deposite a thin layer of palladium coating of a few nanometers thick onto the sample prior to imaging.

### Digital Holographic Microscopy

Digital holographic microscopy (DHM) was first used by Lee et al. [96] to track and characterise individual colloidal particles in 3D. This technique was further advanced by Fung et al. to elucidate information for more complex particle geometries [97]. Fundamentally, in-line holographic microscopy requires shining a collimated beam of laser light onto the point-like particle, so that the scattered light from the particle can interfere with the unscattered laser beam to give an interference pattern. This is then magnified by the microscope objective and is recorded by the camera as a digital hologram (Fig. 2.4). The hololgrams are fitted computationally using the full Lorenz-Mie theory (HoloPy [97], and the radius, refractive index and the 3D position of the particle can be obtained [96].

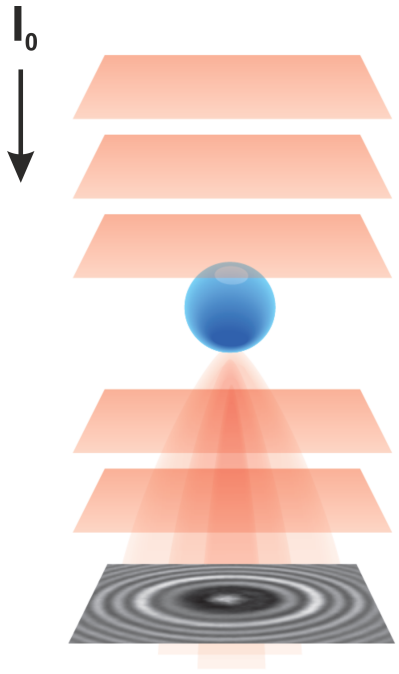


*Figure 2.4: Schematic diagram showing the principles of digital holographic microscopy. $I_0$ refers to the incident light, which is collimated and is represented here as propagating planes.*

The optics setup used here for DHM is a modified version of the setup shown in Fig. 2.8, where the confocal scanhead was replaced with the CMOS camera, and the Köhler illumination was swapped for a coherent laser beam ($\lambda$ =405nm). Typically a very dilute suspension of the colloids is prepared inside a borosilicate capillary tube and sealed with UV glue at both ends onto a glass slide. A single particle is

then trapped in a strong optical tweezing potential to minimise its Brownian displacement from the trap center. In order to reduce the background noise in the final hologram, a video of the hologram is taken (250fps) of a particle dragged along the x-direction at 1$\mu$m/s, which is then normalised by the median of all the frames. Next, the mean of all frames, with each frame centred on the center of the particle, is used for subsequent analysis using HoloPy software [97].

### 2.4.2 Optical microscopy

Optical microscopy provides real-time and real-space imaging of systems in the colloidal size-range, although the spatial resolution is limited by the Abbe diffraction limit. The minimal distance $d$ between two resolvable objects is given by:

$$d = \frac{\lambda}{2NA} = \frac{\lambda}{2n_f \sin(\theta)}, \tag{2.15}$$

where $\lambda$ is the wavelength of light, $NA$ the numerical aperture of the objective, $n_f$ the refractive index of the medium between the object and the lens, and $\theta$ is the half angle of the cone of light entering the objective. Typically $d$ is on the order of $\sim$ 250nm for a conventional brightfield microscope.

The basic setup of a microscope has changed little since its earliest creation in the 1600s [98]. The modern brightfield microscope normally consists of a light source, condenser lens, sample, objective, and observation. Modern brightfield setups make use of Köhler illumination so that the image of the light source is defocused in the sample plane and its conjugate plane, and that the sample is evenly illuminated and would give a high image contrast. One disadvantage of brightfield microscopy is that it is limited to thin or dilute samples only (e.g. in 2D), as light scattered from out of focus objects interferes with the scattered light from the objects in the imaging plane, hence decreasing the image quality. However brightfield remains an extremely useful tool for real-time observation of colloids, particular when used in combination with digital holographic microscopy (DHM) and optical tweezing (see Sections 2.4.1, 2.4.3, and 4.2.4).

In this thesis, all of the brightfield images were taken using a Olympus IX73 inverted microscope with Olympus 60x oil-immersion objective ($NA$ = 1.42). Typically an aqueous sample slide is prepared by sandwiching a 100$\mu l$ drop between two glass cover slips, and the image is recorded using Ximea Viewer V3.17.16 software.

### Confocal microscopy

Confocal Laser Scanning Microscopy (CLSM) is another type of optical microscopy, as it typically uses laser light sources with wavelengths in the visible light region. It combines the technique of confocal microscopy and point-by-point fluoresce illumination of the sample. Confocal microscopy uses two pinholes, one at the light source and one at the receiving source, to suppress the out-of-focus light in dense samples and thus improving the signal-to-noise ratio of the images. The out-of-focus light can also be greatly suppressed by refractive index matching of the particles with the solvent, thereby allowing 3D imaging. However in order to resolve the particles, fluorescent labelling of the sample is necessary. The scattered light from out of focus planes is further suppressed by illuminating the sample sequentially (point-by-point) with the excitation wavelength, so that only the florescent signals from the illuminated point is collected.

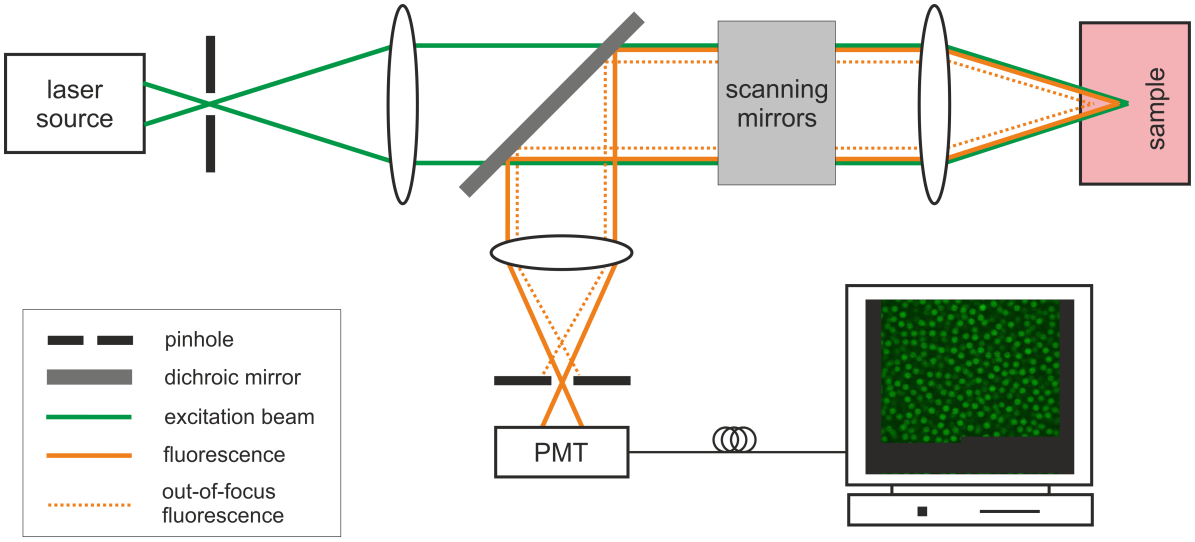


*Figure 2.5: Schematic of a typical laser scanning confocal microscope.*

A schematic diagram of a typical confocal laser scanning microscope is shown in Fig. 2.5. The first pinhole is placed immediately after the excitation laser source, and the other is placed before the Photo-Multiplier Tube (PMT) detector. The excitation light travels in from the laser source, an is narrowed by the first pinhole before passing through the dichroic mirror. The collimated light is then directed onto the specified part of the sample by the coupled effects of the scanning mirrors. The excited fluorophores in that sample region emits light which is picked up and descanned by the same mirrors until it reaches the dichroic mirror. Providing that the $\lambda_{emission}$ has little overlap with the $\lambda_{excitation}$, the emitted light is reflected by the dichroic mirror. Finally it reaches the Photo-Multiplier-Tube (PMT) after passing through the second pinhole. Here the photon counts will be processed for that particular sample space, which will

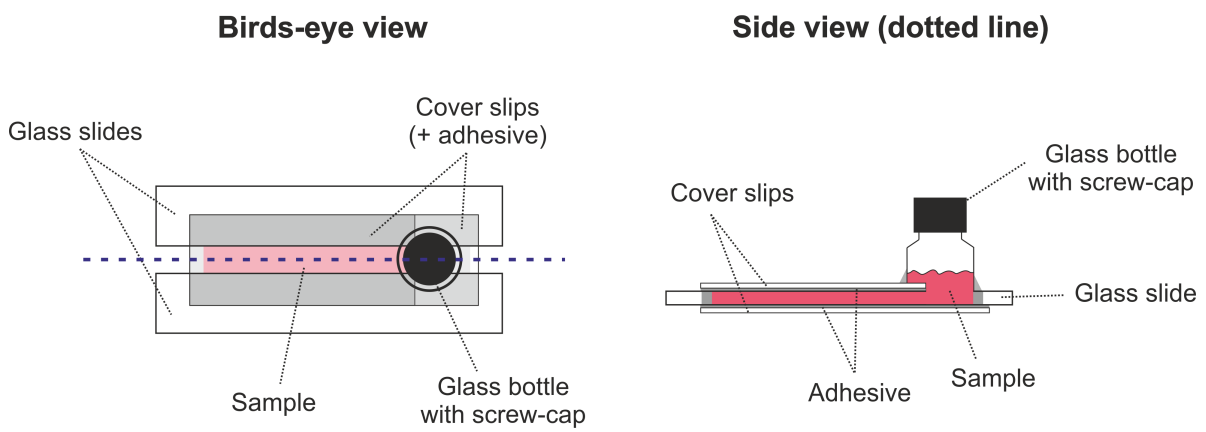


*Figure 2.6: Schematic of the glass sample cell designed for confocal microscopy and optical tweezing. All glass components are sealed by Norland 68 UV adhesive, as indicated by the grey shading. Colloidal samples are added/removed via the screw-cap on the half-bottle.*

be used for computer reconstruction of the entire image. If required, multiple PMT can also be attached to the setup for multi-channel detection.

Typically the resolution for a confocal microscopy is $\sim$ 200nm in $(x, y)$, and $\sim$ 500nm in $z$ due to the point spread function [61]. The speed of obtaining a 3D z-stack depends on the exact setup of the microscope. In this thesis most of the confocal images were taken using a custom Thorlabs confocal setup using a multi-channel fibre coupled laser source that offers excitation wavelengths at 488nm and 561nm. The confocal scans in the x-direction is controlled by a resonance mirror, operating at around 8kHz. The scan in the y-direction is controlled by a galvanometer mirror, which operates at a lower frequency. By using the 2-way scanning mode in $x$, the time required for a square 2D image can be halved. In order to obtain a 3D confocal image, the 60x oil imaging objective is mounted onto a piezo-stage, which allows for rapidly scanning through $z$ at specified intervals. Typically it takes $3s$ to image a z-stack of $20 \times 20 \times 20 \mu m^3$. This provides a set of 2D confocal images which can then be reconstructed for a full 3D volume image of the sample.

Multiple light scattering from the fluorescent samples can be greatly suppressed by refractive index matching the colloids with the dispersion medium. This will be discussed in detail in Chapter 3. Typically the refractive index matching samples contain non-polar and volatile solvents, therefore special sample cells (Fig. 2.6) were made to counter-act the corrosive effects of the solvents on the glue, as well as minimising any drift of the colloids during image acquisition. All glass parts of the cell have been sealed using Norland 68 UV adhesive and cured for 1 hour under UV light. They are then heated to 60°C overnight and left to cool before any sample solution is added.

### 2.4.3 Optical Tweezing

In 1970, Ashkin first demonstrated the manipulation of a micron-sized dielectric particle using a focused laser beam [99]. A year later, he and Dziedzic showed how the particle can be levitated by balancing the radiation pressure from the laser and gravitational forces of the colloid [100]. The development of the single-beam gradient optical trap has significantly improved trapping stability in 3D [101], and has since become the established method for optical tweezing in a number of different fields [54].

The single-beam gradient optical trap consists of a single strongly focused beam of laser light that provides large axial stability. The physics behind how a trapped particle interacts with the tweezing beam can be classified into three regimes, depending on the size ratio of the particle compared to the the laser wavelength: Rayleigh (for $\sigma << \lambda$), Mie (for $\sigma \approx \lambda$), and ray-optics (for $\sigma >> \lambda$). While the Mie explanation is more applicable in this thesis, as $\sigma/\lambda \sim 3$, we illustrate the principles of optical tweezing in terms of ray-optics, as the physics behind Mie theory is rather complex [102]. For both ray-optics regimes, the principle of optical tweezing can be explained insightfully in terms of gradient and scattering forces [101, 103]. A summary of this is given below.

When light travels from a low index material to a high index material, its speed is slowed down at the interfacial boundary and its path deviates towards the normal (Fig. 2.7). This refraction of light is also accompanied by a transfer of momentum to the high index material, which then experiences a restoring force. In the case of a colloidal particle, its stability inside an optical tweezer is balanced by all the forces acting on it, which includes the scattering force, the gradient force, and sometimes the gravitational force, which is negligible here. The scattering force comes from the radiation pressure of the incident laser, which acts along the axis of beam propagation and is proportional to the beam intensity. The gradient force arises from the refractions of light at the edges of the particle (Fig. 2.7), which transfer momentum to the particle. This acts to restore the particle towards the highest intensity gradient, i.e. the focal point, and is proportional to the gradient of beam intensity. Providing that the gradient forces are greater than the scattering force, the particle can be successfully trapped in 3D. The strength of the trap can be considered as a potential of the gradient force. Particles with a high effective index (i.e. $n_p/n_{solv} > 1$) are attracted to the center of the beam as described above. They act as a weakly positive lens, and the resultant gradient forces form a potential well. However for particles with a low effective index (i.e. $n_p/n_{solv} < 1$), the gradient potential reverses sign and repels the particle away from the centre of the trap (Chapter 6). For particles with a matching refractive index (i.e. $n_p/n_{solv} = 1$), both scattering and gradient forces equal to zero, as there is no refraction of light at the particle-solvent interface, and so

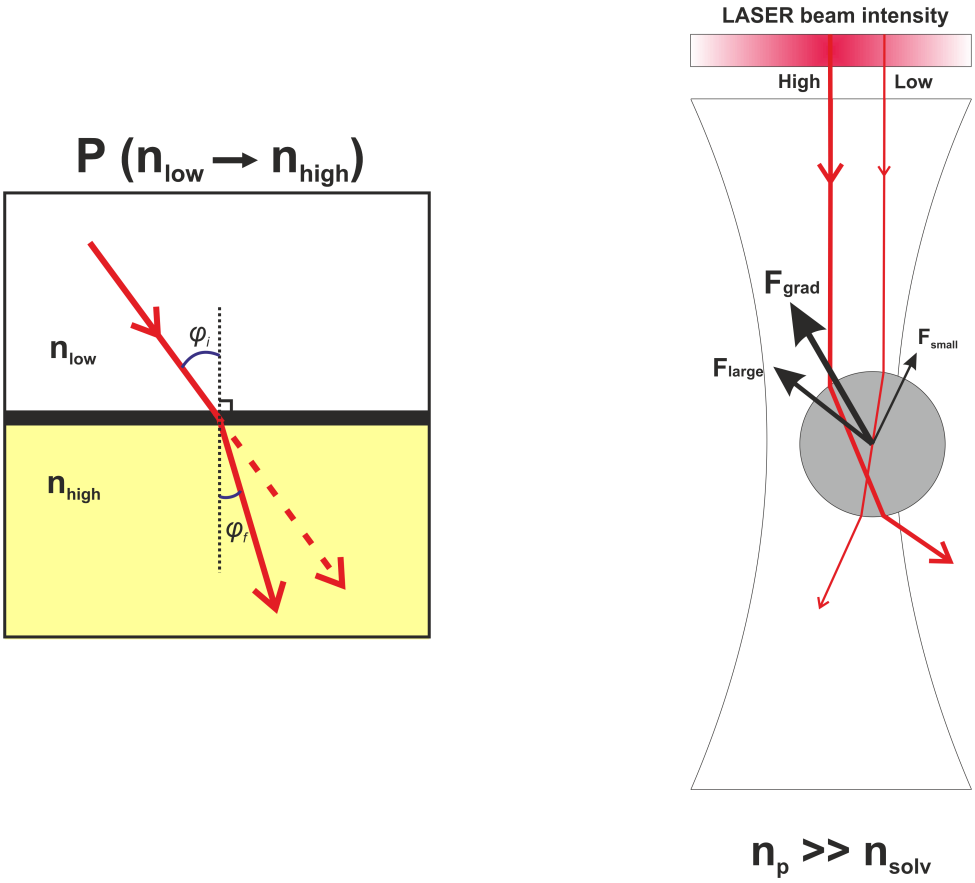


*Figure 2.7: Schematic diagrams illustrating: the refraction of light when travelling from a low refractive index material to a high refractive index material, and the gradient forces involved when trapping a particle with a higher $n_f$ than that of the solvent medium.*

the presence of the laser has no effect on the particle (Chapter 3).

A schematic of the special optical tweezing setup used in this thesis is shown in Fig. 2.8, and the details are provided by Curran et al. [71]. It is a decoupled confocal and optical tweezing setup that allows simultaneous 3D particle manipulation and imaging. The tweezing component uses a holographic optical trap, which allows complex trapping patterns to be created using a spatial-light-modulator (SLM) [54]. For instance, to create multiple traps inside the sample, the laser beam is first reflected off the computer-generated hologram displayed on the SLM, to create multiple diffracted beams. These are then carried forward and are Fourier-transformed by the sample objective into separate individual traps inside the sample. The 3D positions of the traps are fine tuned by adjusting the phase map displayed on the SLM. Note that SLM is superior for optical tweezing experiments in 3D to other beam-steering techniques such as the acousto-optic deflectors (AODs), as SLM allows control in the (x,y,z) positions of each individual trap. In comparison, AODs permits fast steering of multiple traps, but its control is limited to (x,y).

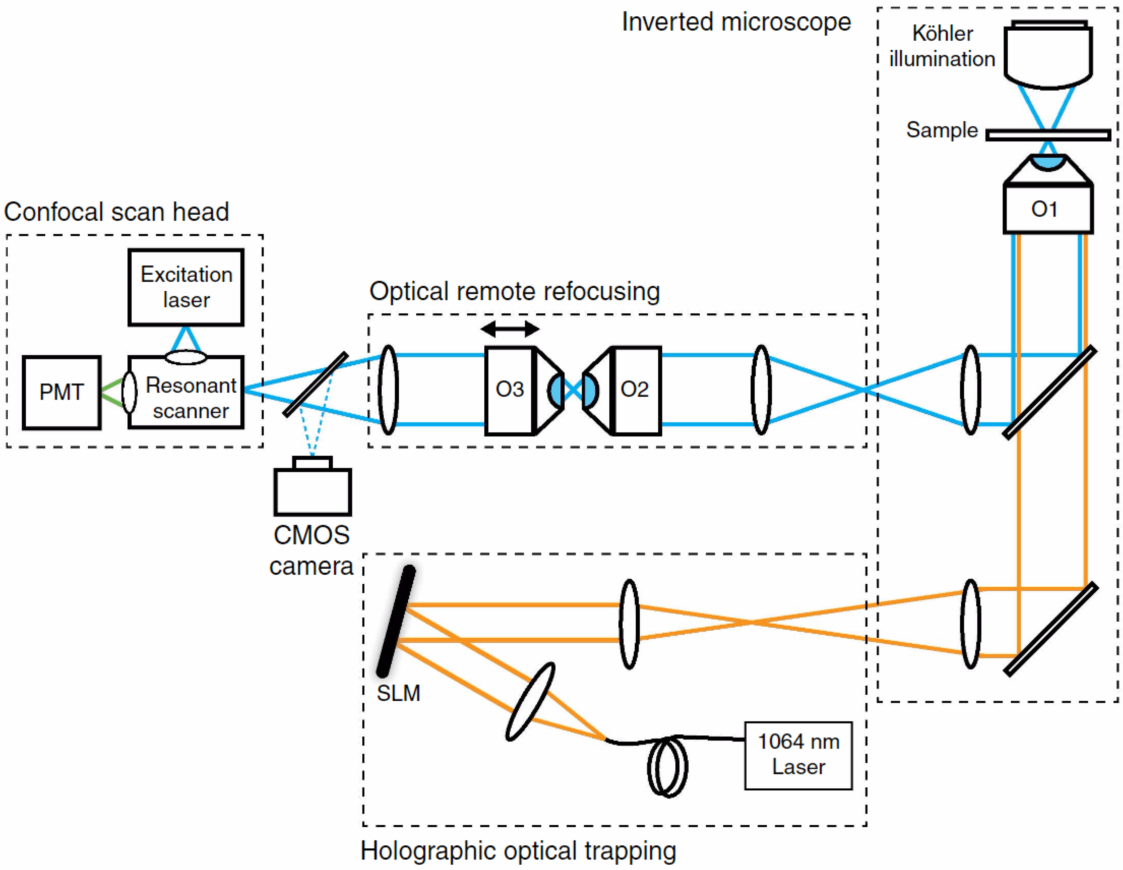


*Figure 2.8: Schematic of the decoupled and simultaneous 3D imaging and optical trapping setup as detailed in [71]. The flip mirror in front of the confocal scan head and the CMOS camera is used to switch between the confocal mode and brightfield mode, which is used in Digital Holographic Microscopy.*

### 2.4.4 Particle detection and Image analysis

#### Particle tracking in 3D

All of the particle positions and subsequent tracking for the 3D confocal data is done using the algorithms developed by Crocker and Grier [104], with the IDL routines written by Crocker and Weeks. Prior to the particle detection, a confocal time series is corrected for its intensity decay over time using the Histogram Matching method using ImageJ, where the histograms of all subsequent frames are matched to that of the initial frame. Within the particle tracking, first the imperfections and noise in the image are eliminated using a bandpass filter that smooths the image and subtracts the background (Fig. 2.9). Next, a Gaussian fit is run on the z-stacks to find the 3D coordinates of each bright spot, as well as their brightness and radius of gyration. The circular features are detected within a specified range in x, y, z, (Fig. 2.9) and uses the center-of-mass (COM) method to determine the particle center to sub-pixel accuracy [104]. The brightness and size of each found feature from the detection can be used eliminate false detections. Finally,

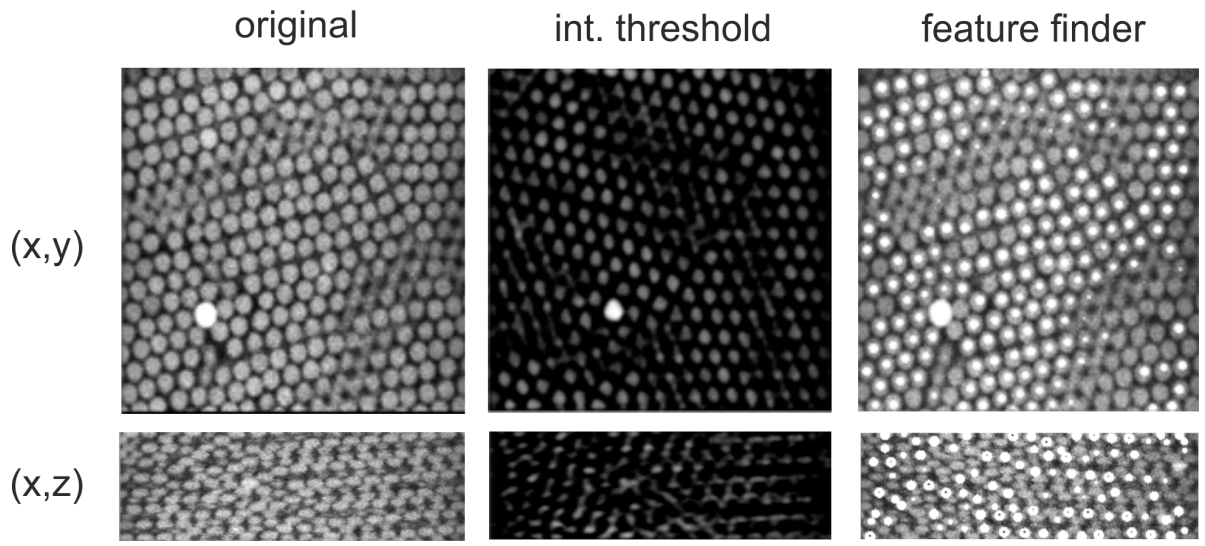


*Figure 2.9: Typical example of particle tracking of fluorescent TPM particles in 3D. The original images in (x,y) and (x,z) are shown on the left. The output of the bandpass filter is shown in the middle. Lastly, the output of 3D particle feature-finder is shown on the right, where white circles are plotted over the detected particle centres. Note the size of the circles plotted corresponds to the perpendicular distance of the particle centre away from the image plane (smaller circle = far away particle).*

the particle coordinates and stack IDs are passed along to the tracking algorithm, where the trajectories of individual particles are linked together and assigned an ID. The tracking trajectories are determined by considering the neighbouring positions in consecutive frames that are within the maximum pre-assigned distance. Providing that the pre-assigned distance is much smaller than the minimum inter-particle separation of $\sigma$, the tracking can be relied upon.

**Acknowledgments**

Arran Curran, Lia Verhoeff, Taiki Yanagishima, François Lavergne and Bo Peng are thanked for practical assistance and useful discussions.

# Chapter 3

# Colloidal TPM particles for three-dimensional confocal microscopy

ABSTRACT

In this chapter, we describe the synthesis and characterisation of 3-(trimethoxysilyl)propyl methacrylate (TPM) particles as a colloidal model system for 3D confocal scanning laser microscopy. The effect of the initial TPM concentration and pH of the reaction mixture on the growth and polydispersity of the particles are discussed, along with the method we used to achieve refractive index and density matching of the TPM particles. Finally a 3D confocal microscopy study is performed to characterise the sedimentation-diffusion equilibrium of the refractive index and density matched TPM sample, and the structure and the dynamics of the particles are examined.

## 3.1 Introduction

Colloidal particle suspensions have been used as accurate physical models to study complex phase behaviour since Jean Perrin's experiment in the early 1900s [105]. Given their easily accesssible lengthscale and timescale, they have provided fundamental insight into a wide of phase transitions [30, 106, 107]. With the development of powerful 3D imaging techniques, such as confocal microscopy [61], we have unprecedented access to the local processes involved in condensed matter phenomena such as crystallization, glass formation, and gels [108–110]. By matching the colloidal particle's refractive index and density using solvent mixtures, real-space and time-resolved studies of the complex structural and dynamic properties of the colloidal model material can be performed, at the single particle level [111].

Currently, the most widely used colloids model systems include silica spheres [111], polymethylmethacrylate (PMMA) spheres [30, 108], and poly(N-isopropyl acrylamide)(PNIPAM) spheres [89]. For studying the phase behaviour of near hard-spheres, PNIPAM is unsuitable due to its inherent 'softness' in $\theta-$solvents. As such, the most commonly used hard-spheres systems for confocal studies are fluorescent PMMA particles [61] and silica particles [111]. PMMA is a good model system, however it can be difficult to make because of the complicated synthesis of the PHSA stabiliser required [89, 112]. As for silica in 3D, density matching can be difficult to achieve due to its high mass density (see Table 3.1), so the effect of gravity is significant. Preliminary results have shown that microparticles made from 3-(trimethoxysilyl)propyl methacrylate (TPM) [113, 114] have similar mid-range refractive index and density to that of PMMA, unlike other conventional colloidal materials (Table 3.2).

*Table 3.1: Physical properties of common colloidal particles.*

| Particle type | $\rho$ /gcm$^{-3}$ | $n_f$ | Solvent stability |
|---|---|---|---|
| Silica [a] | 1.85 | 1.42 | all |
| PMMA [a] | 1.19 | 1.48 | $H_2O$, DMSO, aliphatic hydrocarbons |
| PS [a] | 1.05 | 1.59 | $H_2O$, low alcohols |
| MF [a] | 1.51 | 1.68 | all |
| TPM [b] | 1.30 | 1.517 | all |

[a] Data taken from MicroParticles GmbH website. http://microparticles.de/en/eigenschaften
[b] Determined experimentally in the lab. See section 3.4 for details.

Structurally, TPM consists of an inorganic alkoxysilyl head group and a long organic methacrylate tail (Figure 3.1). This allows it to bond covalently to both inorganic and organic materials, making it a very effective 'bridging' material, and is therefore widely used as a coating reagent in polymer and surface chemistry [115–118]. As a fully cross-linked colloidal particle, TPM has a high structural stability in both

polar and non-polar solvents due to its combined silicon chemistry and carbon chemistry (see Section 3.2.1). Therefore it is a suitable alternative to PMMA for creating a refractive index and density matched colloidal system, that can be used for 3D confocal microscopy studies.

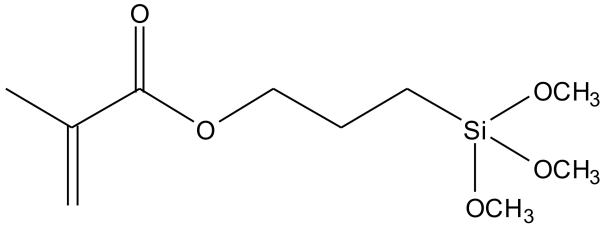


*Figure 3.1: 3-(trimethoxysilyl)propyl methacrylate (TPM).*

This chapter details the synthesis of TPM spherical particles for the purpose of creating a colloidal model system for 3D confocal microscopy. Factors, such as the TPM reagent concentration and reaction pH, that affect the growth and final outcome of the particles are investigated, and TPM particles are characterised using confocal microscopy, static light scattering (SLS) and scanning electron microscopy (SEM). Next we describe the procedure for finding the refractive index of the TPM particles and the solvent transfer process required to introduce these particles into low dielectric solvent media. Lastly, we observe the 3D sedimentation equilibrium profile of the TPM particles in the refractive index matching medium using confocal microscopy, and the structure and dynamics of the particles are examined.

## 3.2 Background

### 3.2.1 TPM Synthesis pathway

The method for TPM particle synthesis (Figure 3.2) is adapted and modified from the polymerisation techniques described by Obey et al. [119] and Sacanna et al. [120]. Although it is possible to hydrolyse TPM in deionised water to hydrolysed TPM monomers (hTPM) as shown on the LHS of Fig. 3.2, this is however a very slow process. Therefore $NH_3$ is used to catalyse this reaction, which rapidly condenses, via the same organosilanol monomers stage, into large branched oligomers (RHS of Fig. 3.2). These oligomers then precipitate out of the aqueous dispersion medium and nucleate into monodisperse oil droplets, which are stabilised against coalescence due to their negative surface charge. These droplets can be grown larger by further addition of the hTPM monomers (LHS of Fig. 3.2), and hence a precise control over the size of the final particle is possible. Once the desired size of oil droplet has been reached, $\alpha$-azo-iso-butyronitrile (AIBN) is added to start the thermally induced radical polymerisation of the

alkene groups in the R-branch of the TPM molecules (shown in the box of Fig. 3.2). Furthermore, the particles can be fluorescently labelled using rhodamine B isothiocyanate-3 aminopropyl trimethoxysilane (RITC-APS) dye [121] at the droplet stage, with the APS component covalently coupling to both the TPM and the RITC dye. Pluronic® F108 surfactant is also added to prevent polydispersity from arising during the dyeing and the radical polymerisation steps [122].

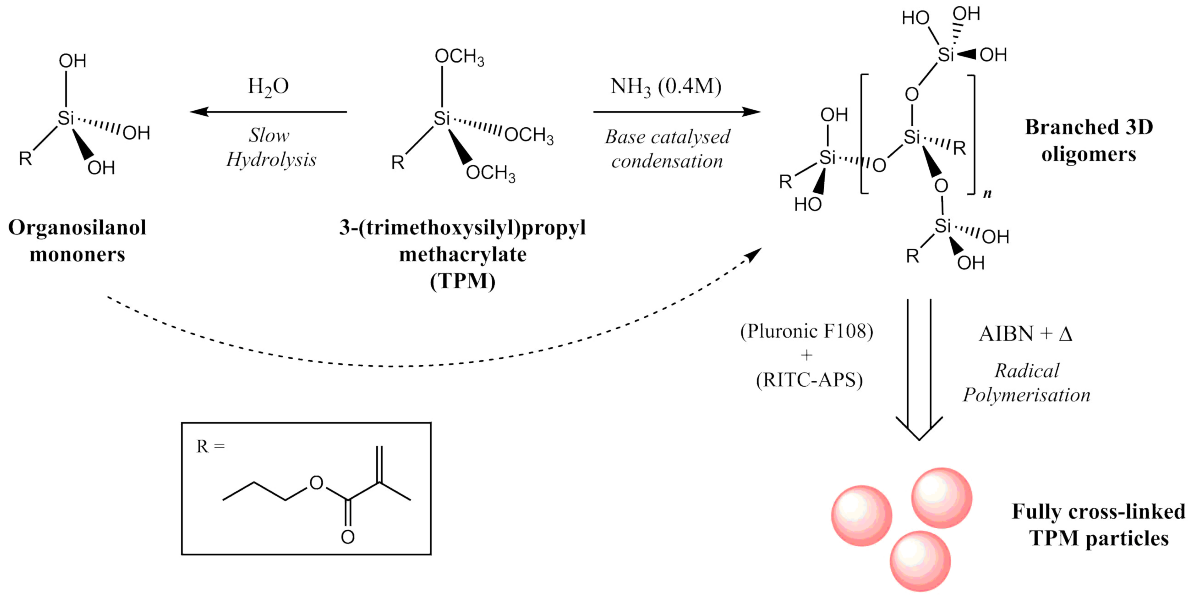


*Figure 3.2: Schematic reaction pathway for TPM particle synthesis.*

### 3.2.2 Three-dimensional confocal scanning microscopy

In order to obtain a dense 3D colloidal system where each particle can be clearly resolved using confocal microscopy regardless of imaging depth, it is essential to minimise multiple light scattering within the sample. This can be achieved by matching the refractive index of the dispersion medium to that of the TPM particles, as this will eliminate refraction of light at the particle-solvent interfaces. Note that the van der Waals forces between particles will also minimised by refractive index matching in non-polar solvents (Chapter 2).

The control of particle density matching with the solvent is also very important for the preparation of 3D colloidal systems. Since colloidal particles exhibit phase behaviours as a function of the particle number density (analogous to the effect of temperature in atomic and molecular systems), controlling the degree of density mismatch allows control of the height of the full sedimentation-diffusion equilibrium profile. As such, the volume fraction $\phi$ in the system is simply a function of the height, $z$, and the full phase behaviour of the system can be observed within the same sample. Analogous to the barometric

distribution in the Earth's atmosphere, the particle distribution in a non-interacting colloidal suspension, or an interacting system with $\phi \to 0$, can be described using the Boltzmann distribution as a function of height:

$$\phi(z) = \phi_0 \ \exp\Big(-\frac{z}{z_0}\Big). \tag{3.1}$$

Here $\phi_0$ is the initial packing fraction at $h = 0$, and $z_0$ is the gravitational length. Physically, $z_0$ follows from a balance of the thermal energy, $1k_BT$, and its gravitational potential energy:

$$z_0 = \frac{k_BT}{m^*g} = \frac{k_BT}{\Delta\rho v_p g}. \tag{3.2}$$

Here $T$ is temperature, $m^*$ the particle's buoyant mass, $\Delta\rho$ the density difference between the particle and medium, $v_p$ the particle volume, and $g$ the acceleration due to gravity. As $\frac{z}{z_0} \to 0$, $\phi \to \phi_0$ and the volume fraction would decay very slowly over a very long range in height. One way of achieving this is by density matching the particles to the solvent medium, thereby setting $\Delta\rho$ close to zero, and significantly increases the gravitational height.

### 3.2.3 Particle stabilisation in non-polar solvents

Electrostatic interactions between colloidal particles are usually determined by particle surface charge ($\eta$) as well as the Debye length of the solvent ($\kappa^{-1}$). The extent of the charge screening is dependent on the concentration of the charge species present as well as their valence (Chapter 2). When dispersed in deionised water, fully cross-linked TPM particles have a fairly large anionic surface potential that aid their stability against flocculation and aggregation. However when they are dispersed in non-polar solvents with a low relative permittivity ($\epsilon \approx 3$) to achieve refractive index matching, the screening length is much larger. According to DLVO theory (Chapter 2), if the van der Waals attraction is sufficiently large, it may overcome the double layer repulsion and lead to colloidal instability. Although the van der Waals force is minimised in a completely refractive index matched colloidal dispersion, irreversible particle aggregation may still occur during the solvent exchange. In order to prevent this, a commercial dispersant OLOA-1200 is added to the non-polar solvents before particles are dispersed in them. Detailed reports on the role of OLOA-1200 have been published by Dufresne et al. [84, 123], where it has been suggested that the active polyisobutylene-succinimide component in OLOA-1200 acts as a steric stabiliser as well as a charge control agent.

## 3.3 Experimental methods

### 3.3.1 Materials

3-(Trimethoxysilyl)propyl methacrylate (TPM, Polysciences Inc.), ammonium hydroxide solution (28% vol. $NH_3$ in $H_2O$, Sigma-Aldrich, $\geq$ 99.99%), $\alpha$-azo-iso-butyronitrile (AIBN, BDH, UK) were used as supplied. The fluorescent monomer RITC-APS (rhodamine B isothiocyanate aminopropyl trimethoxysilane) was synthesized according to the procedure described by Ivell et al. [121] in dimethyl sulfoxide (DMSO, Sigma-Aldrich, $\geq$ 99.5%), using rhodamine B isothiocyanate (Aldrich) and 3-aminopropyl trimethoxysilane (APS, Aldrich, 97%). PEG-PPG-PEG Pluoronic® F108 (Aldrich) was converted to a 5% w/w aqueous mixture before being used in the experiments. The following solvents were supplied by Sigma-Aldrich and were filtered by Millipore Hydrophobic PTFE 0.45$\mu$m before usage : ethanol ($\geq$ 99.8%), toluene (anhydrous, 99.9%), 1,2,3,4-tetrahydronaphthalene or tetralin (99%), trichloroethylene (TCE, $\geq$ 99.5%), tetrachloroethylene (PERC, $\geq$ 99%). OLOA-1200 was produced by Chevron Chemical Co. and was supplied to us by Eric Dufresne. Ultrapure water (Type I) was used in the syntheses, and was obtained directly from Millipore Direct-Q® 3 purification system.

### 3.3.2 Particle Synthesis

Typically, a batch of monodisperse TPM particles is prepared in a round bottom flask. First, deionised water is mixed thoroughly with 0.1% v/v $NH_4OH$(aq) using a magnetic stirrer to get a homogeneous solution of ~pH10. Next, TPM oil is injected rapidly below the solution surface and is allowed to react for 45mins at 500rpm. Nucleation of the droplets can be seen around 5 minutes after the start of the reaction, as the mixture becomes increasingly turbid. The course of the reaction is followed by taking 20$\mu$l samples from the reaction mixture and checked using brightfield microscopy. If particles > 2$\mu$m are required, it is possible to tune the size by dropwise addition of hydrolysed TPM monomers (hTPM) at a rate of $\sim 10 \times 100\mu$l drops per minute. The hTPM monomer solution is prepared by stirring a 1:10 volume ratio mixture of TPM and ultrapure water overnight at 300rpm. The progress of this seeded growth is checked periodically by bightfield microscopy until the desired size is reached.

To prevent droplet coalescence in the subsequent fluorescence labelling step, Pluronic® F108 surfactant can be added to stabilise the droplet surface. A quantity of 25$\mu$l of F108 solution (5% w/w) is introduced per 1ml of the reaction mixture, equivalent to 0.125% w/w F108 overall. Next the

TPM droplets are labelled with the RITC-APS fluorescence monomers dissolved in DMSO. The dye is introduced in 100$\mu$l increments at 5 minute intervals until the colour of the mixture is fully saturated. Finally the droplets are polymerised into fully cross-linked particles by free radical polymerisation using AIBN. This is added in excess ($\geq$ 3mMol) and is stirred for 10 minutes before the reaction mixture is heated to 80°$C$ for 5+ hours in the oven.

The particles are cleaned in ultrapure water by repeated centrifugation, decanting and redispersion by gentle sonication and stirring. Any residue or secondary TPM nucleations are removed by decanting the supernatant at least three times. The size and polydispersity of the particles are determined using a combination of light scattering techniques and scanning electron microscopy (SEM). Details of sample preparation are given in Chapter 2, Section 2.4.1.

### 3.3.3 TPM characterisation using SLS

The radius and the polydispersity of a given batch of TPM particles is found using static light scattering (SLS). The raw SLS data is analysed as follows: the logarithm of the intensity is first plotted against the square of the scattering vector $k^2$, which is related to the angle of detection ($\theta$) by $k = 4\pi sin(\theta)/\lambda$. The scattering decay curves are then compared with calculated values from Mie theory as explained in Chapter 2 section 2.4.1, until a visually optimum match has been found.

### 3.3.4 Refractive index determination

The refractive index of fully cross-linked TPM particles may vary considerably depending on the exact nature of their synthesis [124]. In order to establish the approximate refractive index of our TPM particles, we disperse a representative sample (batch *yl-01-09*, Table 3.2) in binary mixtures of different refractive indices and examine at the transmittance (or absorbance) of light through it [125]. The point of maximum transmission of the incident light (or minimum absorption) is expected to occur at the point of optimum refractive index matching of the TPM particles and the solvent medium. Since absorbance is dependent on the concentration of the particles present in the solution, care is taken to ensure that the volume fraction is identical for all test mixtures at $\phi = 0.08$.

Four different types of solvents are used for the refractive index matching procedure: toluene ($n_f$ = 1.494, $\rho = 0.867 gcm^{-3}$), tetralin ($n_f$ = 1.541, $\rho = 0.970 gcm^{-3}$), trichloroethylene (TCE, $n_f$ = 1.478, $\rho = 1.464 gcm^{-3}$) and tetrachloroethylene (PERC, $n_f$ = 1.506, $\rho = 1.620 gcm^{-3}$). The refractive indices

of the different ratios of solvent mixtures are determined by Anton-Paar Abbemat 200 refractometer prior to the experiment, and their densities are determined using Anton-Paar DMA 4500M Density Meter. These four solvents were chosen because their dielectric constants are all $\sim 3$, and they have very different refractive indices and densities at room temperature. The absorption spectra of the various colloidal suspensions are measured using a UV-1800 Shimadzu UV spectrophotometer at room temperature for 800 nm < $\lambda$ < 1000 nm, where the absorbance showed little dependence on $\lambda$. This range of wavelength is also appropriately close to wavelength of the laser light used for optical trapping ($\lambda_{opt}$ = 1064 nm), whose application will be discussed in Chapter 4.

### 3.3.5 Solvent transfer

The particles are transferred from the aqueous medium to the low dielectric non-aqueous medium by step-wise solvent transfer, with an intermediary ethanol (EtOH) stage. Direct transfer from water to organic medium would result in irreversible particle aggregation. Therefore the particles are transferred from pure $H_2O$ to 50 : 50 (v/v) $H_2O$ : EtOH, then to pure EtOH, then 50 : 50 (v/v) EtOH : apolar, and finally into the 100% apolar medium. Ethanol has been chosen as the intermediary solvent because it is miscible with both water and low dielectric solvents. The transfer procedure involves sedimentation of the particles by high speed centrifugation and removing the solvent, before adding in the new solvent mixture and redispersion by sonication and stirring. Care is taken to remove all traces of water from the particles, otherwise aggregation may occur. To facilitate this, the solvent transfer to pure ethanol is repeated 3 times, and particles are left in ethanol for at least 24 hours before progressing onto the next solvent transfer stage. Gentle heating the sample to $40-50°C$ will help with the solvation process, though excessive heating is avoided as this will damage fluorophores.

For the 3D experiments detailed in this thesis, all particles were eventually transferred to a tetralin : TCE binary mixture (45:55 (v/v)) containing 1 wt % of OLOA 1200, which is used to control the screening length (see Section 3.2.3). Preliminary results have shown that TPM particles exhibit a significant electrostatic repulsion in low dielectic mediums ($\epsilon_r \sim 3$) without OLOA 1200, but instead flocculates if OLOA 1200 concentrations exceeds 1.5 wt %. Therefore in the final colloidal dispersion, 1 wt % of OLOA 1200 surfactant is used for the 3D host system, where the particles are stable and are sufficiently screened. The final solvent mixture consisting of 45:55 tetralin and TCE (v/v) with 1 wt % OLOA 1200 has $n = 1.506$ and $\rho = 1.20 g cm^{-3}$ [1], which enables close density matching as well as near refractive index matching to the TPM colloids.

[1]Density was determined experimentally by measuring the mass for a given volume of solvent mixture.

*Table 3.2: List of TPM particle preparations and outcomes.*

| Batch | $H_2O$(ml) | $NH_3$($\mu$l) | TPM(ml) | hTPM(ml) | F108(ml) | RITC-APS($\mu$l) | $r_{SLS}$(nm) | $\sigma_{SLS}$(%) | $r_{SEM}$(nm) | $\sigma_{SEM}$(%) |
|---|---|---|---|---|---|---|---|---|---|---|
| yl-00-01 | 50 | 50 | 0.20 | - | 0.02 [a] | - | - | - | - | - |
| yl-01-09 | 30 | 30 | 0.50 | 10 | 0.02 | 200 | 1220 | 4.0 | 1278 | 3.5 |
| yl-01-12A | 30 | 30 | 0.50 | 10 | 0.02 | - | - | - | 1147 | 2.2 |
| yl-01-12B | 30 | 30 | 0.50 | 10 | - | 200 | - | - | 1044 | 2.9 |
| yl-01-18A | 180 | 180 | 4.00 | - | 4.50 | (300) [b] | 1300 (1320) | 2.5 (3.0) | 1253 (1260) | 1.1 (3.4) |
| yl-01-18B | 180 | 180 | 1.00 | - | 4.50 | (300) [b] | 645 (650) | 4.0 (5.0) | 623 (623) | 2.2 (3.2) |
| yl-01-18C | 180 | 180 | 2.00 | - | 4.50 | (300) [b] | 840 (850) | 3.0 (4.0) | 827 (828) | 2.0 (2.7) |
| yl-01-18D | 180 | 180 | 0.50 | - | 4.50 | (200) [b] | 340 (320) | 9.0 (8.0) | 302 (305) | 2.7 (5.6) |
| yl-01-18E | 180 | 180 | 0.25 | - | 4.50 | (100) [b] | 215 (220) | 10.0 (11.0) | 202 (208) | 5.2 (8.4) |
| yl-01-18F | 180 | 180 | 0.75 | - | 4.50 | (300) [b] | 545 (540) | 4.5 (6.5) | 513 (510) | 2.6 (5.4) |
| yl-01-18G | 180 | 180 | 1.50 | - | 4.50 | (400) [b] | 720 (720) | 3.5 (4.5) | 671 (664) | 3.7 (6.2) |
| yl-01-25A | 40 | 40 | 0.20 | 3 | 2.15 | 250 | 820 | 4.2 | 803 | 2.5 |

[a] TPM droplet growth experiment. F108 is used to quench the droplet growth for 1ml samples taken out at regular time intervals.

[b] Reaction was split into two equal parts prior to RITC-APS addition, only one part is labelled with the fluorescence dye (results given in parentheses).

### 3.3.6 Confocal microscopy and image analysis

The confocal microscopy experiments are carried out using the confocal laser scanning microscope setup described in Chapter 2, Section 2.4.3. TPM particles (batch *yl-01-09*, see Table 3.2) are cleaned and transferred to a 45 : 55 tetralin : TCE mixture that contains 1 wt % of OLOA 1200. Typically $\sim 100\mu$l is injected into a glass sample chamber described in Chapter 2 Section 2.4.2 and left to sediment for 2-3 days.

To observe the sedimentation equilibrium of TPM particles, confocal z-stacks of $32 \times 28 \times 100\mu m^3$ are taken with $z$-resolution of 200nm using bi-directional scanning. For the particle dynamics experiment, 3D time-series of $32 \times 28 \times 20\mu m^3$ blocks were scanned for 400 frames, for a total of 27 mins each on average. The z-spacing was increased to $250nm$ so as to reduce the time taken to image each z-stack in the time series. Lastly the 3D particle coordinates are extracted and tracked from the 3D confocal data using the particle tracking method described in Chapter 2.

## 3.4 Results and discussion

### 3.4.1 TPM Synthesis and characterisation

First, we monitor the growth profile of the TPM particles. As shown in Fig. 3.2, the first part of the synthesis relies on the base-catalysed hydrolysis and condensation of TPM monomers. Once the saturation point of the TPM oligomers has been reached, they rapidly phase-separate and nucleate into multiple droplets. Visually this is observed by the change of the reaction mixture from being clear and colourless to being cloudy and turbid, as droplets of $\sim 400nm$ in diameter begin to scatter visible light. As the number and the size of the TPM droplets increase, the opacity of the reaction mixture increases as well (see Fig. 3.3), as greater extent of light scattering occurs. We can also observe the progress of the synthesis using brightfield microscopy. A comparison of the size of droplets and the turbidity of the reaction solution is also shown in Fig. 3.3.

From the reaction mechanism (Fig. 3.2), the rate of TPM hydrolysis and nucleation is expected to depend on the pH of the starting mixture. Therefore we compared the growth profiles of TPM droplets at four different values of starting pH. In a starting mixture of 50ml $H_2O$ and 0.3ml TPM reagent, 20, 130, 450, 1770 $\mu l$ of $NH_4OH$ (28%) have been added to give starting pH of 9.46, 10.00, 10.41 and 10.90 respectively, measured using a digital pH meter. The reactions were left to run as usual, and 0.5ml

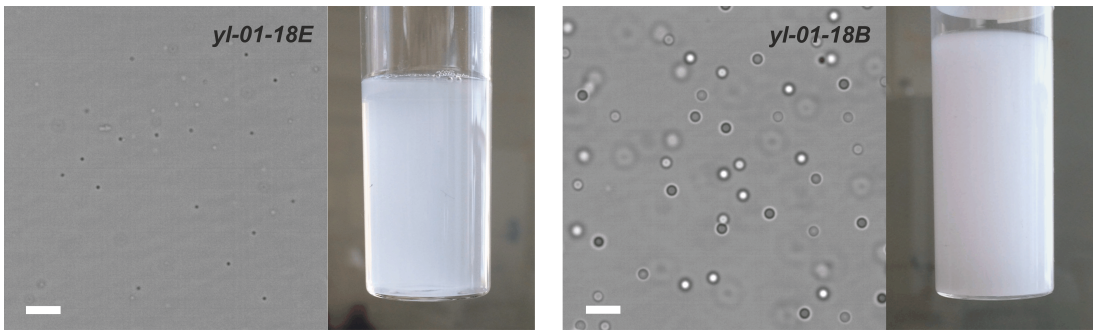


*Figure 3.3: Brightfield and macroscopic images of TPM droplets of two different sizes (final particle data given in Table 3.2). Scale bar = 5μm.*

samples were extracted at specified time intervals and quenched using an excess quantity of F108 (5% wt) solution. The sizes of the droplets are determined using DLS at a fixed detection angle and are plotted in Fig. 3.4A. Between pH 9.46 and 10.41, increasing the pH of the reaction mixture dramatically increases the rate of droplet growth at the start, and decreases the time required for reaching the final size. This can be attributed to the increasing concentration of $OH^-$ species at higher pH, which catalyses the hydrolysis of TPM monomers and rapidly increases the oligomer concentration in solution at the start. In relation to the colloid growth profile explained in Chapter 2, this results in a sharper peak in the LaMer diagram and a narrower window for nucleation events. As such, subsequent hydrolysis of TPM monomers only serves to grow the existing nucleated droplets. This pattern is also reflected in the final droplet sizes for pH 9.46 - 10.41, where the size increased with pH, signifying fewer droplets formed in the reactions as pH increased. On the other hand, the growth profile for pH 10.90 seems to have reversed this trend. Although the time taken for both pH 10.90 and pH 10.41 to reach the final size are nearly identical, nevertheless the final droplet size is much smaller at pH 10.90 than the one at pH 10.41. One possible explanation for this is that the rate of TPM hydrolysis at pH 10.90 is even higher than before, and the bulk quantity of monomers is depleted at the start to form a greater number of nuclei. With insufficient TPM remaining in solution, the final droplet size is therefore restricted. However this hypothesis requires further investigation.

For the rest of this thesis, the pH for TPM synthesis is fixed at pH 9.90. A growth profile of TPM droplet at this pH is recorded in Fig. 3.4B for batch yl-00-01, with the error bars corresponding to the standard deviation in particle radii from the DLS measurements. The logistic growth curve fitting shown in Fig. 3.4B was used as a visual guide to the growth profile, and it approximated the final TPM droplet radius to be 373nm. Comparing this with the average radius of the fully cross-linked particles ($r$ = 346.7nm, $\sigma$ = 6.6%), we can find an approximate mass density of the polymerised TPM colloids. Since the TPM droplets are stabilised by a high anionic surface charge at pH > 9 and the F108

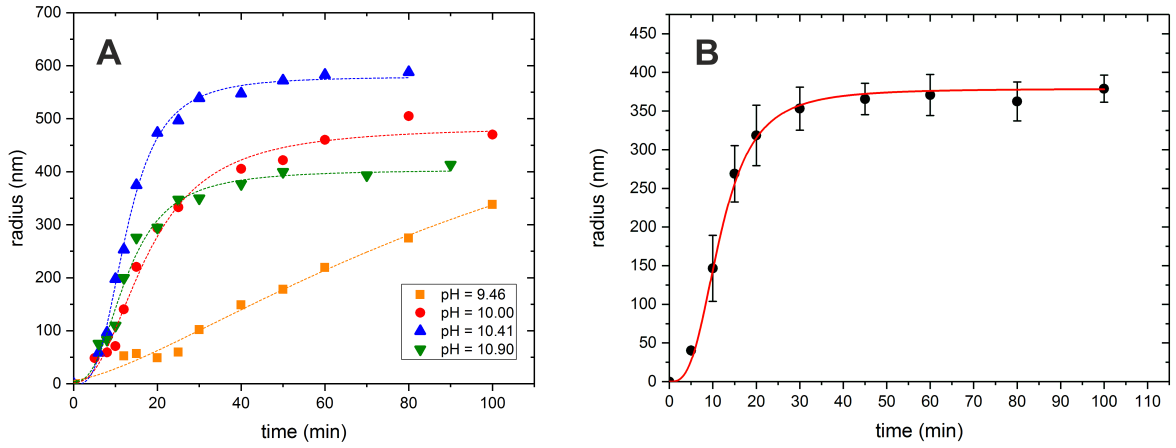


*Figure 3.4: (A) Growth profiles of unpolymerised TPM droplets at four different starting pH (B) Growth profile of yl-00-01 at initial pH = 9.90, where the droplet size stabilises after 60min to a final radius of 373nm. Note that the lines shown in both plots are for visual guidance of the droplet growth.*

surfactant [114], we can assume that the mass of an individual TPM droplet remain unchanged during the polymerisation process. Knowing the density of uncross-linked TPM monomers ($\rho_L = 1.045 g cm^{-3}$, we can use the ratio of the final cross-linked particle volume $V_S$ and the final pre-polymerised droplet volume $V_S$ to estimate a density of the TPM particles. Since $V \propto r^3$:

$$\frac{\rho_S}{\rho_L} = \frac{V_L}{V_S} = \left(\frac{r_l}{r_s}\right)^3. \tag{3.3}$$

From this, we estimate the density of final cross-linked TPM particles to be $1.30 g cm^{-3}$.

In a given reaction, the final size of the TPM droplets (particles) also depends on the availability of TPM monomers in solution. This can be adjusted either at the start of the synthesis by tuning the concentration of the TPM reagent, or by the slow addition of hydrolysed TPM solution post nucleation. The effect that the initial TPM concentration has on the radii of the final cross-linked particles is shown in Fig. 3.5, where the error bars correspond to the standard deviation in particle size detected by SLS and Mie fitting. It is clear that the radius of the TPM particles can be tuned from $\sim 200nm$ to over $1\mu$m by varying the initial concentration of TPM.

SEM images of highly monodisperse TPM particles are shown in Fig. 3.6(i-iii) for three different particle sizes. The corresponding SLS data is also shown in Fig. 3.6(iv), together with the Mie-fits. Particle data from the synthesis is summarised in Table 3.2. Note that the differences in the SLS and SEM measurements are attributed to the drying process and the high vacuum condition required for SEM.

Finally, it appears that the addition of the RITC-APS dye to the reaction can cause a slight increase

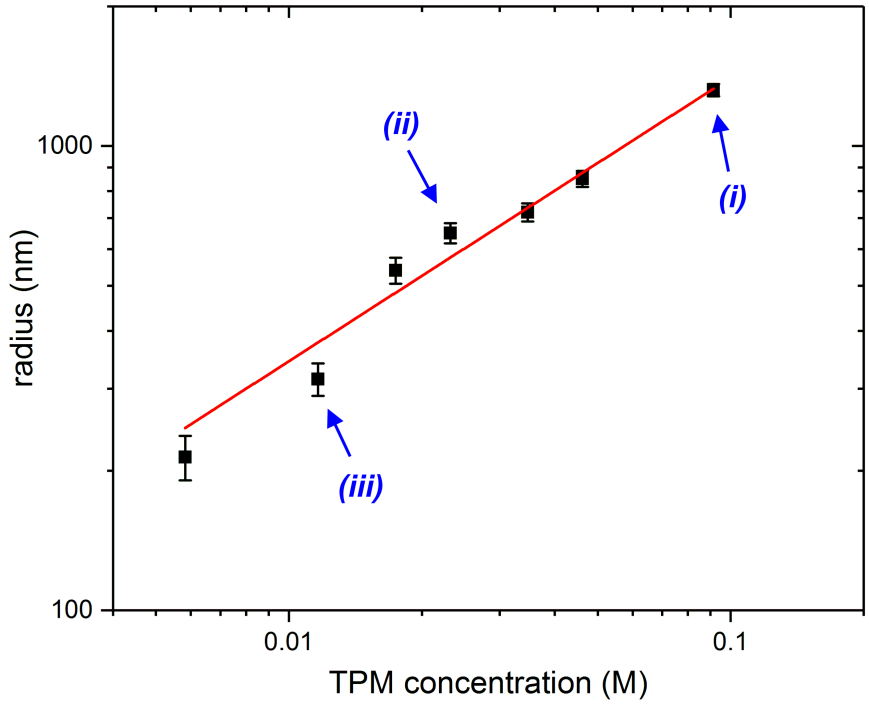


*Figure 3.5: Final size of fully cross-linked fluorescent particles as a function of the initial TPM concentration (yl-01-18 series) determined using SLS. The particle sizes and polydispersities are given in Table 3.2. SEM and SLS data of these particles are provided in Fig. 3.6.*

to the droplet polydispersity, as seen in the data for the undyed and dyed particles in the yl-01-18 series (Table 3.2). However, fluorescence labelling is essential for confocal imaging in 3D. Fortunately, the florescent batches with particle radius larger than $1.4\mu m$ have polydispersities $\sigma$ below 5%, so they are sufficiently monodisperse for exhibiting crystallisation at high volume fractions.

### 3.4.2 Refractive index of TPM particles

As discussed in Chapter 2, refractive index matching of the particles with the surrounding medium is necessary for 3D confocal imaging of a dense colloidal system. TPM particles (batch *yl-01-09*) is dispersed in solvent mixtures with different refractive indices (examples are shown in 3.7. The solvent ratios are given in Table 3.3, along with the measured refractive indices of the solvent mixture without particles, as well as the absorbance level of each sample at $\lambda$ = 900 nm. As the refractive index of the dispersion medium approaches the refractive index of the particles, the turbidity of the solution reduces significantly because of reduced light scattering. Near the point of optimum refractive index matching, the colloidal suspension becomes completely transparent. Examples are shown in Fig. 3.7 where TPM particles are dispersed in solvents of different $n_f$ at the same particle concentration.

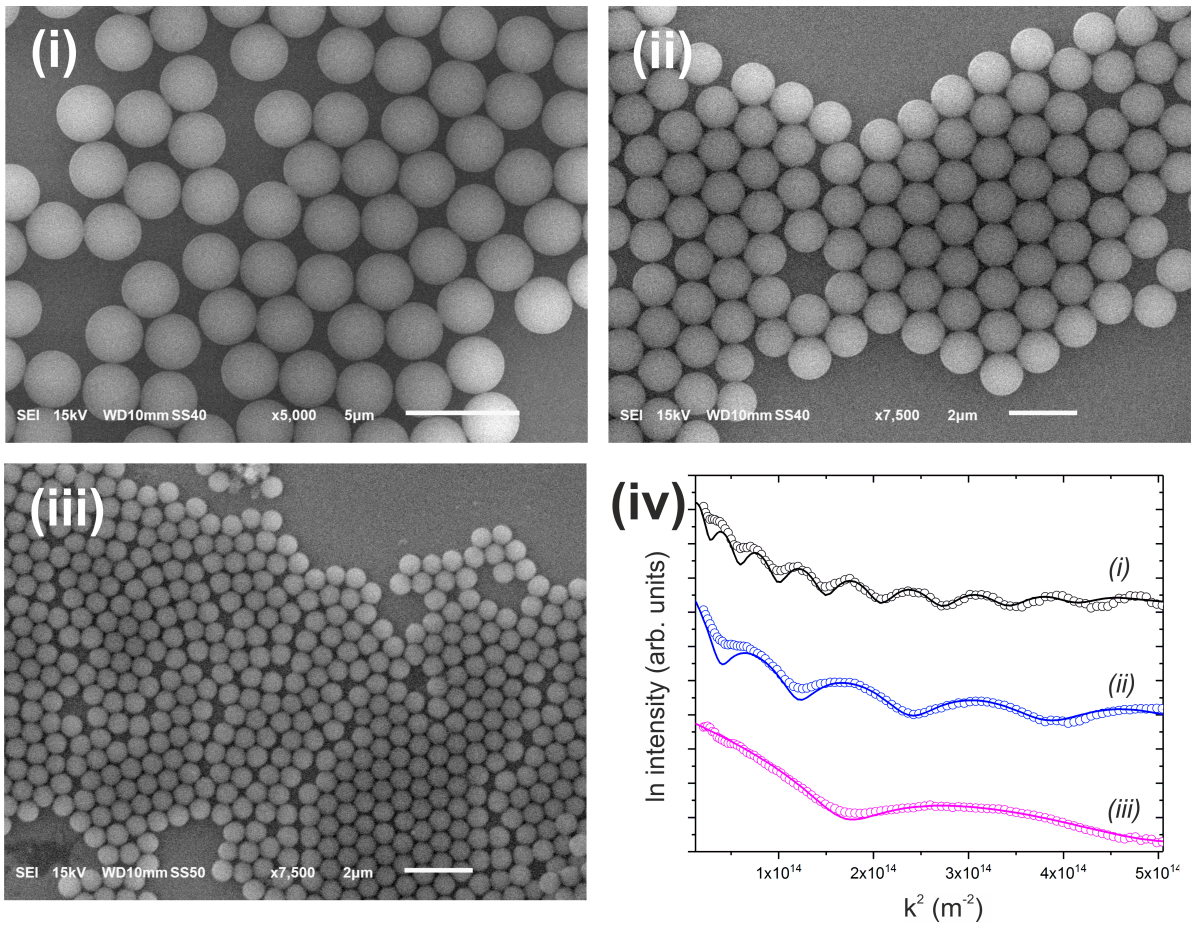


*Figure 3.6: SEM images of cross-linked TPM particles as indicated in Fig. 3.5, corresponding to batches: (i) yl-01-18A, (ii) yl-01-18B, and (iii) yl-01-18D, with different starting TPM concentrations. Their corresponding SLS patterns are shown in(iv), which determined the SLS radii and polydispersities in Table 3.2.*

The plot of the absorption level at $\lambda = 900nm$ as a function of the refractive index of the solvent is given in Fig. 3.8. These points are fitted to a parabolic function to find the minimum absorption, or optimum index matching, for TPM to be at $n = 1.517 \pm 0.01$.

### 3.4.3 Confocal microscopy study of sedimentation equilibrium of TPM

As a result of the good refractive index matching of the solvent medium with the TPM particles, we are able to fully image a TPM system in a sedimentation-diffusion equilibrium at the single-particle level. An example of the 3D colloidal system is shown in Fig. 3.9A, which is reconstructed in 3D using real confocal $x/y$ image slices. As such, we are able to view the sample block from any perspective in $x$, $y$ and $z$. The view shown in Fig. 3.9A displays the $x/z$ side-on view of the z-stack, showing the full phase behaviour of the system over $100\mu m$ in the $z$-direction. Particle coordinates extracted from Fig. 3.9A can also be used to create a 3D digital rendering of the system, as shown in Fig. 3.9B. The corresponding phase behaviour

*Table 3.3: Solvent mixtures of varying refractive index and density that are used for deducing the refractive index of TPM particles, along with the measured absorbance of the colloidal samples containing TPM particles at $\phi = 8\%$).*

| solvent | $n_f$ | $\rho(gcm^{-3})$ | Absorbance |
|---|---|---|---|
| tetralin | 1.541 | 0.970 | 0.390 |
| tetralin : toluene (80:20) | 1.532 | 0.950 | 0.160 |
| tetralin : toluene (60:40) | 1.523 | 0.929 | 0.035 |
| tetralin : toluene (50:50) | 1.519 | 0.919 | 0.004 |
| tetralin : toluene (40:60) | 1.514 | 0.908 | 0.013 |
| TCE : tetralin (40:60) | 1.516 | 1.167 | 0.007 |
| TCE : tetralin (50:50) | 1.509 | 1.217 | 0.036 |
| TCE : toluene (50:50) | 1.487 | 1.217 | 0.658 |
| TCE : PERC (50:50) | 1.491 | 1.542 | 0.432 |
| toluene : PERC (50:50) | 1.501 | 1.295 | 0.167 |

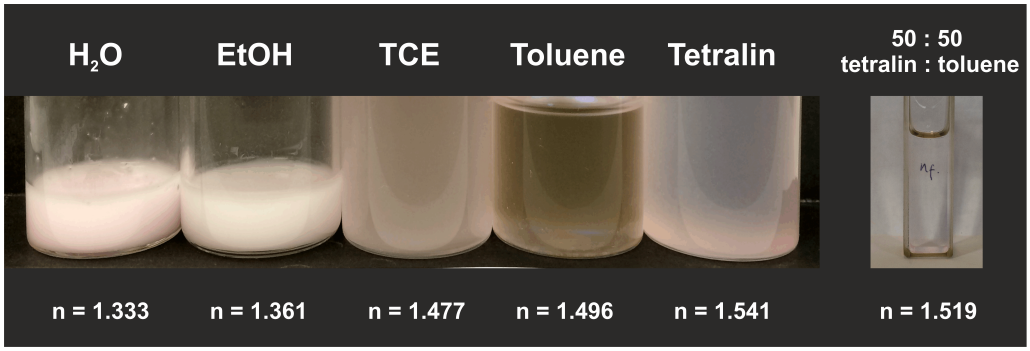


*Figure 3.7: Examples of dispersions of fluorescent TPM particles ($\phi \sim 8\%$) in solvent medium with different refractive indices, displaying a varying extent of turbidity.Transparency is demonstrated at $n_f = 1.519$ in the last image.*

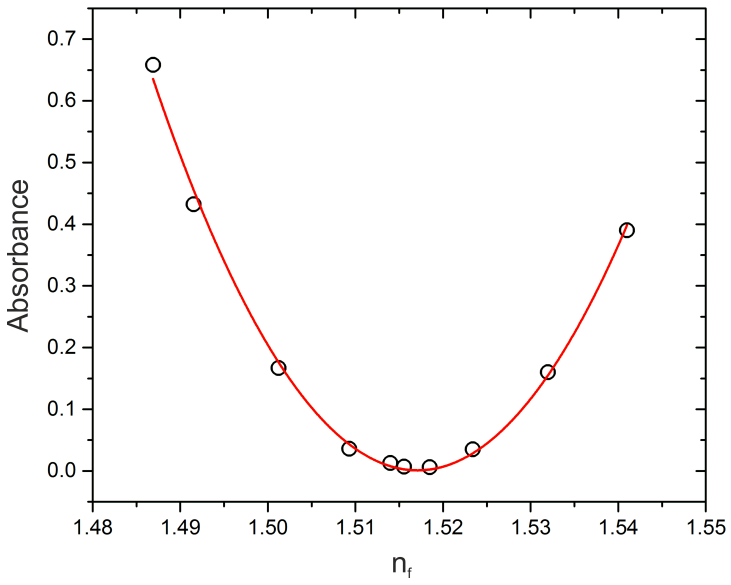


*Figure 3.8: Plot of the level of absorption of incident laser light ($\lambda = 900nm$) by the samples in Table 3.3, along with a parabolic fit with the minimum at $n_f = 1.517 \pm 0.01$.*

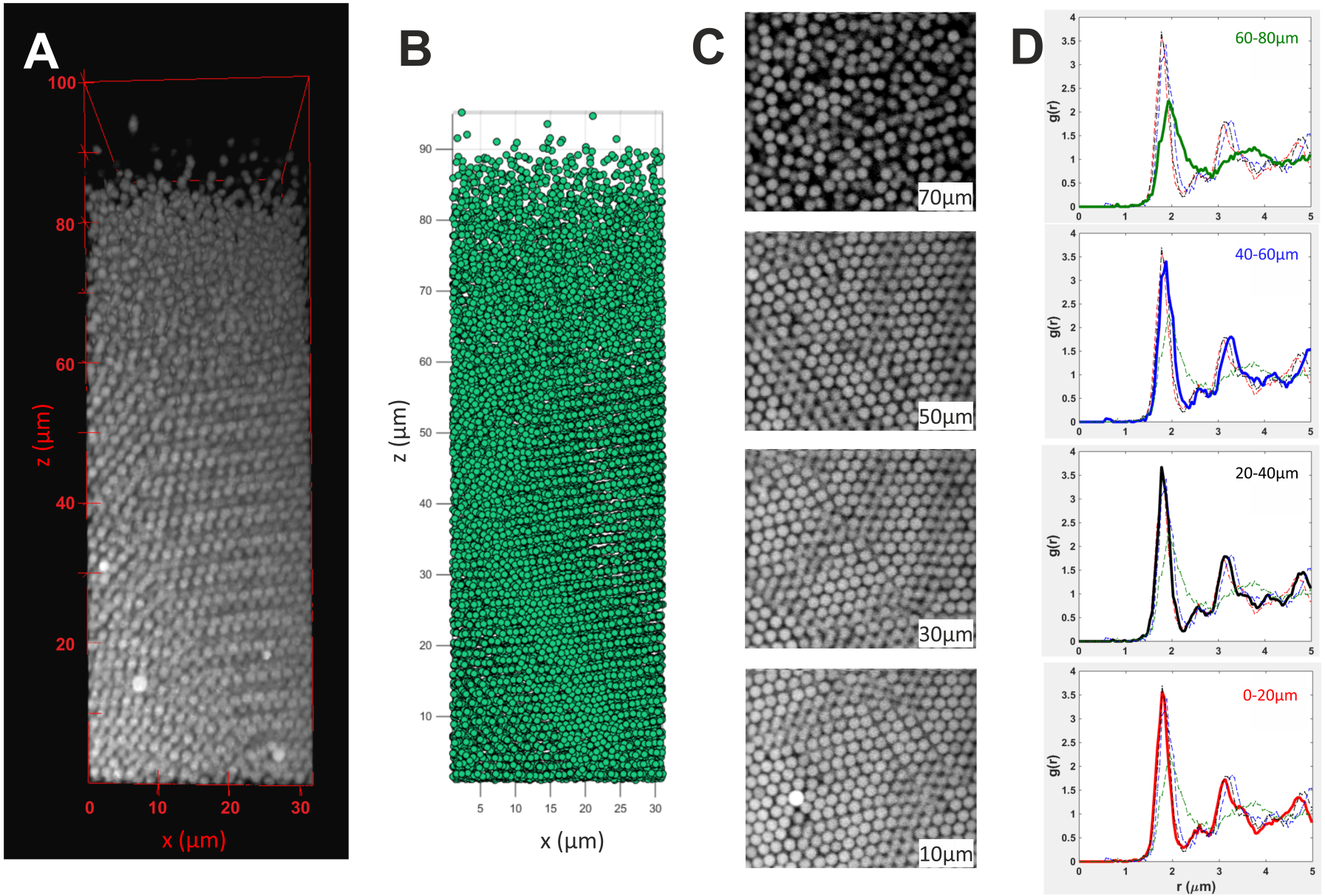


*Figure 3.9: (A) $x/z$ plane of a 3D confocal image reconstruction of a TPM $z$-stack. (B) MatLab rendered $z$-stack using particle coordinates detected from (A) using the Crocker and Weeks algorithm [104] (Chapter 2). (C) $x/y$ confocal slice images at specified $z$-height in the stack shown in (A). (D) Radial distribution functions $g(r)$ for the sub-stack between specified heights in $z$.*

and packing arrangement match perfectly in both diagrams, thus confirming the suitability of our colloidal TPM particles in the refractive index matching solvent for quantitative 3D confocal imaging.

To further demonstrate the change in the particle packing and the phase behaviour as a function of height, we have also shown confocal snapshots of the $x/y$ plane at four different heights in this $z$-stack (see Fig. 3.9C). This is accompanied by their respective radial distribution functions $g(r)$ in Fig. 3.9D. It is clear from both the confocal slices and the $g(r)$ that the sample between $0 < z < 60\mu m$ is closely packed and crystalline. This is reflected in the sharp second and third peaks in the $g(r)$, indicating a high degree of packing order. However for $z > 60\mu m$, there is a clear decrease in the particle packing and the form of the $g(r)$ is more liquid-like, with much less pronounced higher-order peaks compared to the previous plots.

As discussed in section 3.2.2, the change in the particle number density along $z$ is reflected in the phase behaviour at different heights in the sample. With the decrease in the number density $n(z)$ as $z$ goes up, the state of the system changes gradually from a dense crystalline phase to a fluid phase, and finally to a gaseous phase, which we saw in Fig. 3.9A and B. For clarity, we have plotted the number density as a function of the height in Fig. 3.10A. For $z < 10\mu m$, a lot of fluctuations is seen in the number density which is due to the layering of the particles parallel to the bottom of the sample chamber. Then, between $10 < z < 50\mu m$, the number density remains roughly constant, corresponding to the crystalline phase observed in Fig. 3.9. Between approximately $50 < z < 85\mu m$ there is a slow decay in $\rho(z)$ as we enter the dense fluid region of the stack. Above $z = 85\mu m$, we see a short exponential decay, reflecting Eqn. 3.1, before the number density falls to zero.

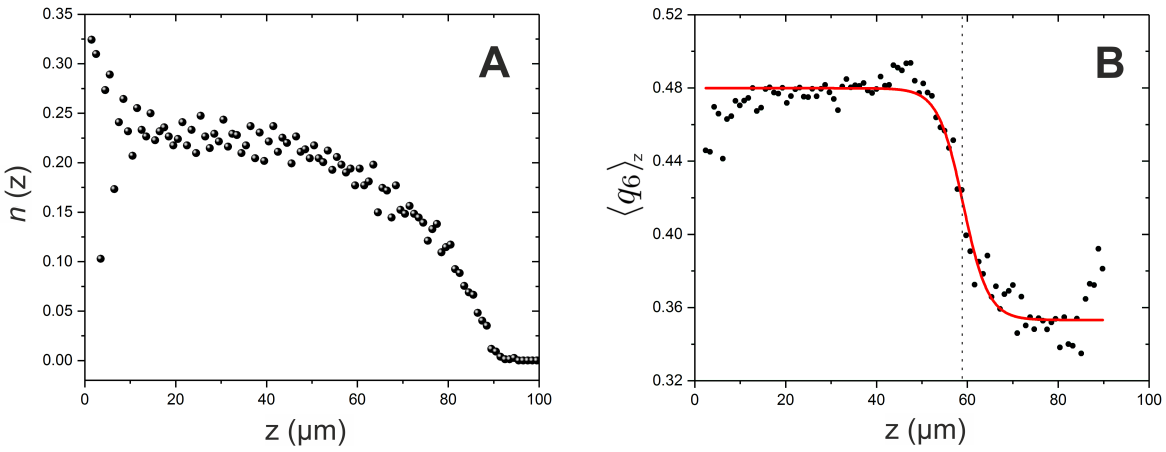


*Figure 3.10: (A) Number density of the z-stack as a function of z-height. (B) Averaged local bond order parameter for particles in each bin in z, plotted as a function of height (•) and fitted with a tangent hyperbolic function (—) in red.*

The transition from the crystal phase to the liquid phase can also be quantified by calculating the local bond (Steinhardt) order parameter, $q_6$, as a function of $z$ [126]. This is independent of the reference frame and is based on spherical harmonics, and gives a good indication of the extent of hexagonal packing in the sample. For a single particle $i$, the local bond order parameter is defined as:

$$q_6(i) = \sqrt{\frac{4\pi}{13} \sum_{m=-6}^{6} |q_{6m}(i)|^2}, \tag{3.4}$$

where:

$$q_{6m}(i) = \frac{1}{N_b(i)} \sum_{j=1}^{N_b(i)} Y_{6m}(\mathbf{r}_{ij}). \tag{3.5}$$

Here, $N_b(i)$ is the number of nearest neighbours for particle $i$, and $(\mathbf{r}_{ij})$ is the vector between particles $i$ and $j$. $Y_{6m}(\mathbf{r}_{ij})$ are the spherical harmonics with integer values of $-6 \leqslant m \leqslant 6$. By summing over all the $q_6$ values for all the particles in a given bin in $z$ and taking the average, (i.e. $\frac{1}{N}\sum_{i=1}^{N} q_6$), we obtain a profile of $\langle q_6 \rangle_z$ as a function of height. This is plotted in Fig. 3.10B for our z-stack and is fitted with a tangent hyperbolic function, which highlights the transition between the crystalline and fluid regions. In Fig. 3.10B, the profile of $< q_6 >_z$ appear mostly flat between $10 < z < 50\mu m$ and is fairly high in magnitude, indicating a high level of hexagonal packing in this sample region. Between $50 < z < 70\mu m$ there is a large drop in $< q_6 >_z$ value, which indicates decreasing hexagonal packing, i.e. decreasing crystallinity of the TPM spheres. For $z < 70\mu m$, there is a short persistence of $\langle q_6 \rangle_z$ around 0.35, before poor statistics of the dilute gaseous phase comes in around $z = 80\mu m$. Analytically, the midpoint of the sudden drop in $\langle q_6 \rangle_z$ can be seen as the crystal-fluid interface of the sample, or the freezing transition point. For the sample in Fig. 3.10B, this occurs at $59\mu m$, which corresponds to a number density $n \approx 0.21$ in the stack (see Fig. 3.10A), which means the volume fraction of the freezing transition occurs at $\phi \approx 0.42$ (Fig. 3.11 inset). This deviates from the predicted hard-sphere freezing transition at $\phi_{HS} = 0.49$, and can be attributed to the soft charged particle interactions in our system. It is worth noting here that the calculation of the volume fraction $\phi$ is extremely sensitive to the exact particle diameter (we used $R_{SLS}$ here) and the total sample volume [127].

For $\phi(z)$ in the limit of $\phi \to 0$, we use Eqn. 3.1 to calculate the gravitational length $z_0$, since the particle packing density can be modelled by the barometric height distribution, Eqn. 3.1. Once $z_0$ is known, we can use the following expression for the gravitational length for a spherical particle to work

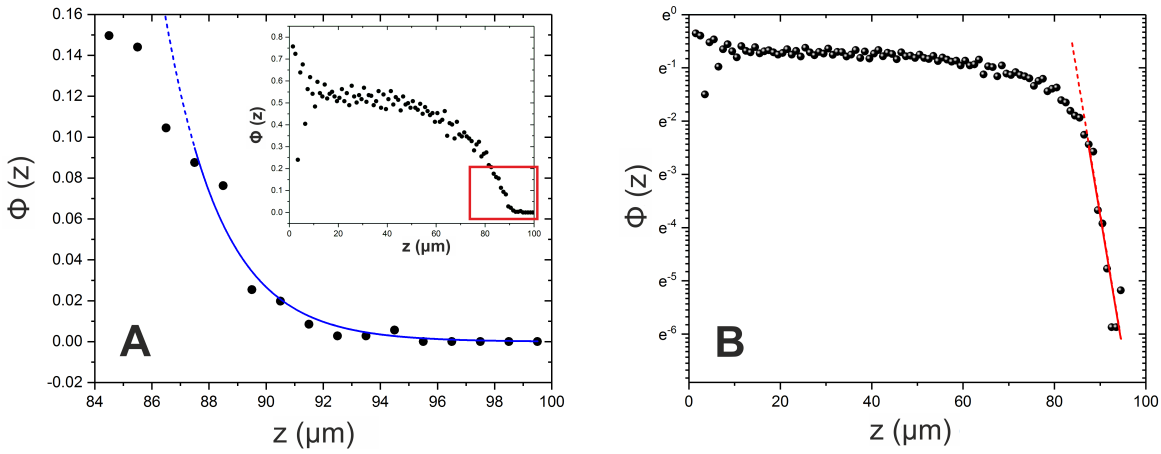


*Figure 3.11: (A) Enlarged area of the inset showing exponential decay of the packing fraction at dilute regions (•). Inset: full sedimentation profile of the z-stack shown in Fig. 3.9A. (B) The same sedimentation profile is plotted in full (•) on a natural log scale. Both plots are fitted individually to Eqn. 3.1 for the low $\phi$ region.*

out the mass density of the TPM particles:

$$z_0 = \frac{k_B T}{(\Delta\rho)(\frac{4}{3}\pi r^3)g}. \tag{3.6}$$

Due to the near density matching of the particles in our 3D system, the decay in the packing density as a function of height is relatively slow in the fluid region, as is shown in Fig. 3.10A. By fitting an exponential function of the form of Eqn. 3.1 to this part of the sedimentation profile, we can obtain a value for $z_0$. This is done on the tail region of the sedimentation-diffusion equilibrium profile shown in Fig. 3.10A, which is plotted in Fig. 3.11A. From this we obtain a value of $z_0 = 1.98\mu m$ for the TPM sample. To check for consistency, we also replotted Fig. 3.10A on a logarithmic scale (Fig. 3.11B) and performed a linear fit on the same $z$ region as Fig. 3.11A. This also gave a value of $z_0 = 1.95\mu m$. Therefore using Eqn. 3.6, the mass density of the TPM particles is $1.30 g cm^{-3}$. This confirms our estimation of the TPM density earlier in Section 3.4.1 using the TPM growth profile.

The equation of state at a given height in the system is related to the integral of the weight being supported there [128]. At a given height in a sample, the associated osmotic pressure $\Pi(z)$ varies in height as $d\Pi/dz = -\rho g$. Given that the mass density $\rho$ is related to the number density (thereby the volume fraction), $\rho = m^* n(z)$ becomes $\rho = m^* \phi(z)/v_p$. Therefore the equation of state becomes:

$$\Pi(z) = \Delta\rho g \int_z^\infty \phi(z) dz. \tag{3.7}$$

Using the expression we have for the gravitational-length (Eqn. 3.2) in a colloidal system, the equation

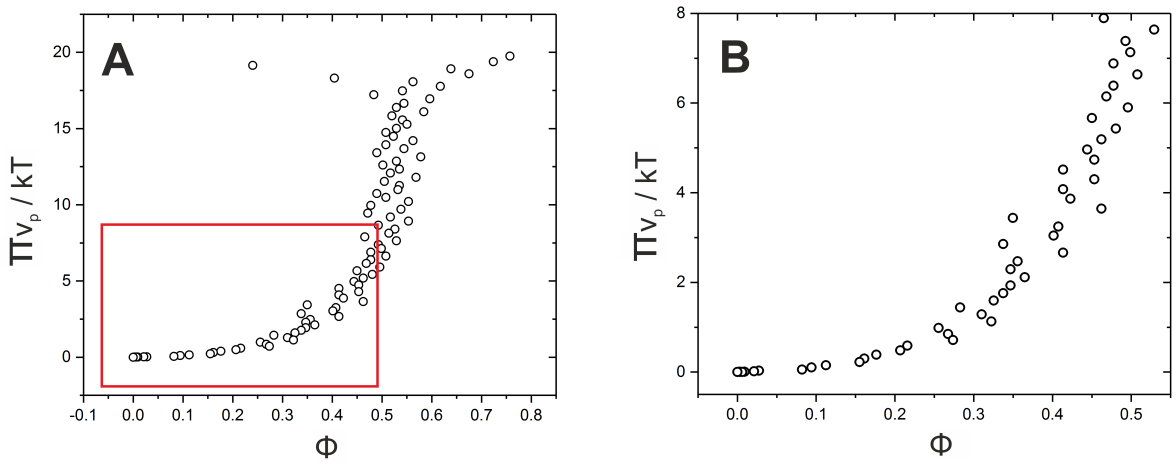


*Figure 3.12: Equation of state multiplied by the particle volume for: (A) the entire stack. (B) the highlighted area of (A), which corresponds to the fluid region as determined by $\langle q_6 \rangle_z$.*

of state can be written as:

$$\frac{\Pi(z)v_p}{kT} = \frac{1}{z_0}\int_z^\infty \phi(z)dz \tag{3.8}$$

Using the data we have obtained from the z-stack, the full equation of state has been plotted in Fig. 3.12A. As expected from the $\langle q_6 \rangle_z$ analysis, the solid-fluid transition in the z-stack occurs at around $\phi = 0.42$. The region in Fig. 3.12A corresponding to the fluid and the freezing transition is shown in Fig. 3.12B. We attribute the difference in the freezing transition of the TPM system with that of a hard-sphere system to the charged interaction between the TPM particles (in the refractive index matching solvent), which is consistent with simulations of Yukawa systems [90].

### 3.4.4 Dynamics of TPM particles as a function of height

As well as the changes in the phase behaviour, the change in the volume fraction of the TPM particles as a function of height also greatly influences the dynamics of the particles. We can see this by examining the mean squared displacement (MSD) of particles at different heights in the sample. This was done for the same data that was shown in Fig. 3.9A at four different heights: (a) $10 < z < 30\mu m$, (b) $30 < z < 50\mu m$, (c) $50 < z < 70\mu m$, and (d) $70 < z < 90\mu m$. This spans all the phases in the system, which allows for clear comparison of the dynamics and the structure. The MSDs were calculated directly from the particle trajectories using

$$\langle r^2(t) \rangle = \frac{1}{N}\sum_{i=1}^{N} \left\langle [\mathbf{r}_i(t) - \mathbf{r}_i(0)]^2 \right\rangle, \tag{3.9}$$

with $N$ the number of particles, and $\mathbf{r}_i$ the position of the particle $i$. The MSDs are shown in Fig. 3.13 for the four different heights in the z-stack. The average packing fraction $\phi$ for each of the curves are given in the plot legend.

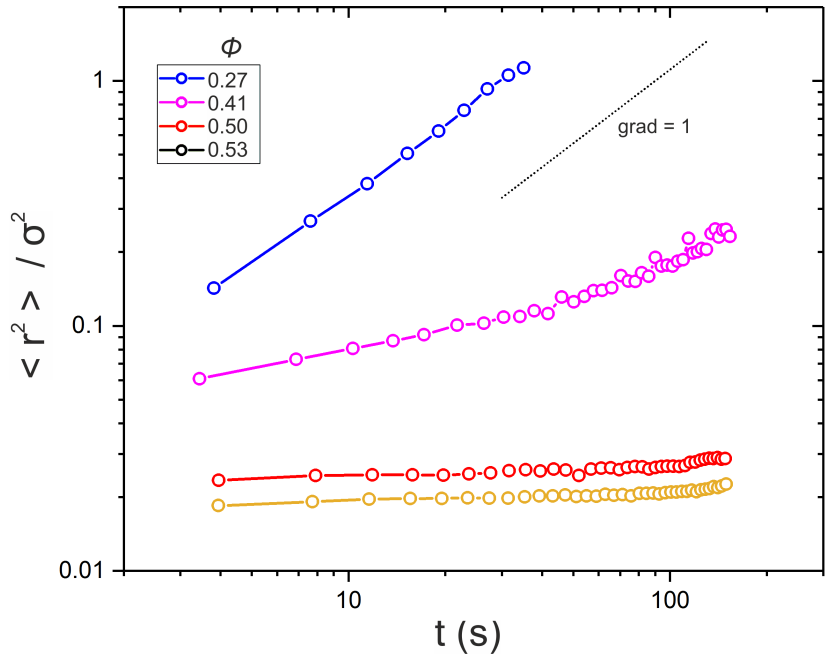


*Figure 3.13: Mean squared displacement of TPM particles corrected by particle size, corresponding to four different heights in z from the sedimentation-diffusion equilibrium profile shown in Fig. 3.9D. The average packing fractions $\phi(z)$ over the course of the experiment for each of the 3D substacks are given in the plot legend.*

Due to limited imaging speed, we were unable to probe the MSD below time lags of $\sim 3$ seconds. Therefore only the MSDs for the intermediate time range are examined, although we would have expected to see diffusive behaviour at very short time scales. From Fig. 3.13 we see that with decreasing volume fraction, the particles become increasingly diffusive. For $10 < z < 30\mu m$ ($\phi = 0.53$), and $30 < z < 50\mu m$ ($\phi = 0.50$), the mean squared displacement profiles are flat and relatively independent of the time lag $t$. As we know from Fig. 3.9C and D and the analysis of the bond-order parameters, the sample is crystalline in the region between $10 < z < 50\mu m$., which is consistent with the plateau in the MSD of the particles. However for $50 < z < 70\mu m$ ($\phi = 0.41$), whose packing fraction is near that of the freezing transition point, the MSD is now sub-diffusive. This indicates that the motion of the particles are less restricted here than in the crystalline region in the intermediate time regime, though there is still a good degree of structure in the local packing which restricts the motion of a typical particle. We also observe a slight upward trend near the end of the MSD for this packing fraction, which suggests that the dynamics may become diffusive again at larger time scales. Lastly, for particles in the more dilute fluid region between $70 < z < 90\mu m$ ($\phi = 0.27$), the MSD is fully diffusive as expected.

## 3.5 Conclusions

In summary, we have developed and characterised a refractive-index and density matched 3D colloidal model system that is suitable for quantitative 3D confocal laser scanning microscopy. The TPM colloidal particles have been characterised using brightfield, static light scattering and scanning electron microscopy. We have investigated the effect of the reaction pH and the starting TPM concentration on the the size and polydispersity of the particles. The procedure for finding the refractive index of the TPM particles has been described, along with the solvent transfer process used to move particles into low dielectric mediums. Finally we have examined the sedimentation-diffusion equilibrium of the TPM model system and discussed the structural arrangement and the dynamics of the colloids as a function of the sample height and packing fraction.

**Acknowledgments**

This work was done in collaboration with Stefano Sacanna, Kazem Edmond, Arran Curran and Taiki Yanagishima.

# Chapter 4

# Core-shell particles for simultaneous three-dimensional imaging and optical tweezing

ABSTRACT

This chapter details the development of core-shell particles for optical trapping in an refractive index matched dense colloidal system of 3-trimethoxysilyl propyl methacrylate (TPM) particles. The two-step coating procedure for the synthesis of the core-shell particles is discussed, and the versatility of the method is demonstrated by coating seed particles of polystyrene (PS), melamine formaldehyde (MF) and TPM. The effects of reagent quantity and the starting core size on the core-shell morphology (size and shell thickness) are investigated, and the particles are characterised using digital holographic microscopy (DHM) and optical tweezing. Finally, the capability and suitability of our core-shell particle for simultaneous optical trapping and confocal imaging in 3D is demonstrated by dragging a polystyrene-TPM core-shell probe particle through a dense crystal of TPM colloids.

## 4.1 Introduction

Colloidal suspensions of microspheres have been used as idealized yet accurate physical models of complex phase behaviours for over a century [30, 105, 107, 129]. The earliest and perhaps most significant example of colloids as atomic models is Jean Perrin's experiments from the early 1900s, where his quantitative measurements of Brownian diffusion confirmed Einstein's theory of diffusion, thereby solidifying Boltzmann's statistical mechanics [105]. Since then, model colloidal suspensions have provided fundamental insights into a wide range of phase transitions [30, 107]. Early investigations of dense colloidal phases used light-scattering techniques to probe deep within the sample, providing a wealth of information about the material's internal structure and dynamics, but as an ensemble average [106, 108]. More recently, by using solvent mixtures that match the particles' refractive index and mass density, powerful 3D imaging techniques, such as confocal microscopy, enabled the direct real-space and time-resolved study of the colloidal material's complex structural and dynamical properties at the single particle level [61, 111]. This allowed unprecedented access to the local processes involved in condensed matter phenomena such as crystallization, glass formation, and gels [108–110].

Moving beyond simple observations, researchers have begun to probe colloidal materials directly by manipulating individual particles using optical tweezers [54, 101]. However, simultaneous optical manipulation and 3D visualization of dense colloidal samples poses significant technical challenges due to their conflicting requirements [65, 71–74]: while 3D visualization requires optical transparency, optical tweezing and manipulation requires a refractive index contrast between the probe particles and solvent. A desirable solution would be a core-shell 'probe' particle where the core diameter, shell thickness, and their respective refractive indices could be controlled independently. As such, the core size and refractive index could be tuned sufficiently for reliable optical trapping, yet interfering minimally with the visualization of the surrounding sample, whilst the shell's thickness could be adjusted as required yet remaining optically transparent. Although there have been numerous reports on the synthesis of core-shell particles [130–137], none describes how to fabricate micron-sized particles with a thick shell, appropriate for both confocal imaging and optical trapping in dense materials.

A commonly encountered challenge in seeded emulsion polymerization is that core particles may get kinetically trapped at the oil-water interface due to the large pinning forces involved [138, 139]. However, a recent study of seeded emulsion polymerization using 3-trimethoxysilyl propyl methacrylate (TPM) [37] shows that at relatively low concentrations, hydrolysed TPM (hTPM) can form evenly sized 'lobes' on the surfaces of the core particles under basic conditions. These lobes can be polymerized

into TPM, resulting in raspberry-shaped particles. Based on this, we introduce a simple, yet robust and general approach involving a two-step heterogeneous nucleation procedure to encapsulate a variety of different core particles within a thick uniform shell.

In this chapter, we repeat the seeded emulsion polymerization with TPM using the raspberry particles as 'seeds', where the nucleated TPM droplets fill the lobe interstices that, when polymerized, yield a smooth uniform TPM shell. The core size and TPM shell's thickness can be independently tuned. Most importantly, the optical contrast of the core-shell particle can be controlled by using cores of different materials, such as melamine-formaldehyde (MF), polystyrene (PS), and TPM. As such, the size and refractive index of the core can, independent to the shell thickness, be optimized for optical tweezing [140]. By dispersing our optical core-shell particles in a host system of fluorescently labelled TPM particles (Chapter 3), hence ensuring identical interactions between all particles, and subsequently refractive index matching the TPM with an appropriate solvent mixture, we achieve a new colloidal system that enables simultaneous 3D confocal microscopy and optical manipulation. We demonstrate this capability by dragging a core-shell 'probe' particle through a dense colloidal crystal of TPM 'host' spheres using holographic optical trapping, whilst the surrounding 3D crystal is imaged at high speed by confocal microscopy.

## 4.2 Experimental methods

### 4.2.1 Materials

3-(Trimethoxysilyl)propyl methacrylate (TPM, Polysciences Inc.), styrene (Sigma-Aldrich, ≥ 99%), 3-aminopropyl trimethoxysilane (APS, Aldrich, 97%), $\alpha$-azo-iso-butyronitrile (AIBN, BDH, UK), ethanol (Sigma-Aldrich, ≥ 99.8%), polyvinylpyrrolidone (PVP K15, MW 10,000, Sigma-Aldrich), ammonium hydroxide solution (28% $NH_3$ in $H_2O$, Sigma-Aldrich, ≥ 99.99%), and Fluorescein 5-isothiocyanate (FITC, Sigma, ≥ 90%) were used as supplied. The fluorescent monomer RITC-APS (rhodamine B isothiocyanate aminopropyl trimethoxysilane) was synthesized according to the procedure described by Ivell et al. [121] in dimethyl sulfoxide (DMSO, Sigma-Aldrich, ≥ 99.5%). NBD-MAEM (4-methylamino ethylmethacrylate-7-nitrobenzo-2-oxa-1,3-diazol) was prepared as described by Bosma et al. [112]. Ultrapure water (Type I) was used for all experiments, and was obtained directly from Milipore Direct-Q®3 purification system.

### 4.2.2 Preparation of seed particles

Polystyrene (PS), RITC labelled TPM and Melamine Formaldehyde (MF) core particles are prepared prior to the core-shell particle synthesis. Polystyrene (PS) seeds are made by combining two separate mixtures of PVP K-15 (6.25% w/w) in ethanol, and AIBN (0.08% w/w) in styrene (15.6% w/w) under nitrogen atmosphere, then allowed to react for 24 hours at 70°C [42]. Melamine formaldehyde (MF) seeds are prepared according to the procedure described by Wu et al. [141], and can be made fluorescent by the addition of minute quantities(~2mg) of RITC or FITC powder to the prepolymer solution. Fluorescent TPM cores are prepared in the same manner as the TPM host particles described in Chapter 3. Each batch of seed particles were cleaned by repeated sedimentation and redispersion in deionised water for at least three times before storage in deionised water.

### 4.2.3 Core-shell particle synthesis

The core-shell particles are fabricated by nucleating and polymerising TPM oil on the surface of the seed particles. In a 30 mL glass vial, a solution of hydrolysed TPM oil (hTPM) is prepared by stirring TPM oil in water at a 1:30 (v/v) ratio with a magnetic stir-bar overnight. In a typical 30 mL reaction (~pH10), core particles (overall concentration of $\approx 10^8$ particles/mL), 30 $\mu$L NH3 and 2 mL hTPM solution are well-mixed with water by vigorous shaking. The reaction mixture is then covered and left undisturbed for 30 minutes before 50 mg AIBN is added, then transferred to a sealed 30 mL glass bottle and placed in a pre-heated 75°C oven for 5 hours to be polymerised. The product particles are cleaned in deionised water for at least three times by repeated centrifugation at 800rpm, decanting and re-dispersion, via gentle sonication and stirring. Secondary TPM nuclei are also removed during this process. The size of the raspberry lobes can be tuned by adjusting the concentration of hTPM solution added initially.

Similarly, in the second TPM coating stage, raspberry particles ($\approx 10^5$ particles/mL) are mixed in a 30 mL aqueous reaction mixture containing 30 $\mu$L NH3 and 5 mL hTPM solution. The final TPM shell is polymerised as before: the reaction mixture is covered, left undisturbed for 30 minutes, 50 mg AIBN is added, and the solution is then transferred to a sealed 30 mL glass bottle and placed in a pre-heated 75°C oven for 5 hours. The resulting core-shell particles are again cleaned in water by repeated centrifugation, decanting, and re-dispersion, as described above. Any secondary TPM particles are, as before, removed by repeated decanting.

### 4.2.4 Digital holographic microscopy

In-line digital holographic microscopy is used with 405 nm laser trans-illumination [96]. A very dilute suspension of the particles in water is prepared, then a single particle is trapped in a strong optical trap such that its displacement from the trap centre is minimised. Whilst dragging the particle along the x-direction at $1\mu m/s$, we record a video at 250 fps. The video is then normalised by the median of all frames. The mean of all frames, with each frame centred on the particle, gives the images presented in Fig. 4.9. The DHM images are analysed using HoloPy software [97]. First, the x, y, z positions of the particle are found in a fit using arbitrary values for the refractive index $n$ and radius $r$, which have a negligible effect on the resulting coordinates. Next, with the x- and y-coordinates fixed and z given a small exploratory range, the DHM images for the core particles are fitted to find the refractive index ($n_{core}$) and the radius of the core ($r_{core}$). Finally, by then fixing $n_{core}$ fixed and allowing a small exploratory range for $r_{core}$ to account for the slight polydispersity in the core particles - the DHM images for the core-shell particles are fitted to find the refractive index of the TPM shell ($n_{shell}$) and the overall radius of the particle ($r_{particle}$).

### 4.2.5 Confocal microscopy and optical tweezing

We use the confocal microscopy and optical tweezing setup is detailed in Chapter 2 section 2.4.3. To prepare the core-shell particles for confocal imaging, they are thoroughly cleaned and are transferred into the TPM refractive index matching mixture consisting of 45 : 55 tetralin : TCE mixture that contains 1 wt % of OLOA 1200, using the procedure introduced in Chapter 3 section 3.3.5. This is mixed with the refractive index matching TPM sample prepared in Chapter 3 to make the binary colloidal mixture, which is then injected into the special glass sample chamber (Section 2.4.2).

For the tweezing of PS-TPM core-shell particles embedded in a sea of TPM host particles, a single core-shell particle is trapped at 4A intensity and moved to a position $\sim 20\mu m$ above the bottom cover glass, where the TPM host particles are densely packed. Three different tweezing trajectories of the core-shell particles were performed: line, circle, and circular sinosoidal (3D). The confocal images were recorded at 20 frames per second for the time-series.

## 4.3 Results and discussion

### 4.3.1 Particle characterisation

All of the core-shell particles presented in this thesis are synthesised as schematically shown in Fig. 4.1. In the first stage, the core particles are coated in a relatively low concentration hTPM mixture under basic condition to form evenly sized lobes on their surfaces [37]. Polymerisation of the TPM lobes results in raspberry shaped particles (Fig. 4.1), which are then used for the second stage coating. During the second stage, fresh hTPM nucleates on the surface of the raspberry particle and the interstitial spaces between the lobes are filled. Provided that a sufficient quantity of hTPM is used, a thick and homogenous TPM shell will form after radical polymerisation is completed (Fig. 4.1). The different stages of the synthesis can be directly observed using brightfield microscopy, and an example from a PS-TPM core-shell synthesis is given in Fig. 4.2A and B. The large shell thickness and the refractive index difference between the core and the TPM shell ensures that the core-shell structures are easily seen. The TPM shell also appears homogeneous, despite the two-stage coating procedure. It is apparent from these images that there is significant increase in the size of the particles after each stage, and this is further corroborated by the scanning electron microscopy images presented in Fig. 4.2B. It is worth noting that the success rate of the conversion from seed particles to core-shell is very high. Virtually all of the cores are converted into raspberry particles in the first step (Fig. 4.3A), and virtually all the raspberry particles are converted into core-shell particles in the second step (Fig. 4.3B). The exception come in the form of joint coating, where a two raspberry cluster is accidentally incorporated into one large ellipsoidal particle (Fig. 4.3B). Note that small secondary TPM particles also form during the coating procedures due to excess hTPM in the reaction, however they can be easily separated from the raspberry or CS particles by centrifugation.

From SLS measurements on the core particles and the final core-shell particles (Fig. 4.2C), we obtain the ensemble average values for the particle radii and polydispersities. Fitting the SLS data (see

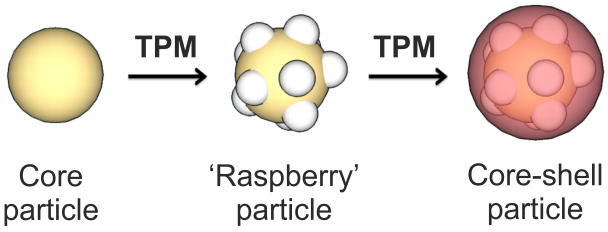


*Figure 4.1: Schematic diagram of the two-step coating procedure of converting a core particle into a core-shell particle with a thick and homogeneous TPM shell.*

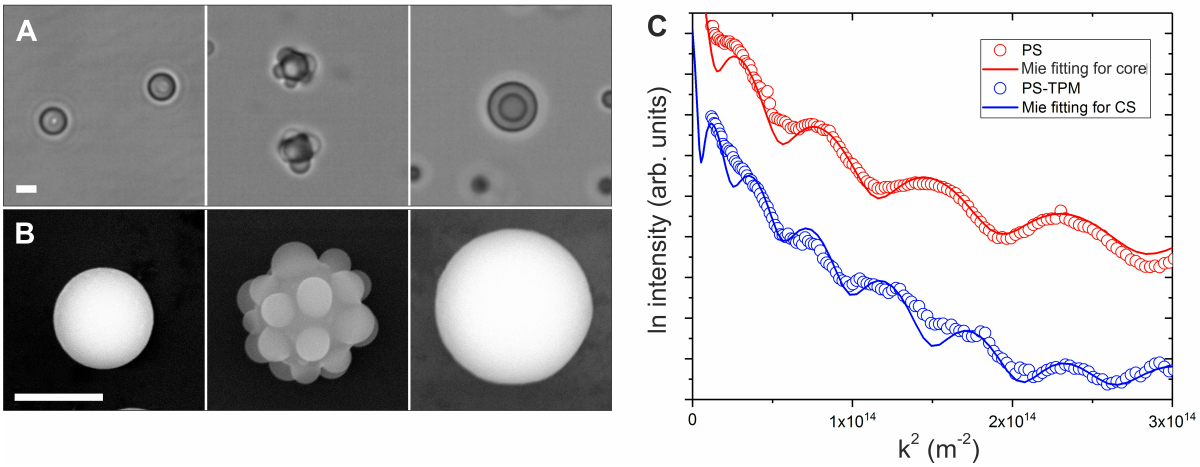


*Figure 4.2: The two stages of the core-shell synthesis as observed under brightfield microscopy (A), and SEM (B) for a PS seed particle. Scale bars = 5µm. (C) Measured SLS data (◯) and calculated Mie fittings (–) for the PS seeds and the resulting core-shell (CS) particles: $r_{PS}$ = 910nm (4%), $r_{PS-TPM}$ = 910nm + 410nm (6%).*

Chapter 2, Section 2.4.1), we obtain for this batch of PS and PS-TPM core-shell the following: $r_{PS}$ = 910nm (4%), $r_{PS-TPM}$ = 910nm + 410nm (6%). These values are slightly larger than their corresponding values obtained from SEM ($r_{PS} = 2.60\mu m$), and can be accounted for mostly by the shrinkage of the particles due to drying and vacuum required for SEM. We also test the core-shell morphology indirectly by comparing its SLS data with the Mie predictions for a homogeneous particles of the same size. However we find that the Mie prediction for a core-shell particle matches the core-shell SLS data more closely, as is shown in Fig. 4.2C.

The two-step mechanism and core-shell morphology is furthermore demonstrated using selective fluorescent labelling of the particle at the various stages of the synthesis. A batch of PS-TPM core-shell particles was synthesised where the core has been labelled with NBD-NAEM fluorophore ($\lambda_{ex}$ =

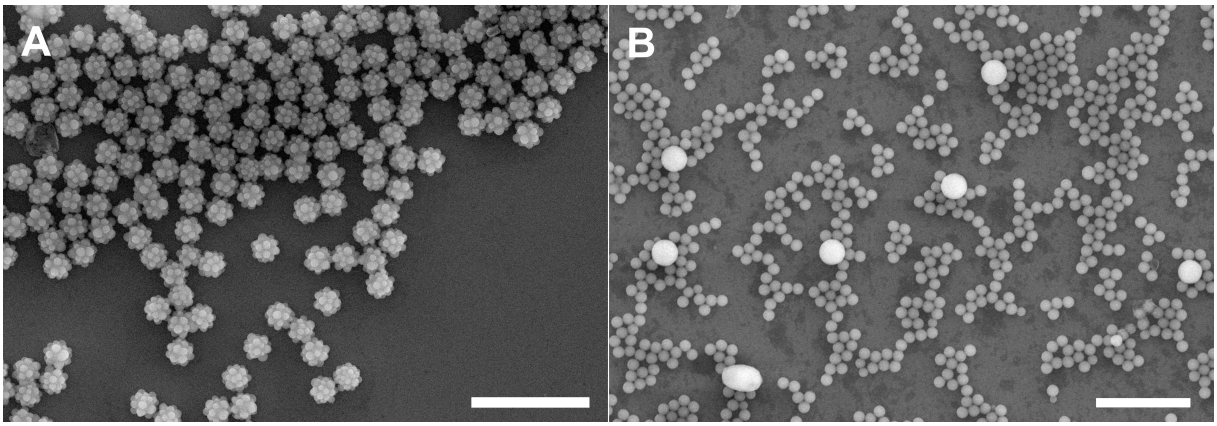


*Figure 4.3: Larger field of view SEM images of Fig. 4.2B, showing: (A) cleaned PS-TPM raspberry particles, and (B) core-shell particles prior to removing the secondary TPM particles. Scale bars = 10 µm.*

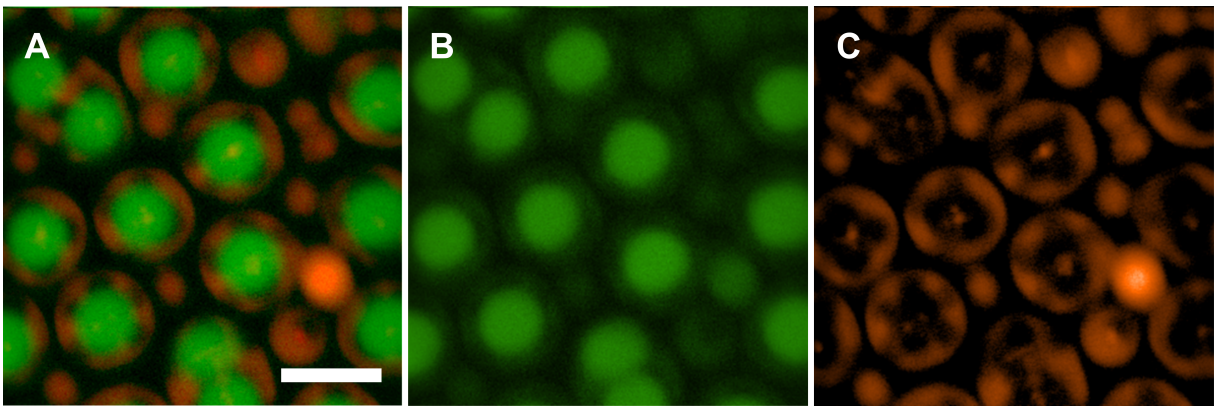


*Figure 4.4: (A) Composite confocal microscopy image showing PS-TPM core-shell particles, where the cores have been labelled with NBD-NAEM and the only the second TPM coating with RITC-APS. The separate detection channels are shown in (B) and (C). Note that the smaller particles seen in (A) and (C) are secondarily nucleated TPM particles. Scale bar = 3 μm.*

488 nm) [112], and the second TPM layer is labelled with RITC-APS ($\lambda_{ex}$ = 561 nm) [112, 121]. No fluorophore was used during the raspberry formation stage. Fig. 4.4A shows a confocal micrograph where this batch of PS-TPM core is simultaneously excited with 488 nm and 561 nm laser light, and Fig. 4.4B and C show the separate detection channels for the two different fluorescence dyes. The different stages are clearly distinguishable: the fluorescent PS cores, and the fluorescent outer TPM layer, which is smooth on the outside but structured on the inside due to the presence of the unlabelled lobes. Note that the red central spots in Fig. 4.4C are caused by the strong back scattering of the high refractive index cores.

Conveniently, due to the nature of the two-stage synthesis, the optical contrast between the core and shell can also be adjusted by changing the core material, thus underlining the generality and flexibility of our approach. Aside from the already mentioned PS cores (n ≈ 1.59), we have also successfully incorporated MF (n ≈ 1.68) and TPM (n ≈ 1.52) cores. This implies that we can tune the refractive index contrast ($\delta n$) between the core and the TPM shell from approximately 0.18 (MF) to 0 (TPM). Examples of MF and TPM core conversions are shown in Fig. 4.5. The optical properties of each particle and their utility for optical tweezing will be discussed in Section 4.2.4.

Similarly, a batch of TPM-TPM core-shell particle is synthesised where only the TPM core is labelled with RITC-APS. As a TPM-TPM core-shell particle is compositionally identical to a homogeneous TPM particle, its core-shell nature is not observable using brightfield microscopy (Fig. 4.6A). However, by fluorescently labelling only the TPM cores, the core-shell structure is easily inferred from the corresponding brightfield and confocal images, as presented in Figs. 4.6B, respectively. The hexagonal close packed nature of the sample means that the separation between the fluorescent cores arises solely from

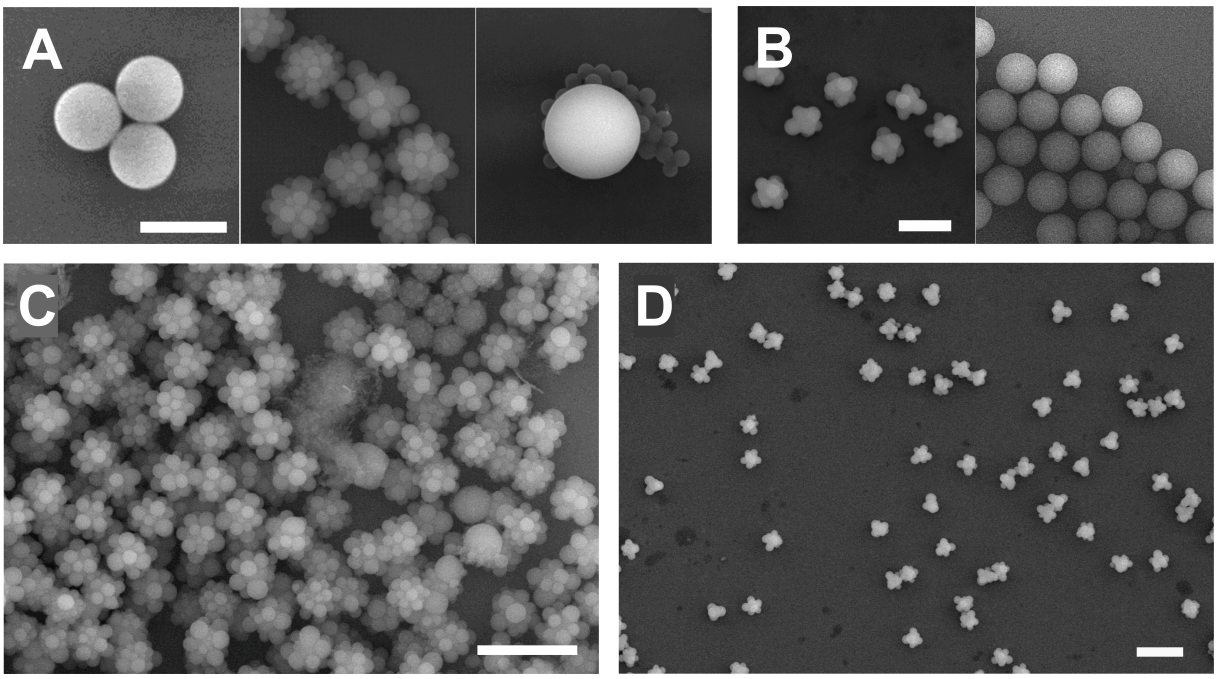


*Figure 4.5: SEM images showing the conversion of: (A) MF seed particles into MF-TPM core-shell particles via the raspberry stage, and (B) the conversion of TPM-TPM raspberry particles into TPM-TPM core-shell particles. Scale bars = 3 μm. (C) and (D) show the large field of view images of the cleaned raspberry particles from (A) and (B) respectively. Scale bars = 5 μm.*

the presence of the non-fluorescent shell. While TPM-TPM core-shell particles are unsuitable for optical trapping when dispersed in TPM refractive index matching solvents, they do present a better alternative to conventional particles for confocal imaging and tracking in dense suspensions.

To further confirm the concentric nature of the core-shell particles and the homogeneity of the shell, PS-TPM and MF-TPM core-shell particles have been calcinated at temperatures above 300°C and 500°C respectively. The high temperature treatment causes the organic components of the core material to disintegrate, whilst the TPM shell decomposes into a silica rich material. Applying mechanical stress to these calcinated particles resulted in some broken, but clearly concentric and homogeneous shells. Examples are shown in Fig. 4.7 for PS-TPM and MF-TPM core-shell particles post calcination and crushing. Significant size reduction is also observed in the shell of the calcinated particles, and could be contributed to the decomposition of the organic material inside.

### 4.3.2 Controlling core size and shell thickness

The size of the core and the thickness of the shell can also be independently controlled in a two-step coating process. This flexibility allows the optimisation of the core particle size for optical tweezing,

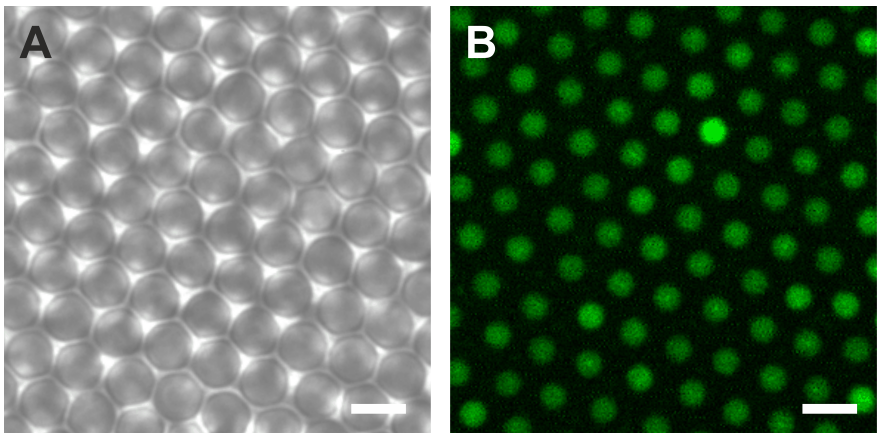


*Figure 4.6: (A) Brightfield and (B) confocal images of closely packed TPM-TPM core-shell particles with RITC-APS labelled cores. Scale bars = 3 μm.*

irrespective of the total size of the core-shell particle. In particular, we find that the final thickness of the shell is essentially controlled by the size of the raspberry lobes. Increasing the hTPM concentration used in the first coating stage leads to a clear increase of the lobe-size of the resulting raspberry particles (Fig. 4.8A), though the number of lobes decreased. However, the lobe-size does not significantly depend on the core-size for a given concentration of hTPM, within the range of core particle concentrations we typically use ($10^8$ - $10^{10}$ particles/mL). This is illustrated in Fig. 4.8B, where raspberry particles with different core sizes were derived from TPM coating a single batch of polydisperse PS cores.

Figure 4.8C shows the effect of varying the hTPM concentration in the second coating stage on the morphology of the final core-shell particle for raspberry particles with two different lobe-sizes. In contrast to the first coating stage, increasing the hTPM concentration in the second coating stage appears to have a limited effect on the overall size increase of the raspberry particles. However it does determine the surface roughness of the final core-shell particles. This is shown in Fig. 4.8C, where raspberry particles with two different lobe-sizes have been coated with various hTPM concentrations and then polymerised. For the raspberry particle with the smaller lobes (left column), a smooth core-shell particle with a shell thickness of ≈600 nm is obtained at a hTPM concentration of 1.4 mM. In comparison, for the raspberry

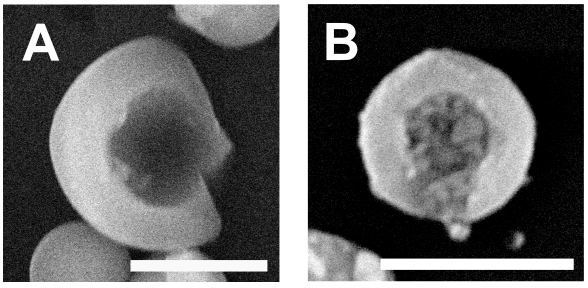


*Figure 4.7: Broken (A)PS-TPM and (B) MF-TPM core-shell particles after calcination. Scale bars = 2 μm.*

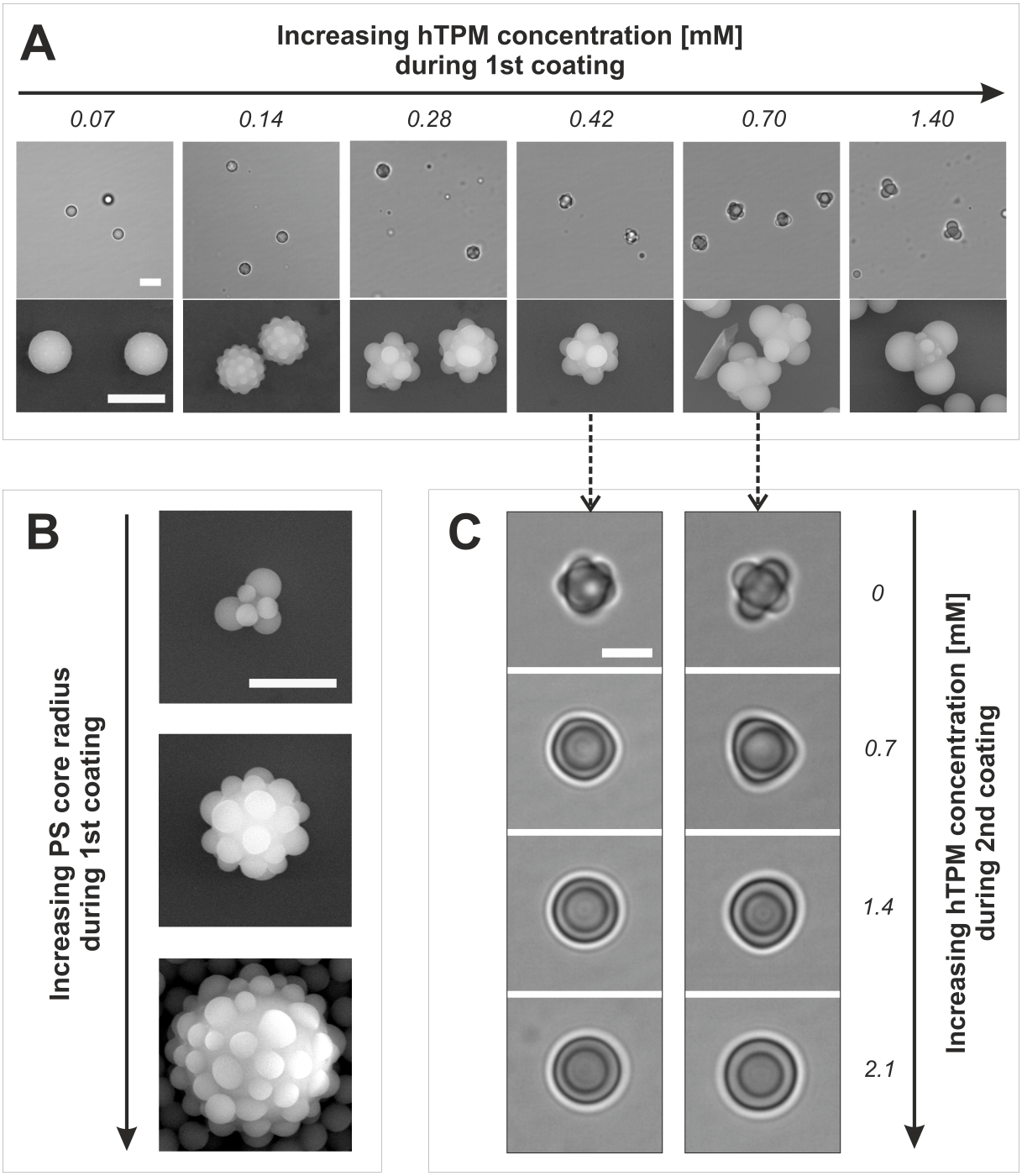


*Figure 4.8: (A) Effects of the hTPM concentration in the first coating stage, as observed by brightfield microscopy (top row) and SEM (bottom row). (B) SEM images of various sized raspberry particles made by coating a batch of polydisperse PS cores at a hTPM concentration of 0.42 mM. (C) Effects of the hTPM concentration on the core-shell particle morphology in the second coating stage. Results are shown for smaller lobed raspberry particles (left column) and larger raspberry particles (right column). Scale bars = 3 µm.*

particle with the larger lobes (right column), a hTPM concentration of 2.1 mM is required to obtain a smooth core-shell particle with a shell thickness of ≈800 nm. At insufficient hTPM concentrations, the lobes protrude out of the second TPM layer, resulting in a rough surface in the final particle.

Overall, we find that the final thickness of the shell is mostly dictated by the size of the raspberry lobes, and that the hTPM concentration used in the second coating stage determines the final roughness of the particle surface. Therefore in order to make make smooth core-shell spheres, the concentration of hTPM needs to be sufficiently high in the second coating, so that all the interstitial space between the lobes are filled.

### 4.3.3 Digital holographic microscopy and optical trapping

To characterise the optical properties of the core-shell particles, we have applied the in-line digital holographic microscopy (DHM) on a TPM sphere, a PS-TPM core-shell particle, and a MF-TPM core-shell particle. The DHM images are shown in Fig. 4.9A-C respectively. We fitted the holograms using HoloPy [97] to find radius of the core, thickness of the shell, and the refractive indices of the particles (Section 4.2.4). The results from the fittings are given in Table 4.1. Using these outputs, we generated simulated holograms with HoloPy, and these are shown as the insets in Figs. 4.9A-C. Visually these match the experimental holograms well.

*Table 4.1: DHM fitting parameters for the holograms shown in Fig. 4.9: refractive indices of the core ($n_{core}$) and shell ($n_{shell}$) are shown, as are the radii of the core ($r_{core}$) and the final particle ($r_{particle}$).*

| Particle type | $n_{core}$ | $n_{shell}$ | $r_{core}/\mu m$ | $r_{core}/\mu m$ | $r_{shell}/\mu m$ [a] |
|---|---|---|---|---|---|
| PS particle | 1.620 | - | 0.915 | - | - |
| PS-TPM core-shell | 1.620 | 1.457 | 0.954 | 1.626 | 0.672 |
| MF particle | 1.679 | - | 0.891 | - | - |
| MF-TPM core-shell | 1.679 | 1.489 | 0.885 | 1.705 | 0.820 |
| TPM-TPM core-shell [b] | 1.481 | - | - | 1.101 | - |

[a] The shell thickness is defined as $r_{shell} = r_{particle} - r_{core}$.

[b] There is only one refractive index for the compositionally homogeneous TPM-TPM core-shell particle.

We also compare each HoloPy fit with the experimental data by calculating the azimuthal averages (plots are given below each hologram in Fig. 4.9A-C). Overall, the positions and the amplitudes of the peaks from each fitting matches closely with the experimental data. The deviation seen in the the peaks near the centre of the particle could be attributed to the effect of the illumination in the optics system. As DHM is highly sensitive to any anisotropy in the particle, a slight eccentricity in the core-shell structure may also contribute to the deviation in the HoloPy fittings. However, as we are able to fit our experimental data well, this method of particle characterisation therefore further attest to the concentric nature of the core-shell particles, as well as the homogeneity in the thickness of the TPM shells.

Next, we characterise the optical tweezing properties of the core-shell particles by trapping MF-TPM and PS-TPM core-shell particles of comparable sizes, which are dispersed in a solvent medium

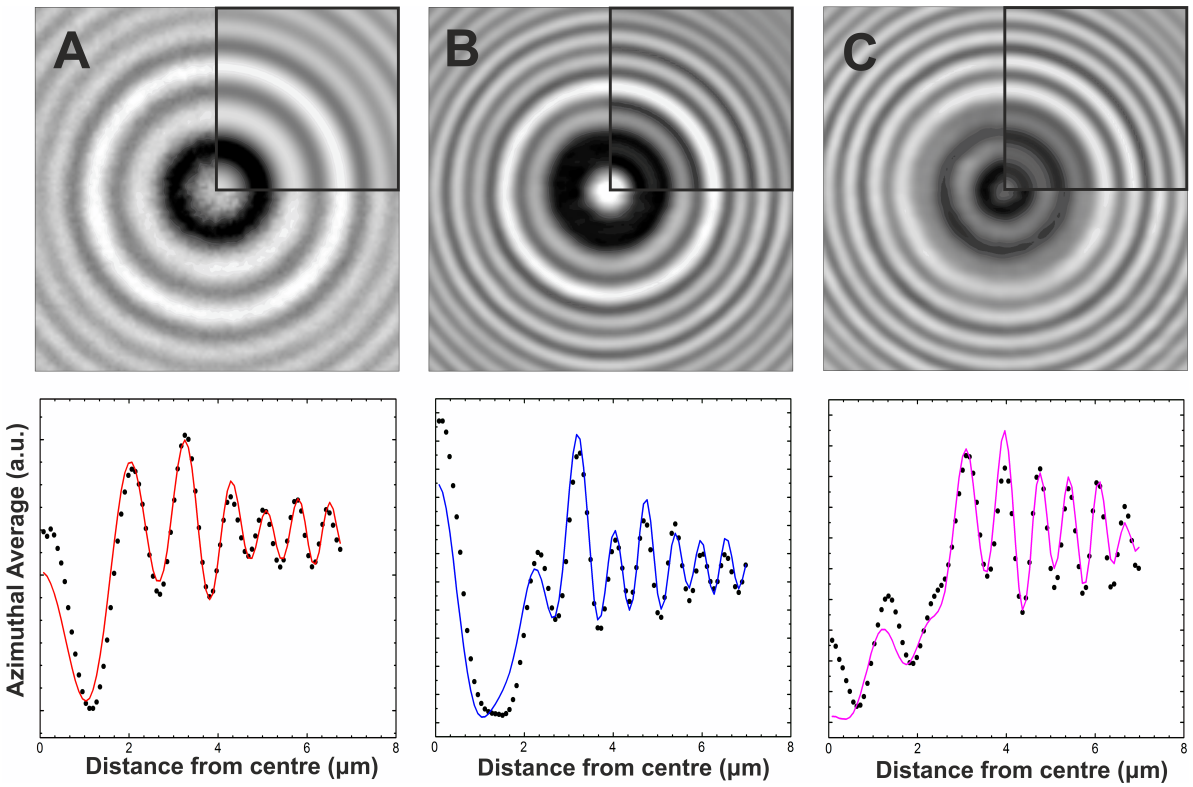


*Figure 4.9: Experimental DHM images of (A) a TPM particle; (B) a PS-TPM core-shell particle; and (C) a MF-TPM core-shell particle in water. Insets (upper right quadrants) shows fitted holograms using HoloPy [97]. The corresponding azimuthal average plots are shown below each hologram for the real data (·) and the fitted data (−).*

with a refractive index that matches with TPM (see Chapter 3). The corresponding trapping potentials are shown in Fig. 4.10. For comparison, the trapping potential for a MF core particle is also included. The solids lines are fits according to a parabolic potential $kx^2$, and the trapping stiffnesses are: $k_{MF} = 9.6\mu N/m$, $k_{MF-TPM} = 9.7\mu N/m$ and $k_{PS-TPM} = 5.9\mu N/m$. The higher trap stiffness values for MF and MF-TPM particles are due to the higher refractive index of the MF core compared to the PS core. More importantly, the trapping potentials for MF and MF-TPM particles are nearly identical. Therefore this quantitatively confirms the near perfect refractive index matching of the TPM shell by our binary solvent mixture, and corroborates with our findings in Chapter 3.

### 4.3.4 Simultaneous three-dimensional confocal microscopy and optical tweezing

Finally, to demonstrate the simultaneous 3D imaging and optical trapping capability of our new colloidal system, we drag a single core-shell probe particle through a dense crystalline region of fluorescent TPM host particles. The solvent mixture's ratio is adjusted to allow for a slight density mismatch in order to sediment the particles and permit the formation of a large crystalline domain, yet still maintain good

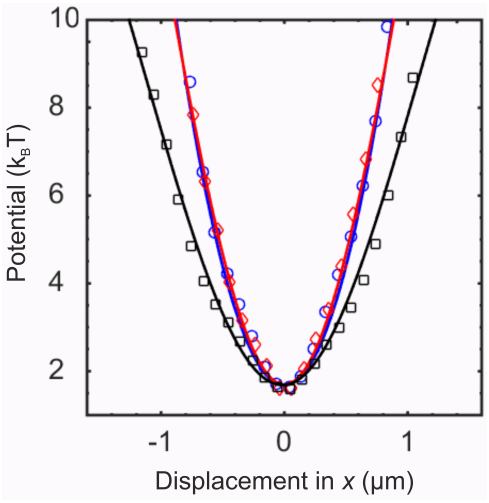


*Figure 4.10: Optical trapping potentials for a MF particle (◇), a MF-TPM core-shell particle (□), and a PS-TPM core-shell particle (◯) in a R.I. matching binary solvent mixture. The solid lines are fits according to a parabolic potential of $kx^2$.*

optical clarity for quantitative 3D confocal imaging deep within the sample. Using the hybrid optical trapping - confocal microscopy set-up [71] detailed in Chapter 2, a single PS-TPM core-shell particles is trapped and dragged through a colloidal crystal in the following geometries: (i) a straight line in the $x/y$ plane, (ii) a circular orbit in the $x/y$ plane, (iii) a sinusoidal trajectory in $z$ along a circular orbit in $x/y$, whilst being imaged simultaneously using high-speed confocal microscopy. Videos of these trajectories are provided in the Appendix using the original confocal data, and are played back at real-time.

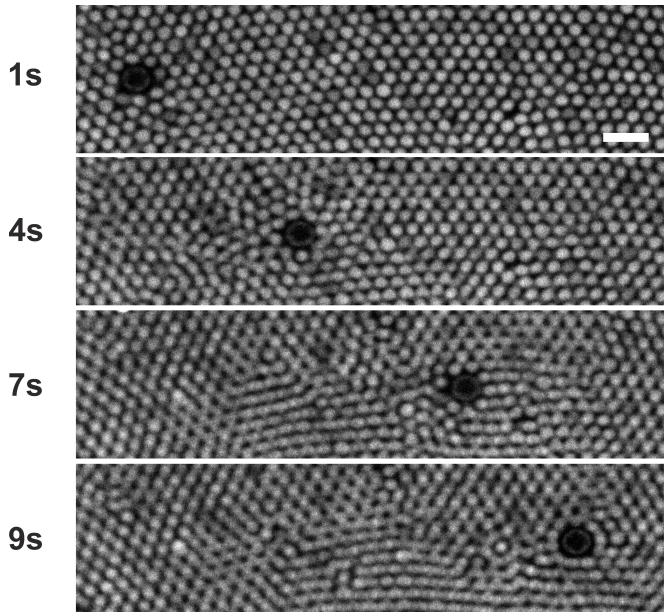


*Figure 4.11: Snapshots from the 2D time-series of a PS-TPM core-shell particle being dragged in a line, through a dense crystalline region of TPM host particles by optical tweezing (See Appendix for the full video). The labels on the left are timestamps of the snapshots from the full video. Scale bar = 5 μm.*

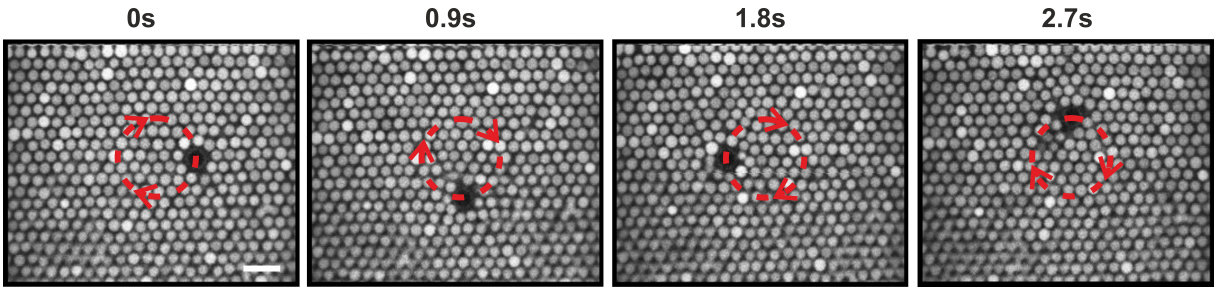


*Figure 4.12: Snapshots from the 2D time-series of a PS-TPM probe particle being dragged in a circular orbit in a crystalline region of TPM particles. Dashed lines (– – –) indicate the clockwise motion of the core-shell particle. Scale bar = 5 μm.*

For the line trajectory (i), a 2D time series was taken where the PS-TPM core-shell probe particle was dragged through a crystalline region of the TPM host particles at a constant speed of $\sim 6\mu m/s$. Snapshots from the time series is shown in Fig. 4.11 where the particle has been dragged from its starting position at $t = 1s$ to the final position at $t = 9s$. We see that the optical tweezer only 'picks up' the core-shell particle in this binary colloidal mixture, and has no effect on the surrounding TPM host particles. As the particle is dragged through the TPM crystal, the regular hexagonal packing of the host particle around it is disrupted (Fig. 4.11), but it is recovered once the core-shell particle has been moved further away. Note that during the time-series, the TPM sample has moved slightly out of the focus of the imaging plane, therefore the host particles appear less well defined towards the end of the experiment. Similarly the effect of host particle rearrangement around the core-shell probe particle is also seen in (ii), the PS-TPM core-shell particle is moved in a circular clockwise orbit (Fig. 4.12). A full revolution of the particle takes $\sim 3.6s$, which can be seen in the full video included in the Appendix.

Particle data from trajectory (iii) is represented in Fig. 4.13, which demonstrates the independent optical tweezing control and the high-speed confocal imaging in all three dimensions. A 3D reconstruction of the confocal data from the region of interest is shown in Fig. 4.13A, where the core-shell particle's trajectory is centered inside a 15 x 15 x $10\mu m^3$ block of TPM colloidal crystal. The coordinates of the TPM particles are detected and tracked using the method detailed in Chapter 2 section 2.4.4, and a computer generated rendering is shown in (B) using the particle coordinates at t = 0. The schematic of the trajectory of the core-shell particle is also drawn in (B) for clarity, where the positions of the core-shell particle at the top (blue), middle (red) and bottom (green) of the trajectory are represented with spheres. The time projections of the different cross-sections in $z$ can also be compiled using the minimum pixel values within each frame, giving rise to the images shown in Fig. 4.13C-E. The dark circles indicate the positions of the core-shell probe particle at different times in its 3D trajectory. A full video of the dragging of the core-shell particle through the 3D colloidal crystal is provided in the Appendix. These

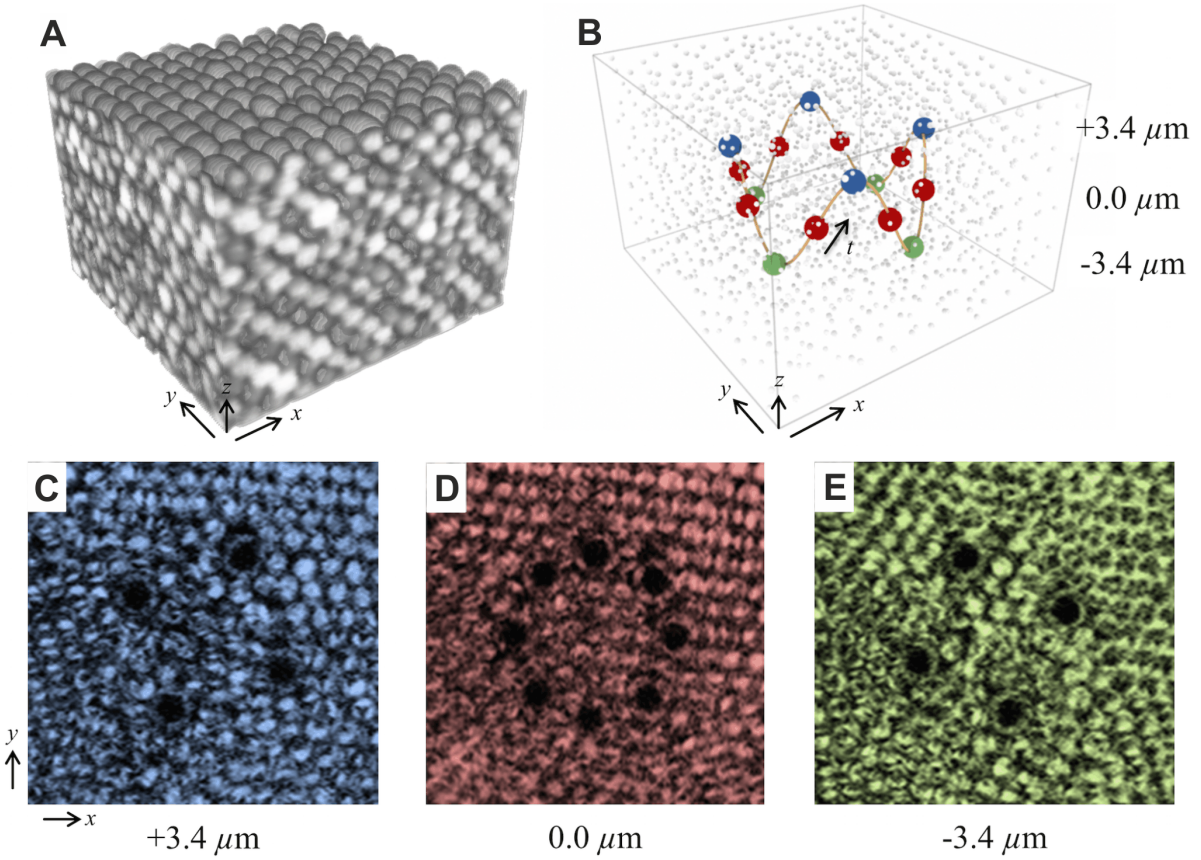


*Figure 4.13: Simultaneous 3D imaging and optical tweezing of a core-shell particle in a colloidal crystal. (A) 3D reconstruction of confocal data from sample's region of interest. (B) Computer-generated image using detected particle coordinates: gray spheres represent TPM host particle positions at the initial time, and core-shell probe particle is drawn at its maximum and minimum z-positions along its circular sinusoidal trajectory, which is depicted by the orange line. (C)-(E) Time projections of minimum pixel values for three cross-sections within the region of interest, showing the core-shell particle locations at the (C) top, (D) middle, and (E) bottom of its trajectory. Full video is provided in the Appendix.*

experiments demonstrate the capability of our colloidal system for simultaneous optical trapping and 3D confocal microscopy in dense colloidal materials.

## 4.4 Conclusions

In summary, we have described the development of novel micro-sized core-shell particles that enable simultaneous 3D confocal imaging and optical tweezing by embedding them as 'probe' particles in a dense and optically matched host suspension of fluorescently labelled particles. While the probe's core is made of a high refractive index material, the probe's shell and surrounding host particles are both made of TPM, which can be refractive index and density matched by a mixture of organic solvents, rendering them invisible to the optical tweezer. The core-size and shell-thickness can be independently tuned and we have

further shown the generality and flexibility of our approach by incorporating cores made of melamine formaldehyde, polystyrene and TPM. By dragging a core-shell particle through a dense colloidal crystal, we have demonstrated the unique capability of our new colloidal system for performing quantitative 3D confocal imaging while simultaneously optically trapping, a capacity which we believe will open up a broad range of opportunities to address many outstanding problems in condensed matter science.

## Acknowledgements

This work is done in collaboration with Arran Curran, Kazem Edmond, Bo Peng, Charles Bryant, Stefano Sacanna, and Dirk Aarts. Vinothan Manoharan, David Grier, Theodore Hueckel and Joseph Auslander are thanked for useful discussions.

# Chapter 5

# Direct measurement of the depletion potential in a binary mixture

ABSTRACT

In this chapter, we measure the depletion potential between two large PS-TPM core-shell particles embedded in a sea of small TPM host particles using optical tweezing, whilst simultaneously measuring the 3D structure of the host particles using confocal microscopy. First we measure the direct interaction potential between two isolated core-shell particles. Next a sea of refractive index matched TPM host particles is introduced to the system, and we trap the large core-shell particles at a series of distances to directly obtain the potential of mean force. Lastly the form of the depletion potential, obtained by subtracting the direct pair potential from the total potential, will be discussed in light of the structural arrangement of the host TPM particles surrounding the trapped core-shell particles at various distances of separation.

## 5.1 Introduction

Since Perrin and Einstein [85, 86], Onsager and others [142] have further validated the analogy between colloids and atomic systems [143]. By integrating out the degrees of freedom of the solvent molecules, the interaction between two colloidal particles can be seen as acting through an effective potential. Specifically, integrating out the positions and momenta of the solvent molecules means that the interaction potential of a pair of colloidal particles should be considered as a potential of mean force, and that the presence of the solvent can be treated as a background. It has been shown that the phase diagram of a spherical colloid system sensitively depend on the potential of mean force [144]. As such, it is important for us to understand the underlying reasons and factors which influence this potential.

In 1958, Asakura and Oosawa [145, 146] first reported a theoretical model describing an attractive force between two hard spheres suspended in a solution consisting of dilute macromolecules. This was later confirmed by Vincent et al. [147] and Vrij [148] for colloid-polymer mixtures. The attractive depletion interaction was attributed to the overlap of the depletion zones of the hard spheres, which excludes the presence of small depletants in between them. This results in a net imbalance in the osmotic pressure, which pushes the particles closer together. Importantly, the overlap of the depletion zones results in a net increase in the entropy of the macromolecules, thus lowering the free energy of the system as a whole. Hence depletion interaction is entropic in origin. However, more recent studies [149, 150] have shown that at higher concentrations of the macromolecules in the system, the depletion potential is no longer simply attractive at short inter-particle spacings. Instead, oscillations in the depletion potential have been observed at larger inter-particle spacings, and the magnitude of the oscillation appear to correlate with the packing density of the depletants [149]. This has been attributed to the increase in the ordering of the liquid structure of the small macromolecules as its packing density increases, though direct evidence of their spatial configuration has not yet been acquired.

Experimentally, the inter-particle potential between two individual colloidal particles can be determined using a variety of techniques, including surface force apparatus [151], total internal reflection microscopy (TIRM) [152], colloid probe atomic force microscopy [153] and optical tweezing [154]. In all of these cases except for optical tweezing, the measurement of the pair-potential is limited to isolated particles. Yet, while optical tweezing allows the pair potential to be measured in dense suspensions, the structural arrangement of the bulk colloidal suspension can not yet be easily observed. This is because optical tweezing requires a refractive index mismatch between particles and the solvent, and this conflicts with the optical transparency that is required for 3D confocal imaging.

In this chapter, we use the TPM colloidal model system that was described in Chapter 3 and the core-shell particles from Chapter 4 to overcome the problem of simultaneous confocal imaging and optical tweezing in a dense colloidal dispersion, so that the potential between a pair of core-shell particles embedded in a sea of small TPM particles can be measured. First we determine the direct pair potential between a pair of PS-TPM core-shell particles in a TPM refractive index matching medium by measuring the displacement of the particles from the trap centres and the strength of the optical traps. Next the same procedure is repeated for the trapping of core-shell particles embedded in a sea of small TPM host particles to obtain the potential of mean force. Using both the direct pair potential information and the potential of mean force measurement, the depletion potential is derived. Finally the form of the depletion potential is interpreted and compared with the direct visualisation of the host particle structuring around the core-shell particles.

## 5.2 Background

### 5.2.1 Pair potential

We have seen in the previous chapters that TPM particles experience a soft inter-particle interaction when immersed in the refractive index and density matching solvent mixture, due to screened electrostatic interactions. The typical decay length of the charge screening in a system is given by the Debye length, $\kappa^{-1}$. In the hard-sphere Yukawa (screened Coulomb) model, the interaction potential between particles of diameter $\sigma$ is given by:

$$\frac{U(r)}{k_B T} = \begin{cases} \frac{\epsilon \exp(-\kappa\sigma(r/\sigma - 1))}{r/\sigma}, & \text{for } r > \sigma \\ \infty, & \text{for } r \leq \sigma. \end{cases} \tag{5.1}$$

The parameter $\epsilon$ is the contact value of the pair potential, which is given by:

$$\epsilon = \frac{\lambda_B Z^2}{\sigma(1 + \kappa\sigma/2)^2}. \tag{5.2}$$

Here $Z$ is the effective charge of the particles, and $\lambda_B = e^2/(\epsilon_r k_B T)$ is the Bjerrum length, which represents the separation of the unit charges at $k_B T$. The pair potential can be seen as the reversible work required to bring two particles together at a separation distance of $r$. Simulation studies done by Hynninen et al. have shown that changes in contact value $\epsilon$ and the Debye length $\kappa^{-1}$ greatly influence the phase

diagram of a hard-core Yukawa system [90]. For highly charged colloids with large contact values of $\epsilon$, the crystal-fluid transition occurs at significantly lower hard-core packing fractions than weakly charged colloids. For example, in a point Yukawa particle system with a contact value of $\epsilon = 20k_BT$, if the Debye length is small at $1/(\kappa\sigma) = 0.05$, the crystal-fluid freezing transition would be expected to occur at $\phi = 0.3$. However if the particles are very charged and the Debye length is larger at $1/(\kappa\sigma) = 0.15$, then the freezing transition would be expected to occur at a far lower packing fraction of $\phi = 0.2$. Therefore it is of central interest to directly measure the interaction potentials between two colloidal particles.

### 5.2.2 Depletion interaction

In 1958 Asakura and Oosawa first reported the phenomenon of an attractive force between two hard-spheres when suspended in a dilute solution of macromolecules [145, 146], which was also observed by Vincent et al. [147] and Vrij [148] using colloid-polymer mixtures. This phenomenon is known as the depletion interaction. The macromolecules, which include non-adsorbing polymers and small colloids, are considered as inter-penetrable hard-spheres when interacting with each other and as hard-spheres when interacting with the large colloidal particles [143]. For two colloidal particles of size $\sigma_L$ immersed in a sea of macromolecules of size $\sigma_S$, as shown in $Fig.5.1A$, there is an associated depletion layer of thickness $\sigma_S/2$ around each colloidal particle. Even though the direct colloid-colloid and colloid-macromolecule interactions are repulsive, the overlap of the depletion layers of the two colloids brings about an effective attractive force, due to the increase in the volume available for the macromolecules and the lowering of the overall free energy. As such, the attractive depletion potential between the two large particles at low depletant concentrations can be accounted for by the product of the overlap volume $V_{ov}$ and the osmotic pressure $\Pi = n_b k_B T$, where $n_b$ is the bulk number density of the depletant. This is summarised in the Asakura-Oosawa-Vrij (AOV) depletion potential as:

$$V^*_{dep}(h) = \begin{cases} \infty & h < 0, \\ -\Pi\, V_{ov}(h) & 0 \le h \le \sigma_S, \\ 0 & h > \sigma_S, \end{cases} \tag{5.3}$$

and is plotted in Fig. 5.1B as a function of colloid surface-to-surface separation, $h$. Given that the overlap volume $V_{ov}$ depends on the thickness of the depletion zone $\sigma/2$, we can see from Eqn. 5.3 and Fig. 5.1B that the range of the AOV depletion interaction is determined by the size of the depletant. Similarly, the strength of the interaction is set by the osmotic pressure of the bulk, which depends on the bulk

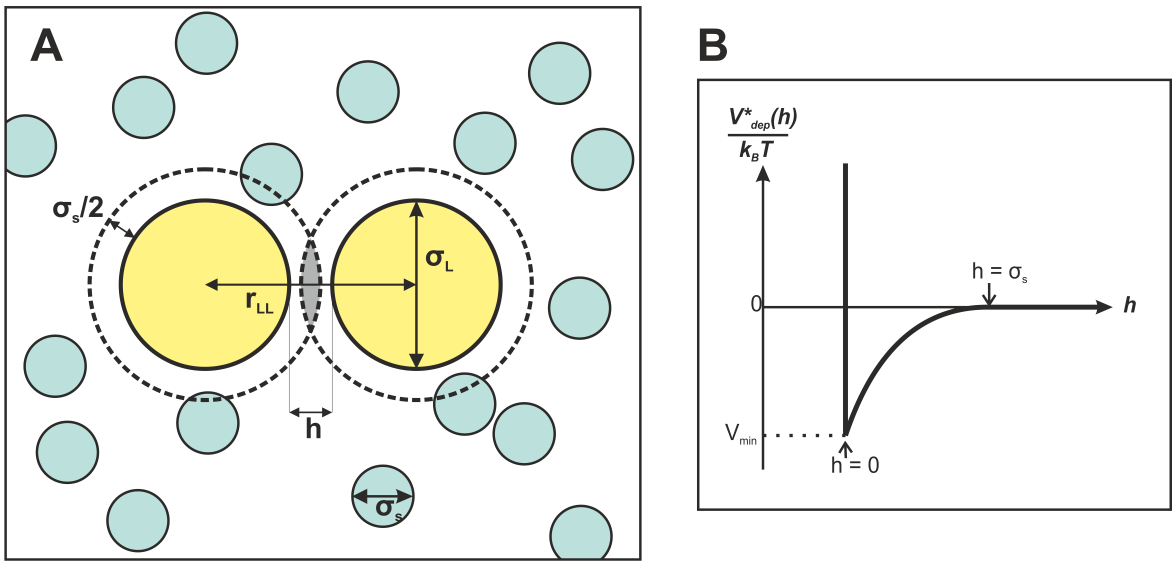


*Figure 5.1: (A) Schematic diagram of two hard-spheres in a sea of small penetrable hard-spheres. The depletion zones are drawn in dashed lines (−−), and the overlap volume is indicated by the shaded region, where the osmotic pressure is lower than that of the bulk, resulting in an attractive depletion potential. (B) AOV depletion potential plotted as a function of the surface-surface separation of the pair of large colloids, h, at low $\phi_S$.*

concentration of the depletant [142, 143].

In the case of a more concentrated solution of macromolecules, AOV theory breaks down, and studies have shown that the depletion interaction ($V_{dep}$) between two colloidal particles in a sea of macromolecules is no longer simply attractive [149, 150, 155]. The oscillatory nature of the potential is now attributed to the structuring of the small macromolecules, though direct visualisation of this has not yet been observed.

### 5.2.3 Potential of mean force

From statistical mechanics, we know that the potential of mean force between two colloidal particles in a mono-disperse colloidal suspension can be determined from the structural information of the host particles:

$$\frac{W_{tot}(r)}{k_B T} = -\ln(g(r)). \tag{5.4}$$

Here, the radial distribution function $g(r)$ conveys the structural information of the small particles, and the potential of mean force $W_{tot}(r)$ is the reversible work required to bring the particle pair together to a separation of $r$ from infinite separation. The potential of mean force, i.e the total effective potential, can

be expressed as the sum of the direct pair potential $U(r)$ and the depletion potential $V_{dep}(r)$:

$$W_{tot}(r) = U(r) + V_{dep}(r). \tag{5.5}$$

In the dilute limit where the packing fraction of the neighbouring particles $\phi \rightarrow 0$, the contribution from $V_{dep}$ becomes negligible and Eqn. 5.5 simplifies to the direct pair potential $U(r)$. It is interesting to note at this point that for a pair of colloids in a solvent, the solvent molecules would also be expected to contribute to the potential of mean force. However as the size of the colloidal particles are several orders of magnitude larger than the molecules, the structuring of the solvent molecules is not felt by the colloids. Therefore the solvent is treated as a continuous medium and contributes a negligible amount to the overall total effective potential. Hence the measurement of the potential of mean force for a pair of colloids in a solvent medium with no other particles around can be seen as their direct inter-particle potential.

However, for a system with high packing fractions of colloids, past experimental and simulation studies have shown that the potential of mean force $W_{tot}$ no longer decreases monotonically as a function of distance of separation $r$ [149, 150, 154]. Therefore the entropic contribution due to the structuring of the neighbouring particles through the increased $\phi$ has a significant effect on the depletion potential $V_{dep}$, and hence $W_{tot}$. By measuring the potential of mean force and knowing the direct pair potential of a particular pair of particles, we can quantify exactly the extent of the contribution from the surrounding particles.

In the case of a binary system, consisting of large particles with size $\sigma_L$ embedded in a sea of small particles of size $\sigma_S$, and with $\phi_L << \phi_S$ (as illustrated in Fig. 5.1), the total interaction potential between a pair of the large particles is given by:

$$W_{LL}(r) = U_{LL}(r) + V_{dep}(r). \tag{5.6}$$

Therefore the structural information of the system can be derived using:

$$\frac{W_{LL}(r)}{k_B T} = -\ln(g_{LL}(r)). \tag{5.7}$$

However, in the limit $\phi_L << \phi_S$, $V_{dep}(r)$ depends predominantly on the structuring of the small particles, and hence the structure of the $g_{LL}$ is expected to have the same oscillation wavelength as that of $g_{SS}(r)$.

## 5.3 Experimental methods

### 5.3.1 Sample preparation

Refractive index and density matching of both TPM particles and core-shell particles are required for simultaneous optical tweezing and confocal imaging to take place. RITC-labelled TPM particles from the batch *yl-01-25A* (Chapter 3, Table 3.2) have been selected as the host particles, with $\sigma_{SLS} = 1.64\mu$m and a polydispersity of 4%. The particles were thoroughly cleaned and underwent solvent transfer into a final solution that consist of 45 : 55% vol tetralin : TCE and 1% OLOA-1200 surfactant. The details of the solvent transfer procedure are described in Chapter 3. Similarly, a bath of PS-TPM core-shell particles ($\sigma_{SLS} = 3.1\mu m$ with a polydispersity of 8%), outer layer labelled with RITC-APS) was chosen as the probe particles, and underwent the same solvent transfer procedure in a separate process.

For the direct pair-potential measurements, a dilute dispersion ($\phi_{CS} < 0.01$) of refractive index and density matched core-shell particles was used. For the measurement of the potential of mean force, both the core-shell and the TPM components are mixed together, and the proportion of the core-shell probe particles is adjusted so that its number density is less than a thousandth of that of the TPM host particles. Finally the sample is inserted into the special glass sample chamber (shown in Chapter 2 section 2.4.2) and left to equilibrate over the course of 48hrs.

### 5.3.2 Optical tweezing and confocal microscopy

The decoupled confocal and optical tweezing setup described in Chapter 2 is used to optically trap the core-shell particles, whilst 3D confocal time-series data is acquired simultaneously. Via the spatial light modulator (SLM), two first-order traps are used to control the positions of the core-shell particles. Once a pair of core-shell particles has been selected, they are moved to a region of the sample chamber away from walls and other core-shell particles. The laser intensity is adjusted so that the pair of core-shell particles is weakly trapped. Subsequently, the distance of separation between the optical traps is systematically varied by the SLM. The trapping stiffness of the optical traps was determined by measuring the displacements of a single trapped core-shell particle from the centre of the trap over the course of 10 minutes. The normalised probability distribution of the particle positions (summed in the $y-$direction) is related to the potential of the optical trap , $U_{trap}$, via $P(x) \sim \exp[-U_{trap}(x)]/k_BT$. By plotting $\ln[P(x)]$ against the particle displacement $x$, and fitting a quadratic equation of the form $kx^2/2$ to the data, we obtain a value

for the trapping stiffness $k$.

For the measurement of the direct pair potential, the core-shell particles are moved to a position roughly $30\mu$m above the bottom cover glass to prevent wall effects. The separation between the two optical traps was set at regular intervals between $3.2 - 4.4\mu$m. Confocal 2D cross-sections through the centres of the core-shell particles are recorded at a frame rate of $120 fps$ using bi-directional scanning over the course of 10 minutes for each trap separation.

Similarly, for the measurement of the potential of mean force between core-shell particles embedded in a sea of TPM particles, the core-shell particles are moved to a region where $\phi \approx 0.20$. The sample is left to equilibrate for a further 5 minutes before data is taken. Due to the presence of TPM host particles, the separation between the two optical traps were set between $3.2 - 7.0\mu$m so that any long ranged interactions between the core-shell particles can be recorded. Confocal 3D time-series of the sample are recorded using uni-directional scanning at 60 fps. The stacks have dimensions $50 \times 17 \times 20\mu m^3$, with resolutions of $0.195\mu$m /pixel in x-y and $0.25\mu$m /pixel in z. Typically 1000 stacks are recorded for each time-series, taking on average a total acquisition time of 22 minutes each. The raw timestamps and z-height of each confocal slice are also recorded for every run so that the time-resolution can be validated in the post-processing.

### 5.3.3 Image processing

The positions and trajectories of the small TPM host particles can be detected and tracked in 3D using the Crocker and Grier method (see Chapter 2 section 2.4.4). However the detection of the positions of the larger core-shell particles requires a different approach, because they are weakly fluorescent and appear much darker in the confocal images. Therefore the conventional particle detection method can lead to a large degree of inaccuracy in the particle position, and hence in the measured potential. To determine the equilibrium separation distance in the plane bisecting the centres of the pair of core-shell particles (and $\perp$ to $z$), we take a sum of the $x, y$ projections along $z$ over the region of the core-shell particle, and over the total time of the experiment (see Fig. 5.2A). From these projections, we can accurately determine the equilibrium positions of the trapped particles in $(x, y)$, by looking at the pixel intensities along $x$ and perpendicular $(y)$ to the axis of the trap separation in the summed image. The location of the core-shell particle corresponds to the low intensity regions of the plot profile (Fig. 5.2B), and a Gaussian curve is fitted to the bottom of each curve, yielding the $(x, y)$ coordinates of each particle. From these we obtain the average core-shell centre-to-centre separation distance for each optical trap separation.

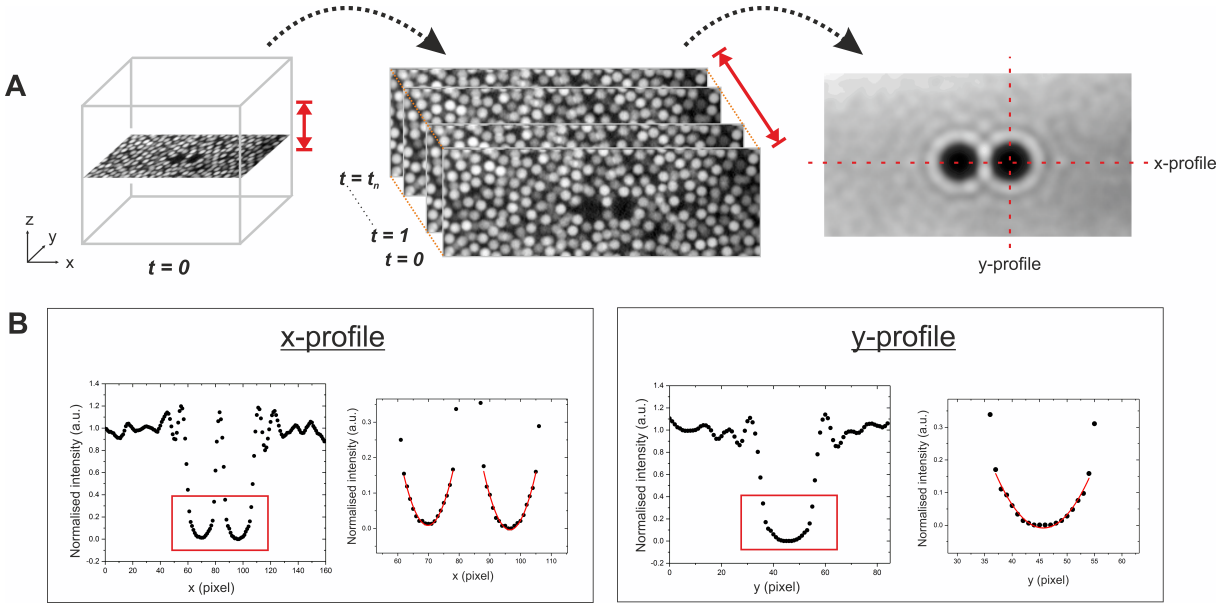


*Figure 5.2: (A) The relevant $x/y$ slices of each timestack is summed together to give a composite image containing information on the core-shell particle pair for that particular 'time frame', then all the composite images are summed together for the entire time series for a particular trap-separation, yielding the final image shown in the last panel. (B) Cross-section profiles of the normalised pixel intensity along the dotted lines on the composite image in $x$ and $y$. Gaussian functions were fitted to the low-pixel intensity regions to determine the particle coordinates.*

## 5.4 Results and discussion

### 5.4.1 Direct pair potential measurement

In Chapter 3 we have seen that the fluid-crystal phase transition for a system of refractive index matched TPM system occurs at $\phi = 0.42$, which is lower than what is expected for a hard-sphere system. This suggests a soft repulsive interaction between the TPM particles in the refractive index matching solvent. Here, we directly measure this interaction by tweezing two PS-TPM core-shell particles and bringing them to a close proximity. Due to the repulsive interaction, the pair of core-shell particles is expected be found (on average) further apart than the separation distance between the centres of the pair of optical traps. However because the range of this repulsive interaction is relatively short-ranged and decays as $\sim \exp(r)/r$, we do not expect to see significant deviation in the particle-particle separation $r_{LL}$ unless the trap-trap separation $r_{trap}$ is sufficiently small. As such, at large $r_{LL}$ the repulsive direct pair potential is very weak compared to the trapping potential and the core-shell particles diffuse around their respective trapping centres. However, as $r_{trap}$ decreases, the particles are brought increasingly close to one another and the repulsive force between them increases significantly, resulting in a measurable difference of $\Delta r = r_{LL} - r_{trap}$. Note that here, we assume that the potential of the PS-TPM core-shell particles are

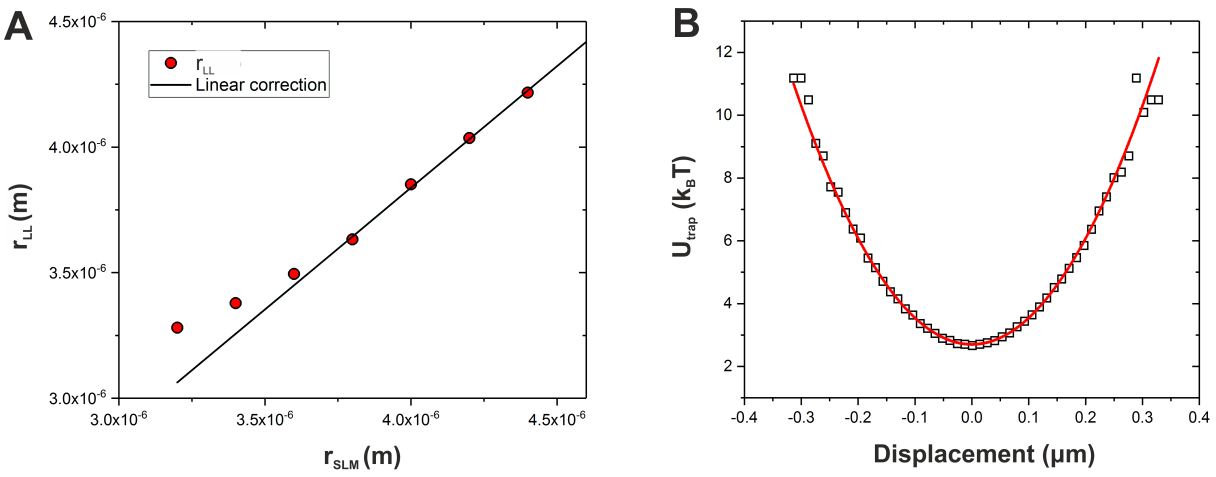


*Figure 5.3: (A) Detected core-shell particle centre-to-centre separation $r_{LL}$ compared with the estimated SLM trap-separation distance $r_{SLM}$ in a dilute core-shell particle dispersion. A linear correction has been added to account for the resolution of the SLM. (B) Typical optical trapping potential for a single PS-TPM core-shell particle in a TPM refractive index matching solvent, fitted with a parabolic curve of the form $\frac{1}{2}kx^2$. Data is taken from the pair potential measurement experiment for $r_{SLM} = 4.4\mu m$.*

identical to that of the TPM particles as their surfaces are identical.

Fig. 5.3A displays the outcome of trapping a pair of PS-TPM core-shell particles in a refractive index matching solvent and compares the SLM controlled trap centre-to-centre distance $r_{SLM}$ with the detected core-shell particle pair centre-to-centre separation $r_{LL}$. We see that for $r_{SLM} > 3.8\mu m$ there is good agreement between the particle separation and the trap separation, however at smaller $r_{SLM}$ there is a significance deviation in $r_{LL}$ from the linear trend. Before recording the difference $\Delta r$, we first account for the systematic error in the trap position calibration and the resolution of the SLM: using the large $r_{SLM}$ data points for reference, a line has been fitted and the y-intercept is restricted to $< 40nm$ to account for the resolution of the SLM ($r_{trap} = 0.96874 r_{SLM} - 3.7 \times 10^{-8}$). This line has also been plotted in Fig. 5.3A, and we can use the adjusted values of $r_{trap}$ to accurately determine $\Delta r$.

Next, to convert $\Delta r(r_{LL})$ into $F_{LL}$, we use $F_{opt} = -k \cdot \Delta r = -F_{LL}(r)$. To find the trapping stiffness $k$, we use the method described in Section 5.3. The natural logarithm of the probability distribution of core-shell's position in an optical trap is plotted against its displacement from the trap centre, as shown in Fig. 5.3B. To find $k$, the trapping potential close to the trap centre can modelled as a Hookian spring, and fitting with a function of the form $y = \frac{1}{2}kx^2$ yields a value for the trapping stiffness. The $k$ values for all trapping distances were found to be similar in magnitude, and an average value of $k = 7.42 \times 10^{-7} Nm^{-1}$ is taken for the subsequent calculations.

Having obtained both the $\Delta r$ and $k$, we can now determine the magnitude of the force due to the inter-particle interaction between the pair of core-shell particles using $F_{LL} = -F_{opt} = +k \cdot \Delta r$. This has

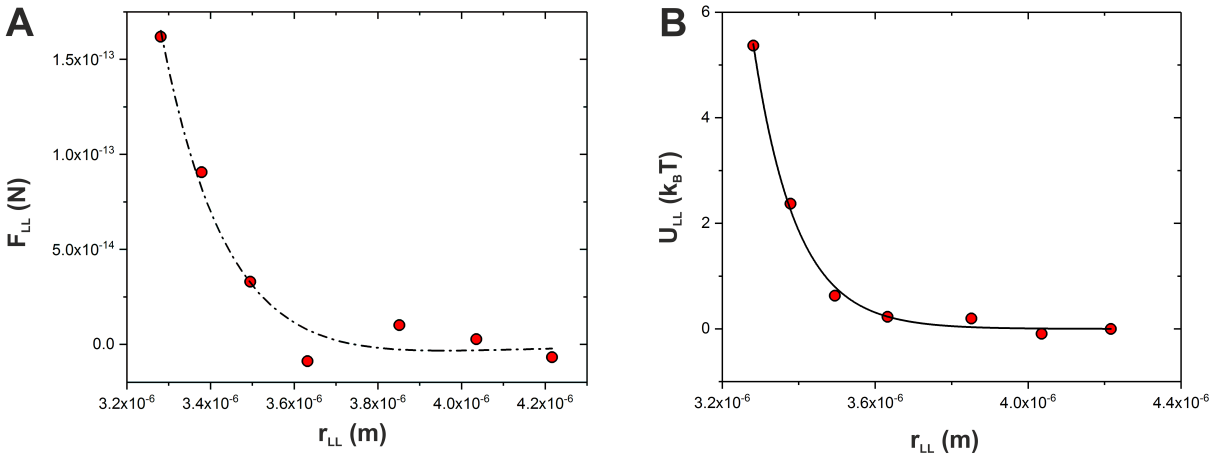


*Figure 5.4: (A) Force experienced by the pair of core-shell particles due to the presence of the optical tweezers, plotted as a function of their centre-to-centre separation distance. The force profile is fitted with the derivative of the Yukawa function. (B) Direct pair potential of the core-shell particle, fitted with the hard-sphere Yukawa function (Eqn. 5.1).*

been plotted in Fig. 5.4A as a function of the inter-particle centre-to-centre distance. As expected, the repulsive forces between the core-shell particles decreases rapidly to zero once $r_{LL}$ is sufficiently large. We have also fitted this plot with the derivative expression for the hard-sphere Yukawa model introduced in Eqn. 5.1, which has the form: $dU/dr = -AB\exp(-Br)/r + A\exp(-Br)/r^2$, where $A$ and $B$ are constants.

Finally, the direct pair potential between the two PS-TPM core-shell particles is obtained from $F_{LL}(r) = -dU_{LL}(r_{LL})/dr_{LL}$, i.e. by the integration of the inter-particle force data with respect to the inter-particle separation distance $r_{LL}$. This is shown in Fig. 5.4B along with a hard-sphere Yukawa fit, whose expression is given in Eqn. 5.1. By extrapolating the fit to $r_{LL} = \sigma_L$, where $\sigma_{LL} = 3.1\mu m$, we obtain a contact value of $\epsilon = 27.4k_BT$, as well as a value for the Debye length in the refractive index matching solvent of $\kappa^{-1} = 115nm$. For comparison, the $\kappa^{-1}$ value obtained from the exponential decay of the force curve in Fig. 5.4A yielded 140nm. Both would suggest a very low concentration of $\sim 2 \times 10^{-7}M$ for a monovalent salt in solution. Applying $\kappa$ and $\epsilon$ to the simulated phase diagrams of hard-sphere Yukawa systems as reported by Hynninen et al. [90], it predicts that the freezing transition of TPM particles in the refractive index matching solvent would occur at $\phi \approx 0.35$. This is somewhat below the freezing transition of $\phi = 0.42$ that we have determined previously in Chapter 3, but still confirms the soft nature of the particle interactions. In fact, the agreement is reasonably good as the exact values for $\kappa^{-1}$ and $\epsilon$ from the Yukawa fit are particularly sensitive to the particle diameter. For our calculations, we have used the SLS measurement of the core-shell particle that was measured in water. In addition, it also suggests that the TPM and the PS-TPM core-shell particles interact very similarly.

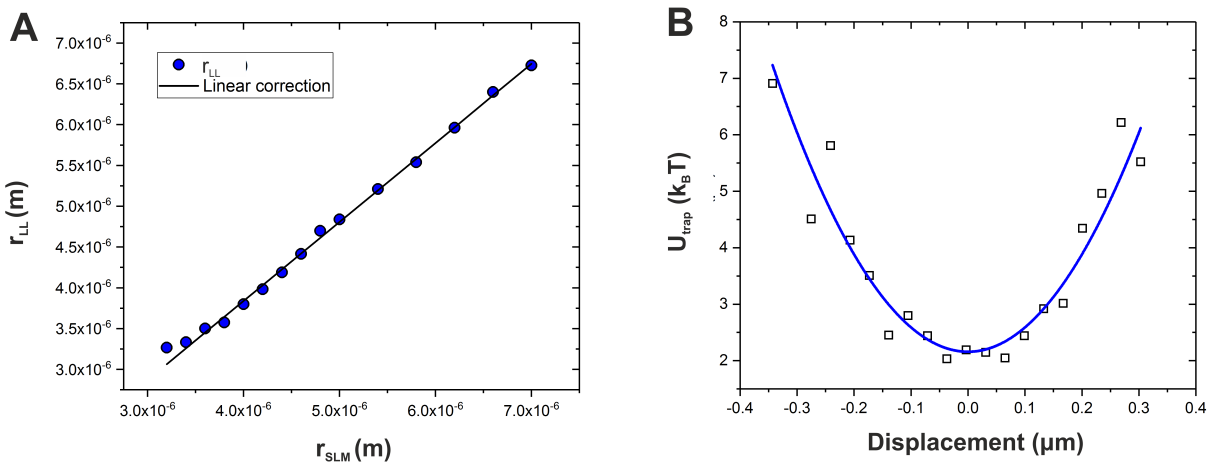


*Figure 5.5: (A) Detected core-shell particle centre-to-centre separation $r_{LL}$ compared with the estimated SLM trap-separation distance $r_{SLM}$ in a binary core-shell and TPM colloid mixture. (B) Typical optical trapping potential for a single PS-TPM core-shell particle in a TPM refractive index matching solvent with smaller TPM host particles around, fitted with a parabolic curve of the form $\frac{1}{2}kx^2$. Data is taken from the potential of mean force experiment for $r_{SLM} = 7.0\mu m$.*

### 5.4.2 Potential of mean force measurement

Analogous to the determination of the direct pair potential for a pair of isolated core-shell particles in the TPM refractive index matching solvent, the total effective potential between two core-shell particles embedded in a dense liquid of small TPM particles can be determined using the same methodology.

For the trapping of a pair of core-shell particles in a sea of small TPM spheres, whose average volume fraction is $\phi = 0.165$, the core-shell particle separation has been plotted against the SLM trapping distance in Fig. 5.5A. The packing fraction of the small TPM spheres varies up to 2% between each measurement, however it has been kept within a fluid region and below the freezing transition that was detected in Chapter 3. Comparing this with the equivalent plot for the direct pair potential (Fig. 5.3A), it appears that the deviation from the expected distance persist for a longer range of separation distances. Again the same linear correction used for Fig. 5.3A has also been applied to Fig. 5.5A, and from this we can work out the true trap-to-trap separation $r_{trap}$ and hence obtain $\Delta r$. Note that $\Delta r$ is now much smaller than those for the direct potential measurements. This indicates that the potential of mean force is much weaker.

The trapping stiffness for the potential of mean force experiment is obtained using the same method as the one for the direct pair potential experiment. Fig. 5.5B shows a typical example of the trapping potential and the parabolic fit. On average the trapping stiffness was found to be $k = 3.60 \times 10^{-7} Nm^{-1}$ for trapping a core-shell particle in the binary colloid mixture.

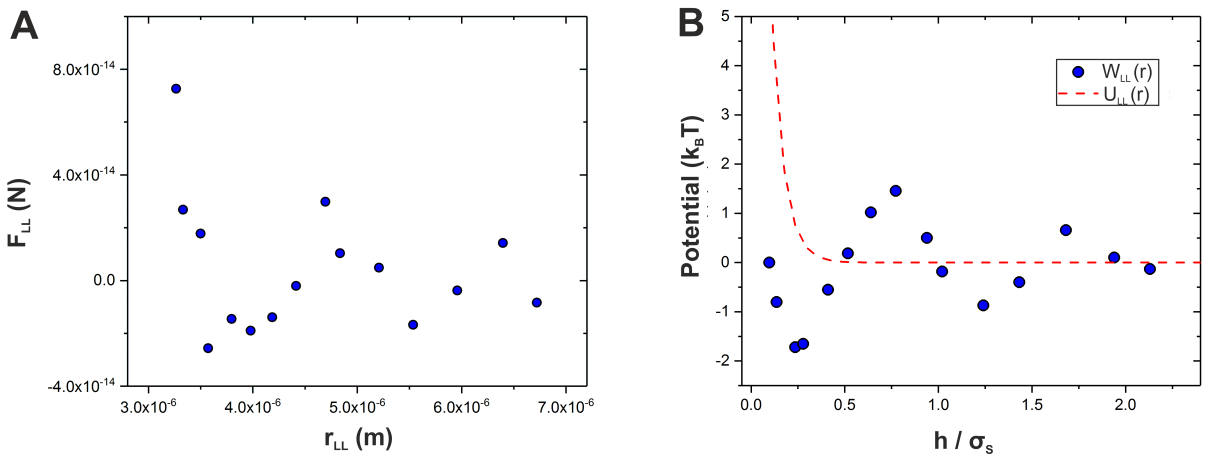


*Figure 5.6: (A) Force experienced by the pair of core-shell particles embedded in a sea of small TPM host particles, plotted as a function of the core-shell centre-to-centre separation distance. (B) Effective total pair potential or PMF of the core-shell particle in the binary mixture, plotted against the core-shell surface-to-surface distance normalised by the diameter of the small spheres. The extrapolated direct pair potential fit from Fig. 5.4B is also plotted (−−) for comparison.*

Using $F_{LL} = -F_{opt} = +k \cdot \Delta r$, the inter-particle force between the trapped core-shell particles is calculated and has been plotted as a function of the inter-particle separation in Fig. 5.6A. Unlike the force plot in Fig. 5.4A, we can see a highly oscillatory pattern in the force profile for the core-shell particle pair in the binary mixture, which persists for the entire range of separation distances that were measured. This contrasts with the faster decay in the force profile for the core-shell only system (Fig. 5.4). Also note that $F_{LL}$ here is about an order of manitude smaller than the equivalent core-shell only system.

Integrating the force profile, we get the potential of mean force for the trapping of the core-shell particles in the presence of small TPM host particles. From the plot of the potential of mean force in Fig. 5.6B, we also see the fluctuation in the potential around zero at various inter-particle separations. By plotting the potential against the surface-to-surface particle separation, normalised by the diameter of the small particles, it is interesting to observe that the potential appear most attractive at $h/\sigma_S = 0.25$ and 1.25, most repulsive at $h/\sigma_S = 0.75$ and 1.75, and zero at half or integer $\sigma_S$ spacings. Whereas for the direct potential measurement, also plotted in Fig. 5.6B, we can see that it decays rapidly to zero within a half of the small particle spacing. Therefore, in relation to the works by Crocker et al. [149, 150], and comparing with the Asakura-Oosawa prediction, the oscillation in the potential of mean force is attributed to the structure of the surrounding host particles.

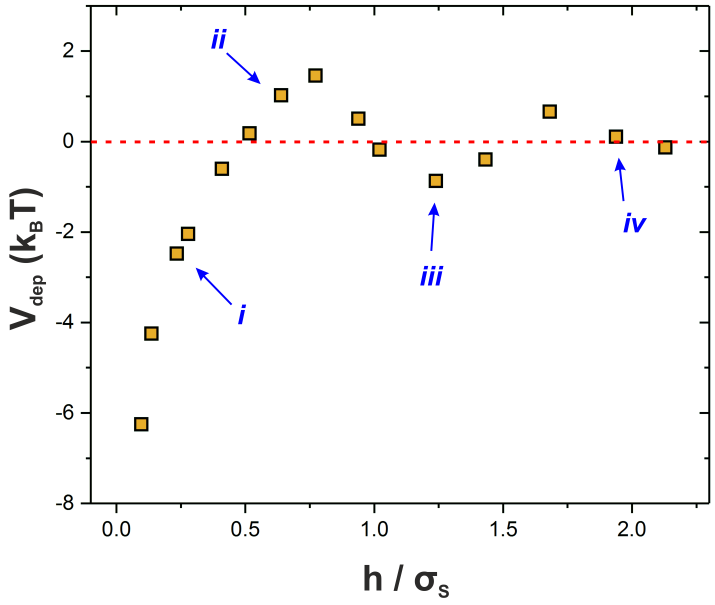


*Figure 5.7: Depletion potential of a pair of core-shell particles embedded in a sea of host particles with $\phi = 0.165$, plotted against the particle surface-to-surface distance h, normalised by the size of the small host spheres $\sigma_S$.*

### 5.4.3 Depletion potential

The direct pair potential and the full potential of mean force data, the depletion potential can be determined using $V_{dep} = W_{LL} - U_{LL}$ and this is shown in Fig. 5.7. The form of our depletion potential is consistent with the density-functional-theory simulation results reported by Roth et al. [150].

For $h/\sigma_S < 0.5$ the potential appears attractive. This has been predicted in the work of Asakura-Oosawa and can be explained by considering the large overlap of the zones around the trapped core-shell particles known as the excluded volume. This is a region where the smaller particles cannot penetrate. Effectively the overlap volume creates an osmotic pressure imbalance, where the pressure in the bulk greatly exceeds that in the excluded region. Consequently the two trapped particles experience an attractive potential. This attractive depletion potential is entropic in original. A greater overlap of the excluded volumes of the large particles results in an overall increase in space for the small particles. This leads to an overall increase in the entropy of the system, an therefore a lower free energy.

The attractive region at $h/\sigma_S = 1.25$ means that a small particle can now fit between the core-shell particle space. However as the spacing is greater than the integer value spacing of the small particle diameter, the time-averaged concentration of the small depletants is lower in the inter-particle region than in the bulk. Again this leads to an osmotic pressure imbalance, where the pressure in the bulk exceeds that of the inter-particle region. Therefore we see an attractive potential in Fig. 5.7.

Conversely, at $h/\sigma_S = 0.75$ and 1.75 where the particle separation is just below the integer spacings of the small host particles, the potential is repulsive. This suggests that the core-shell particles have a larger average separation distance than expected. As $h/\sigma_S$ is close to an integer values of the small particle spacing, there is a greater chance for the small particles to diffuse into this region, as driven by the pressure in the bulk. Therefore this leads to an increase in the average concentration of the small depletants in the inter-particle region, and the average osmotic pressure here is larger than the pressure in the bulk, hence 'wedging' the large particles apart. This repulsive potential persists until $h$ equals integer spacings of the small particle diameter, so that there is no net osmotic pressure imbalance in the system and the potential is zero.

### 5.4.4 Structure of the host particles

To illustrate the structural influence of the TPM host particles on the depletion potential, confocal data for the highlighted points in Fig. 5.7 are presented in Fig. 5.8. Here we can directly visualise the previously hypothesised 'liquid' structure layering of the small TPM host spheres around the pair of large core-shell particles at various trapping separations.

In the first column of Fig. 5.8, raw $(x, y)$ confocal slices for the four different core-shell separations are shown. These were taken from the middle of the z-stacks where the plane bisects the centres of both core-shell particles that were being held in the optical tweezers. Due to photobleaching, the core-shell particles appear dark in these images, whereas the RITC-labelled TPM host particles appear as the bright features. It is clear from Fig. 5.8(i) that there are no host particles in the inter-particle space at $h/\sigma_S = 0.24$, where the depletion potential is highly attractive. In (ii), $h/\sigma_S = 0.64$, small particles are seen to 'wedge' the large particles apart, resulting in a repulsive potential. In (iii), $h/\sigma_S = 0.64$, a single small particle can fit comfortably into the inter-particle region on average, but with a small excess volume. Lastly in (iv), $h/\sigma_S = 1.94$ so two small particles can reside in the inter-particle spacing.

To make it easier to see the overall averaged liquid structure of the small TPM particles, the confocal images were summed over the core-shell region of each stack and then for all frames in the 3D confocal time-series. These are displayed in the middle column of Fig. 5.8. Due to Brownian diffusion of the host particles, these now appear blurred in the images, but bright rings can be easily distinguished around the dark core-shell particles. Lastly, the normalised intensity profiles of the x-cross-section of the composite image are shown in the last column. This provides an indication of the probability of finding a host particle particle at specific points along the middle of the summed image.

| | Confocal slice | Summed image | Int. profile | h / $\sigma_s$ |
|---|---|---|---|---|
| *(i)* | 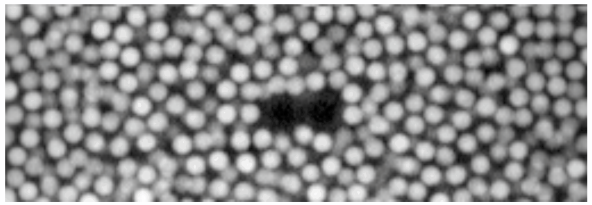 | 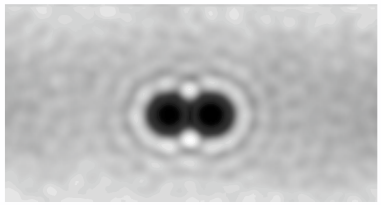 | 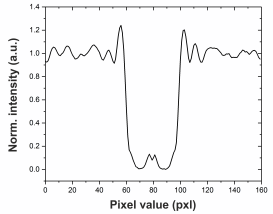  | *0.24* |
| *(ii)* | 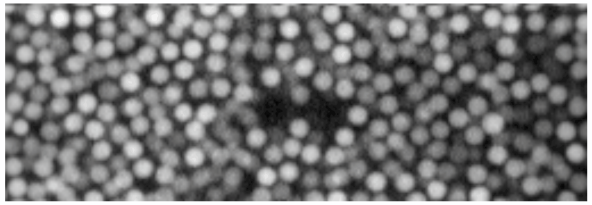 | 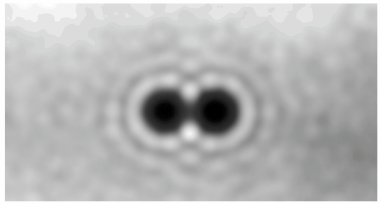 | 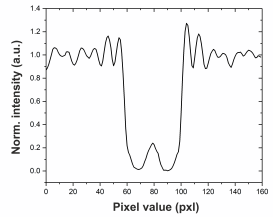  | *0.64* |
| *(iii)* | 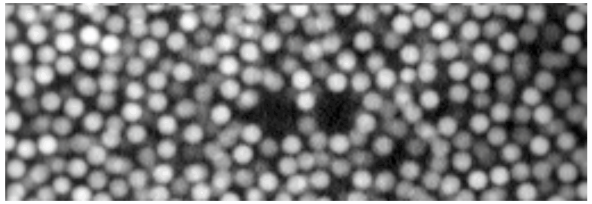 | 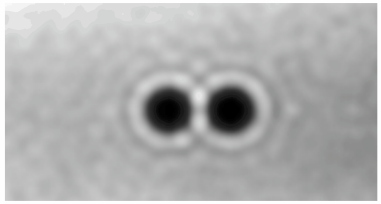 | 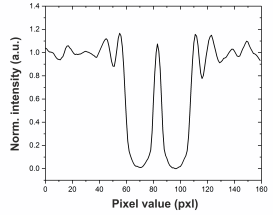  | *1.24* |
| *(iv)* | 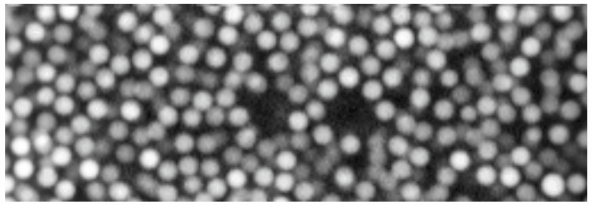 | 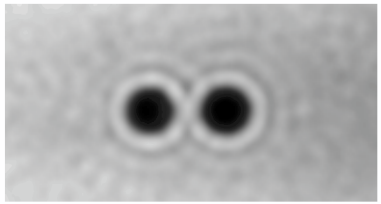 | 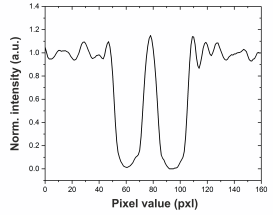  | *1.94* |

*Figure 5.8: Table of data for selected $h_{LL}$ as indicated in Fig. 5.7. For each distance of core-shell particle separation, a $(x, y)$ confocal slice bisecting the core-shell particle centre is shown, along with the composite confocal image and the pixel profile along $x$ as detailed in Section 5.3.3.*

For Fig. 5.8(i) with $h = 0.24\sigma_S$, the particles are experiencing a large attractive potential as seen in Fig. 5.7. The core-shell particles are very close to each other, and there are no small particles in the excluded region between them. In this liquid bath of TPM particles, the large particles have distinct layered structures of the small particles surrounding them [150]. They are pushed closer together to maximise the overlap of their depletion zones, so that more volume is available for the surrounding host particles. We also observe the extent of the overlap indirectly in the plot intensity cross-section, where the peak in between the core-shell particle pair is extremely low, signifying the low probability of finding any host particles in between them.

In (ii), the particles are slightly further apart, with $h = 0.64\sigma_S$, but the depletion potential here is near zero. Like in (i) the layering around the outside of the particles are observed. However there is also a higher probability of finding small particles immediately above and below the excluded zone. These small particles lead to a reduction in the overlap of the excluded volume of the large particle pair. As such there is a balance of the forces from these small particles in the $y$ direction, as well as that from that of the bulk in the $x$-direction. Consistently we see a reduction in the attractive strength of the potential at this particular separation distance. This is further confirmed by the increase in the pixel intensity of the middle peak in the plot profile.

As the particle separation $h$ increases further, more and more small particles can fit in the spacing between the pair of large particles. In Fig. 5.8(iii), $h/\sigma_S = 1.24$, the spacing is larger than the small TPM particle diameter and is sufficiently large for one small particle to fit on average. This is reflected in the middle peak of the normalised intensity profile. We also see the complete 'ring' of small host particles around the two core-shell particles in the summed confocal images. For Fig. 5.8(iv), $h/\sigma_S = 1.94$, the spacing is almost large enough for two TPM host particles to fit in line between the core-shell probes, and two separate 'rings' can be seen around the large particles. As $h$ is now near an integer value of small particle spacing, there is very little osmotic pressure imbalance, and the depletion potential is nearly zero (see Fig. 5.7).

Next, we quantify the structure of the small particles by calculating the radial distribution function of the small host particles, $g_{SS}(r)$. The packing fraction of the core-shell particles is so low in the system that their contribution to $g_{SS}(r)$ is negligible. The measured $g_{SS}(r)$ is plotted in Fig. 5.9A, and the peaks occur near integer values of $\sigma_S$. To find a comparable radial distribution function for the large core-shell particles, $g_{LL}(r)$, we can use the potential of mean force $W_{LL}$ according to:

$$g_{LL}(r) = \exp\left(-\frac{W_{LL}(r)}{k_B T}\right). \tag{5.8}$$

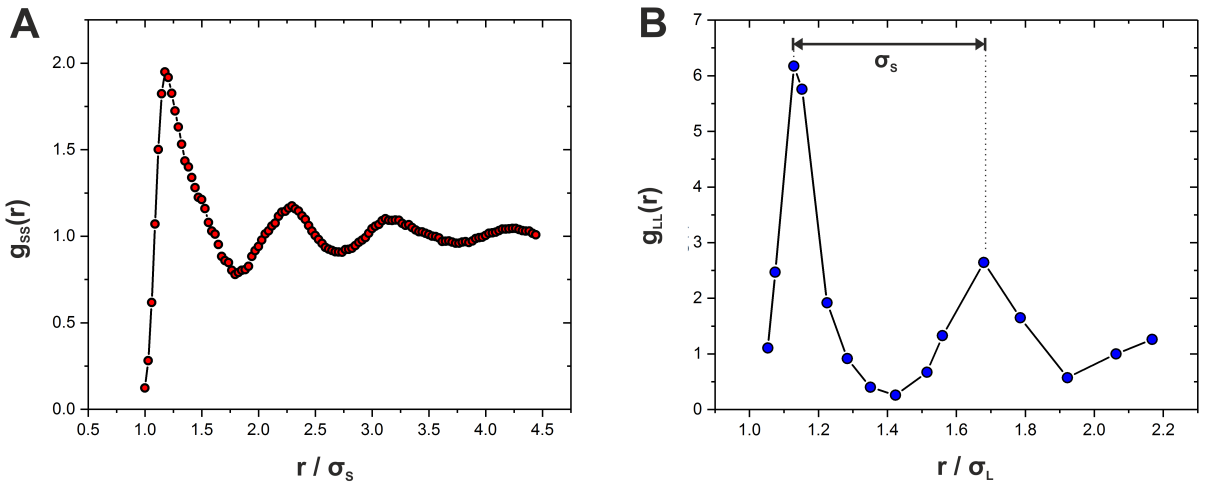


*Figure 5.9: Radial distribution functions from the binary system for (A) the small TPM host particles ($\phi_{TPM}$ = 0.165), and (B) the large core-shell probe particles ($\phi_{CS}$ = 0.0018), as derived from the potential of mean force data (Eqn. 5.7). A linear extrapolation of $g_{LL}(r)$ is also included here for illustrative purposes (–). $\sigma_S$ and $\sigma_L$ denotes the TPM and core-shell particle diameters respectively.*

The resulting $g_{LL}(r)$ is plotted in Fig. 5.9B against a radial distance normalised by the size of the large particle diameter $\sigma_L$. Interestingly, the peak separation does not correspond to integer values of $\sigma_L$, but rather corresponds to integer values of $\sigma_S$. Therefore this indicates that the $g_{LL}(r)$ in our binary mixture is completely dominated by the structure of the small particles.

This can be further quantified by plotting the natural logarithm of the total correlation function $h(r) = g(r) - 1$, as a function of distance normalised by the small spheres, which highlights the oscillation wavelength in the decay of the structural peaks of $g(r)$ [156]. In Fig. 5.10A, this is done for $g_{SS}(r)$ and it is clear that the peaks have integer value spacing of the small particle diameter. Similarly for $g_{LL}(r)$ via Eqn. 5.7 (see FIg. 5.9B), we see that the peaks also oscillate at integer values of $\sigma_S$. This confirms that in the limit of $\phi_L \to 0$, the depletion interaction between the two large particles is dominated by the structuring of the small particles.

## 5.5 Conclusions and outlook

In summary, we measured the depletion potential of two large PS-TPM core-shell particles embedded in a sea of small TPM particles using optical tweezing, and recorded the 3D structuring of the host particles using confocal microscopy. The direct pair potential of a pair of isolated core-shell particles was detected first, before a sea small TPM particles was introduced so that the potential of mean force between two large particles can be measured. The depletion potential is then obtained by subtracting the direct interaction

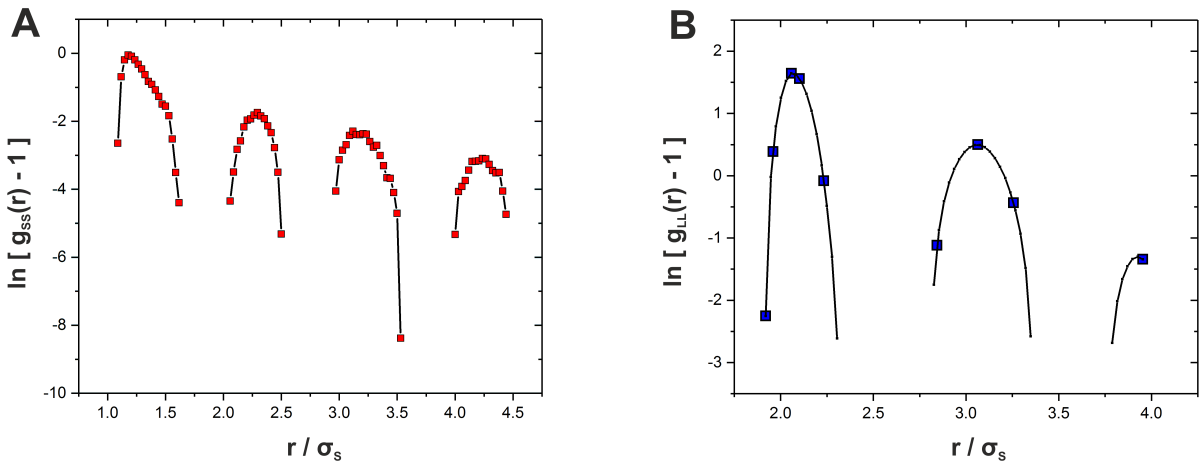


*Figure 5.10: The natural logarithm of the total correlation function for the small TPM particles (A) and the large core-shell particles (B), plotted as a function of distance away from the particle centre r and normalised by the size of the small particle diameter $\sigma_S$.*

potential from the total interaction potential. Finally we discussed the form of the depletion potential in terms of the structuring of the small host particles around the large core-shell particles.

With this experiment, we have also demonstrated the suitability of our colloidal system for combined 3D confocal microscopy and optical tweezing studies, which may help to better address some of the fundamental questions in statistic mechanics. In future work, we will extend the depletion potential measurements to other volume fractions of the small host particles so as to obtain a more complete picture of the depletion potential. Likewise it may also be interesting to explore the effect of size ratio of the binary colloid mixture on the depletion interaction.

## Acknowledgements

This work is down in collaboration with Arran Curran, Taiki Yanagishima and Dirk Aarts.

# Chapter 6

# Development of optically anisotropic dumbbells

ABSTRACT

In this chapter, we synthesise and characterise optically anisotropic dumbbell particles by coating a high refractive index seed particle with a single TPM lobe. We rationalise the formation of the dumbbell particles by considering the total surface energy for single and multi-lobed particles. In particular, we investigate the effects of the hTPM volume, the seed particle size, and the lobe's contact angle on the total surface energy. We discuss the synthesis outcomes from Chapter 4 in light of these calculations, as well as the results of coating titania-PS and TPM seed particles with TPM. Finally we demonstrate the use of MF-TPM dumbbells immersed in a solvent with a refractive index in between that of the dumbbell lobes in a preliminary optical tweezing experiment, where we drive the TPM lobe with a time-delayed feedback trapping setup.

## 6.1 Introduction

In recent years, optical tweezing and manipulation of colloidal particles have become a widely used tool to study a wide range of topics in soft matter [54], ranging from hydrodynamic coupling [157] to directed self-assembly [158]. With the increasing complexity in the design and development of trapping methods and technology, particularly the use of spatial-light-modulators (SLM) [54], we are able to access a large variety of optical landscapes, including the simple Gaussian beam [101, 159], Laguerre-Gaussian beams [160, 161], and interference patterns [162]. This opens up a wide range of topics that can be addressed using trapped and driven spherical colloids in various optical potentials [160].

The complexity of optical tweezing experiments can also be increased by trapping colloidal particles with complex geometries and anisotropic properties [37]. The simplest anisotropic geometry for a non-spherical particle would be the prolate or the oblate, i.e. a rod-like particle or a disk-like particle. Indeed, the optical manipulation of homogeneous rods has also been reported [160]. Nevertheless, the behaviour of optically anisotropic colloidal particles in optical traps is much less explored. If we have two spheres made from different materials conjoined in the form of a dumbbell particle, it would be possible to induce both geometric and optical anisotropy.

We have seen in Chapter 3 that TPM droplets can often attach to the surface of a spherical seed particle during nucleation, and that the volume of the TPM used can greatly influence the final geometry of the colloidal particle. This varies from the multi-lobed raspberry particles to single-lobed particles [37, 163]. By the nature of the coating, different materials for the seed can be used, resulting in two sides of the dumbbell particle having different refractive indices. If the size of the TPM lobe of the dumbbell particle can be controlled so that the size ratio between the two lobes is approximately 1:1, then we effectively have a prolate particle with optical anisotropy. To better control the morphology of the dumbbell particle during synthesis, the total surface energy involved needs to be considered to see which geometries (multi-lobed or single-lobed) are more favourable under different conditions. In particular, one has to consider the amount of TPM used, the size of the initial seed particle, and the change in the contact angle through the introduction of surfactants.

In this chapter, we will first explore the underlying reasons for the formation of multi-lobed or single-lobed particles by considering the surface energies in these systems. We will compare these numerical calculations to our experimental observations, involving the coating of different seed particles with TPM under different reaction conditions, and also discuss the limitations of the surface energy

calculations. Lastly, we immerse the optically anisotropic MF-TPM dumbbell particle in a solvent medium with intermediate refractive index to the two sides of the dumbbell, and manipulate it using optical tweezers. In this preliminary tweezing experiment, we trap one side of the dumbbell and drive the other side using a second trap, following a time-delayed feedback control.

## 6.2 Background

### 6.2.1 Surface energy of a droplet

For a droplet of any material to exist in a dispersion medium of a different material, there is a surface tension $\gamma$ associated with the interface. This surface energy originates from the net loss of bulk intermolecular forces at the interface, and can be considered as the work required to create the interface when bringing the two materials into contact [80, 81]. The surface tension between materials 1 and 2, $\gamma_{12}$, is expressed by the Dupré equation [81] as:

$$\gamma_{12} = \frac{1}{2}W_{11} + \frac{1}{2}W_{22} - W_{12} = \gamma_1 + \gamma_2 - W_{12}, \tag{6.1}$$

where $W_{12}$ is the contact energy between materials 1 and 2. As such, this implies that the nucleation and the formation of droplets of liquid 1 in liquid 2 would only occur if there is a sufficiently large surface tension between the two fluids.

For a single lobe of material 2 on a flat surface of material 1 in a medium 3 (Fig. 6.1A), its shape depends on the surface energies. At equilibrium, there is a contact angle $\theta$ that is defined by the balance of the interfacial tensions at the triple contact point. This leads to the Young's equation [81]:

$$\gamma_{12} + \gamma_{23}\ \cos(\theta) = \gamma_{13}. \tag{6.2}$$

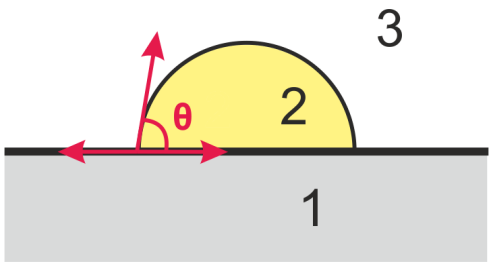


*Figure 6.1: Schematic diagrams of: (a) A droplet on a flat surface, and (b) A droplet on a spherical surface. Numbers 1, 2, 3 denote the solid phase, the TPM droplet phase, and the aqueous phase respectively. $\theta$ is the contact angle between the droplet and the solid surface.*

Physically, the contact angle $\theta$ has to lie between 0° and 180°, which corresponds to complete wetting and complete de-wetting respectively.

Surface tension has the unit of energy per area. Therefore, to work out the total interfacial energy, we also need to consider the relevant surface areas of contact between the three phases. For the system depicted in Fig. 6.1A, the total surface energy can be described as:

$$U = \gamma_{13}A_{13} + \gamma_{12}A_{12} + \gamma_{23}A_{23}. \tag{6.3}$$

Since the contact angle is independent of the geometry of the surface, the above equation can be adapted to the case where the substrate surface is highly curved, e.g. the case shown in Fig. 6.4A. As such, the surface energies of the single-lobed and multi-lobed particle formation can be calculated and compared, which will be discussed in Section 6.4.1.

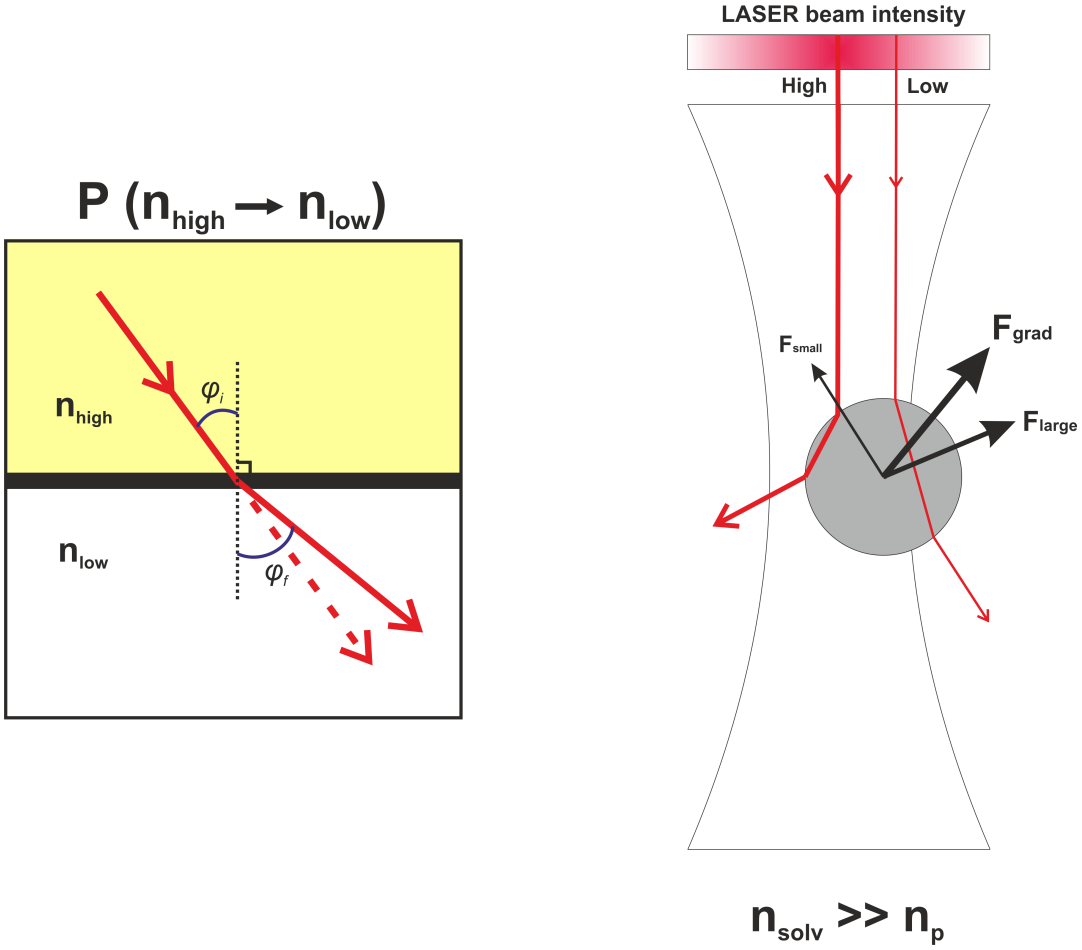


*Figure 6.2: Schematic diagrams illustrating: the refraction of light when travelling from a high refractive index material to a low refractive index material, and the gradient forces involved when trapping a particle with a lower $n_f$ than that of the solvent medium. (c.f. Fig. 2.7 for trapping a particle with $\Delta n_f > 0$.)*

### 6.2.2 Optical trapping of optically Janus dumbbells

In the previous chapters, the optical tweezing experiments made use of the positive refractive index mismatch ($\Delta n > 0$) between the colloidal particle and the surrounding medium. The underlying mechanism was detailed in Chapter 2, Section 2.4.3, which involves the balancing of the scattering forces and the restoring gradient forces on the particle. However, if light is travelling from a high refractive index material to a low refractive index material, as shown in Fig. 6.2, it would speed up at the interface and its path would deviate away from the normal. Therefore if a colloidal particle has a lower refractive index than its surrounding medium, when placed close to an optical tweezer, the laser beam that travels through the solvent-particle interface would refract away from the normal of the incident light. Thus the resultant gradient force points away from the focal point of the trap, and helps to destabilise the particle in the trap centre. As such, the particle would experience a potential 'hill' at the center of the optical trap, and any fluctuations away from the exact trap centre would lead to a repulsive force that pushes the particle down the trapping potential.

## 6.3 Experimental methods

Three main types of seed particles have been used for the investigation of TPM droplet formation on the curved surfaces: melamine formaldehyde (MF) particles, titania coated polystyrene particles, and fully cross-linked TPM particles.

### 6.3.1 MF-TPM dumbbell synthesis

Melamine formaldehyde particles were synthesized as described in Chapter 4 [141]. In a typical reaction, the MF seeds were converted into MF-TPM dumbbell particles by the following method. In a 30 ml bottle, $20\mu l$ of $NH_4OH$ (28% $NH_3$ in water) is added to a 20 ml aqueous solution that contains $\approx 10^6/ml$ seed particles. 5 ml of hydrolysed TPM solution (1:10 v/v TPM to water) is injected into the reaction whilst stirring at 500rpm using a magnetic plate. The reaction is left to run for 40 mins, then 200 $\mu$l of F108 is added and allowed to react for a further 5 mins. A fluorescent dye may be added at this point for labelling the TPM parts of the particle. Finally, 50 mg of AIBN is added, and the reaction mixture is heated in the oven at 80°C for 5 hours. The particles are left to cool overnight and are cleaned using repeated sedimentation and decanting using deionised water.

### 6.3.2 Titania-TPM dumbell synthesis

The titania seed particles were made using the methods reported by Imhof [164]. Titania-TPM particles were synthesised using a similar method to Section 6.3.1, but with the quantities adjusted to account for the small seed size. To convert the titania particles into dumbbells, 2 ml of hTPM (1:30 v/vol TPM to water) is added to a 28 ml alkaline solution ($\sim pH10$ containing $\sim 10^8 particles/ml$ of the seed particles and 30$\mu$l of $NH_3$. The reaction is stirred at moderate speed using magnetic stirring plate and is left to react for 40 mins. Finally AIBN is added and the reaction mixture is heated to 80°C for the cross-linking of TPM polymers.

### 6.3.3 TPM-TPM particle synthesis with PVP

The TPM seed particles were prepared using the methods described in Chapter 3. Batch *yl-01-12B* (see Table 3.2) was chosen for the contact angle experiment, as the particles do not have any surfactant on the surface. To test the effect of surfactants on the formation of TPM lobes on seed particles, three different polyvinylpyrollidone (PVP) sizes with average molecular weights of 10k, 40k, and 360k $g/mol$ were used. To coat the seed particle surface with PVP, an excess amount of PVP was first dissolved in 5ml of $H_2O$ before adding 5ml of seed particles. The mixture is left to mix thoroughly for 2 days. Next, the seed particles are extracted by centrifugation, and excess PVP is washed off with deionised water. The seeds are then coated with TPM using the same method as that for the titania-TPM synthesis described in the previous paragraph. A control experiment was also carried out using the untreated TPM seed particles.

### 6.3.4 Optical tweezing of MF-TPM dumbbell particles

The two parts of a MF-TPM dumbbell particle have a refractive index of 1.68 and 1.52 respectively. Tetralin has a refractive index of 1.54, in between that of MF and TPM, and is therefore a suitable solvent for exploring the unusual trapping behaviour of the optically anisotropic dumbbell particle. The MF-TPM dumbbell particles are transferred to a pure tetralin solution containing 1% wt OLOA 1200 via the step-wise solvent transfer process described in Chapter 3. For the tweezing experiments, the dispersion was highly diluted so as to prevent multiple particles from jumping into the trapping beam during the experiment.

As seen from the schematic diagrams in Fig. 6.3, two individual first-order traps, generated using SLM, are used for the optical tweezing experiment. The first one is used to trap the MF part ($\Delta n > 0$)

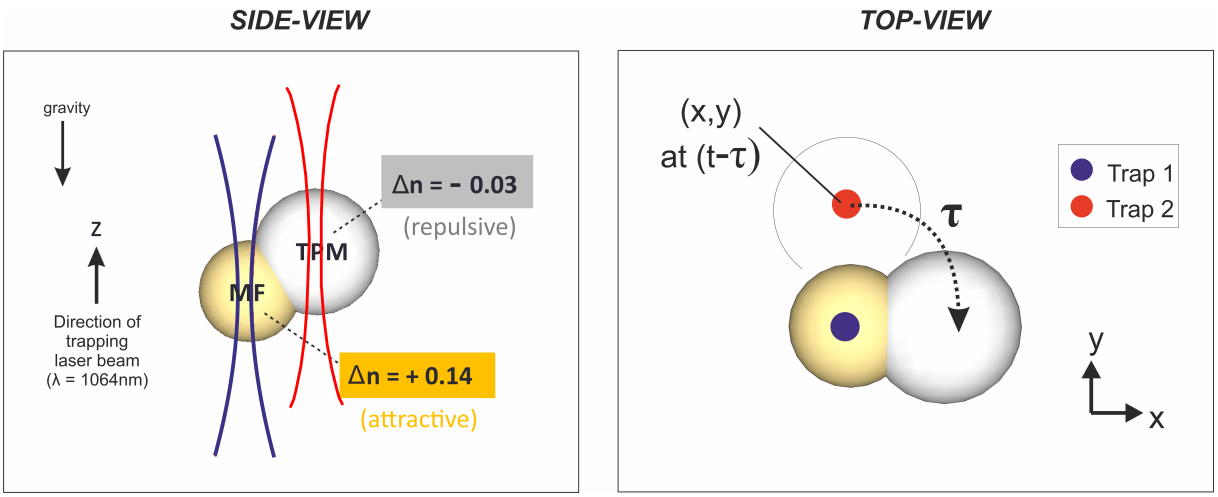


*Figure 6.3: Schematic diagram of a driven dumbbell experiment using two optical tweezers. One trap is used to center the MF part of the dumbbell, which has a +ve $\Delta n$ to the surrounding, the other trap is used to 'drive' the TPM lobe, which has a -ve $\Delta n$ to the surrounding. The position of the first trap is fixed, whereas the second trap is moved to the coordinates of the TPM lobe at $\tau$ seconds ago.*

of the dumbbell particle, and the second trap is placed $\sim 5\mu m$ away from the first trap, and is used as the 'driving' trap for the TPM lobe ($\Delta n < 0$). Both traps are set at the same trapping power. During the experiment, the location of the first trap is fixed, and the 2D position of the TPM lobe that points away from the first trap is located and recorded with center-of-mass tracking in real-time . The second trap is used to retrace the trajectory of the TPM lobe with a fixed time-delay $\tau$ (See Top-view of Fig. 6.3). The experiments are recorded as 2D brightfield videos from the topview, with the MF part of the dumbbell out of focus and the TPM lobe in focus. Care was taken to ensure that at the start of each experiment, the second trap is placed $> 10\mu m$ from the first trap so as to avoid influencing the initial movements of the TPM lobe.

## 6.4 Results and discussion

In this section, first the analysis of the total surface energy of a single-lobed and a multi-lobed particles will be discussed. These will be compared to the surface energies of isolated TPM droplets formed in solution, i.e. not on the surface of the seed particles. Next, we discuss the observed particle geometries in light of these calculations, particularly the effects of changing the volume of TPM and the contact angle (via surfactants). Finally, the dynamics of a trapped MF-TPM dumbbell particles in an preliminary optical tweezing experiment will be shown and discussed.

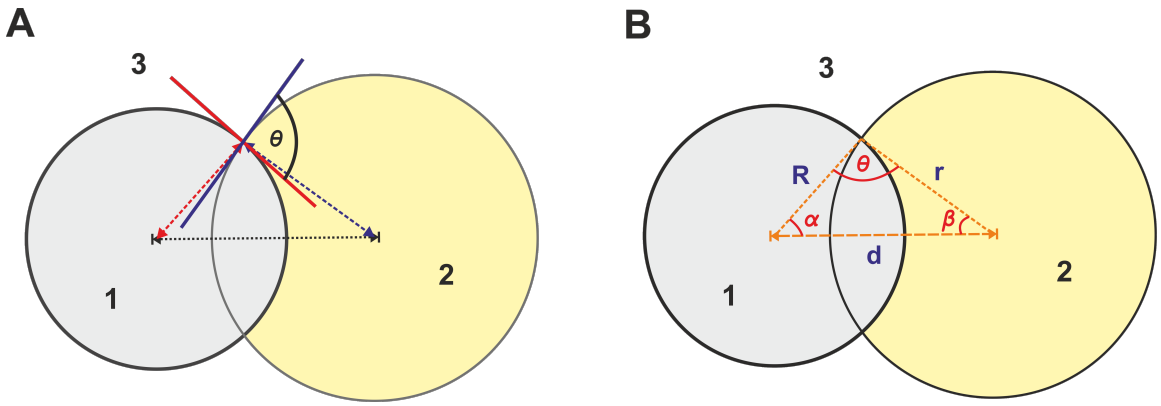


*Figure 6.4: (a) The contact angle θ for a lobe on a curved surface (b) Triangular relationship between θ and the radius of phase 1, R, radius of phase 2, r, and the centre-to-centre distance of separation, d. The letters α and β denotes the angles between the centre-to-centre line to the centre-to-intersection point from phase 1 and phase 2 respectively.*

### 6.4.1 Surface energy

To investigate the preferential formation of multi or single lobes on a seed particle during the coating with TPM, we need to consider the total surface energy. For a given total volume of TPM, $V_{total}$, the volume of each lobe (or droplet) $V_d$ formed on the seed particle is given by

$$V_d = \frac{V_{total}}{N}, \tag{6.4}$$

where $N$ is the number of droplets formed. In the case of a lobe on a flat surface as shown in Fig. 6.1, the total surface energy is given by Eqn. 6.3. This equation can be adapted to the spherical surface shown in Fig. 6.4A, and because $A_{13} + A_{12} = 4\pi R^2$, the total surface energy can be rewritten as:

$$U_d = \gamma_{13}(4\pi R^2 - A_{12}) + \gamma_{12}A_{12} + \gamma_{23}A_{23}. \tag{6.5}$$

Using Young's relation (Eqn. 6.2) for $\gamma_{13}$, this becomes:

$$U_d = \gamma_{13}4\pi R^2 + \gamma_{23}(A_{23} - A_{12}\cos\theta). \tag{6.6}$$

The first part of this expression is the surface energy from the seed sphere, and the second part comes from the contribution of the attached TPM lobe. Therefore, in the case of $N$ droplets attached to the seed sphere's surface, the contribution of the second part of Eqn. 6.6 would be $N$ times greater, giving a total

surface energy of:

$$U_d(N) = \gamma_{13} 4\pi R^2 + N\ \gamma_{23}(A_{23} - A_{12}\cos\theta). \tag{6.7}$$

As a reference, the total surface energy of $N$ free liquid TPM droplets and the free seed particles in the dispersed medium is simply

$$U_f(N) = \gamma_{13} 4\pi R^2 + N\ \gamma_{23} A_{23} = \gamma_{13} 4\pi R^2 + N\ \gamma_{23} 4\pi r_f^2. \tag{6.8}$$

Here $r_f$ is the radius of the free TPM droplet in solution. Comparing Eqn. 6.7 and 6.8 for the attached lobes and free droplets scenario, we can see the two differ by $(N\gamma_{12}A_{12}\cos\theta)$. Consistently, in the case of complete dewetting with $\theta = 180°$, Eqn. 6.7 is reduced to Eqn. 6.8.

For a given $V_{total}$ of TPM, it is straighforward to calculate $U_f$ for all $N$, as $r_f \propto V_d^{1/3}$. However, this is not the case for $U_d$. In order to find $U_d$ using Eqn. 6.7, we must first determine $A_{12}$ and $A_{23}$ for a given $V_d$. From the diagram in Fig. 6.4, we can see that the edges of the overlap region of phase 1 and 2 consist of the spherical caps of spheres 1 and 2 respectively. Using standard trigonometric relations applied to Fig. 6.4B and the equation for the surface area of a spherical cap $S = 2\pi Rh$ where $h$ is the height of the cap, we obtain an expression for $A_{12}$:

$$A_{12} = 2\pi R^2(1 - \cos(\alpha)). \tag{6.9}$$

Similarly, the expression for $A_{23}$ is

$$A_{23} = 4\pi r^2 - 2\pi r^2(1 - \cos(\beta)). \tag{6.10}$$

We can rewrite this in terms of $R$, $\alpha$ and $\theta$ using the sine rule, knowing that $\alpha + \beta + \theta = 180°$:

$$A_{23} = 2\pi R^2 \sin^2(\alpha)\Big(\frac{1 - \cos(\alpha + \theta)}{\sin^2(\alpha + \theta)}\Big). \tag{6.11}$$

Substituting both Eqn. 6.9 and 6.11 back into the equation for the total surface energy (Eqn. 6.7), we now have $U_d$ expressed as a function of $\alpha, \theta$ and $R$.

$$U_d = U_d(N, R, \alpha, \theta) = \gamma_{13} 4\pi R^2 + N\gamma_{23}\pi R^2\Big(\frac{sin^2(\alpha)}{cos^2(\frac{\theta+\alpha}{2})} - 2\ cos(\theta)\Big(1 - cos(\alpha)\Big)\Big). \tag{6.12}$$

This means that for a given seed particle size of $R$, and a fixed contact angle $\theta$, the total surface energy

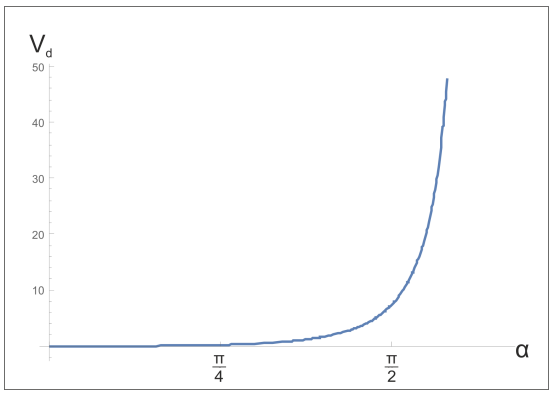


*Figure 6.5: An example of $V_d$ as a function of $\alpha$, where $\theta = \frac{\pi}{3}$, plotted for the physically valid range of $\alpha$ ($0 \leq alpha < \theta$). Note that $V_d$ shown here had been normalised by the volume of the seed particle and is a dimensionless quantity.*

is a function of $N$ and $\alpha$. Note that the sum of all $A_{12}$ has to be smaller than the total surface area of the seed particle. i.e.

$$\sum_{i=1}^{N} A_{12} = NA_{12} < 4\pi R^2, \tag{6.13}$$

which assumes that the maximum close packing of the droplets on the seed particle surface is unity, compared with the value of 0.91 for close packing in 2D.

The parameter $\alpha$ is a measure for the volume of the droplet $V_d$, as there is a one-to-one relationship between $V_d$ and $\alpha$ (see Appendix for a full derivation of $V_d$). Mathematically, $V_d$ is cyclic and periodically reaches asymptotic points at $\alpha = (\pi - \theta) + 2n\pi$. An example of $V_d$ is plotted in Fig. 6.5 for an arbitrary contact angle $\theta = \pi/3$ for its physically valid region, $0 \leq \alpha < (\pi - \theta)$. This is because for $(\pi - \theta) < \alpha < 2\pi$ the volume $V_d$ is negative and non-physical, thus this is consistent with the boundary condition stated earlier regarding the contact angle, $0 \leq \theta < \pi$. This one-to-one relation between $V_d$ and $\alpha$ for a given $\theta$ establishes the link between $V_d$ and $A_{12}$ and $A_{23}$ (Eqns. 6.9 and 6.11), which are also parametrised by $\alpha$. Hence for a given $V_{total}$ and $N$, we find $\alpha$, which can then be used in Eqn. 6.12 to find the total surface energy.

Because $V_d$ depends on $N$ and the total volume of TPM in the system (Eqn. 6.4), and is parametrized by $\alpha$, the total surface energy can be considered as $U_d = U_d(V_{total}, N, R, \theta)$. In the following section, we will investigate the effect of changing the total TPM volume, the seed particle size, and the contact angle on the overall surface energy of the system as a function of $N$. In the subsequent calculations, $\gamma_{13}$, which corresponds to $\gamma_{PS/H_2O}$, has been set to 34 mN/m as per [165]. The value for $\gamma_{23}$, which corresponds to the interfacial tension between partially cross-linked TPM and water is not reported. Therefore the

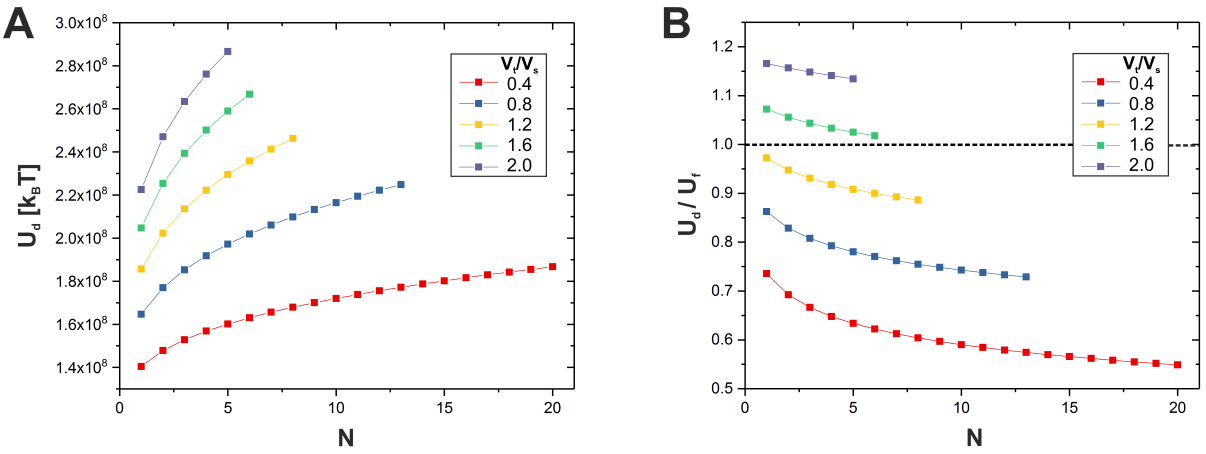


*Figure 6.6: (A) Total surface energy of attached droplets against number of droplets for different total TPM volumes of $V_t$, given in the legend as a ratio w.r.t. the seed particle volume, $V_s$. (B) The calculated $U_d$ values for the attached droplet state shown in (A) but is now normalised with the corresponding free droplet state, $U_f$.*

value for propyltrimethoxysilane and water ($\gamma_{PTMS/H_2O}$ = 28.5 mN/m) is used instead as an estimation, as PTMS has a similar chemical structure to TPM.

### 6.4.2 Effect of total TPM volume on surface energy

As $U_d = U_d(V_{total}, N, R, \theta)$, the values for $R$ and $\theta$ have been fixed to 1$\mu$m and $\frac{\pi}{3}$ respectively. The total surface energy as a function of the number of droplets on the seed surface is given in Fig. 6.6A for five different total volumes of TPM. This highlights the relative changes in the total surface energy as $N$ increases for different volumes of TPM. As the total TPM volume increases, the total surface energy becomes larger for all $N$, and the number of $N$ that is physically possible has decreased significantly (due to the surface area constraint, Eqn. 6.3). For all total TPM volumes, the lowest surface energy state always lies at $N = 1$. This indicates that the most stable state is the single-lobed dumbbell system. The formation of the multi-lobed raspberry particles ($N > 1$, Chapter 4) can thus be attributed to kinetics. In other words, the coalescence of the lobes on the seed's surface is kinetically very slow, possibly due to their charged nature in water. Furthermore, from Fig. 6.6A, it is clear that as $V_{total}$ gets larger, it is energetically more costly to create multiple lobes on the seed particle surface. Thus, we are more likely to observe raspberry particles at low TPM volumes and less likely to do so at large $V_{total}$, consistent with our observations in Chapter 4 (See Fig. 4.8).

Comparing the attached droplet system to the free droplet reference state (Eqn. 6.8) in Fig. 6.6B, the ratio of $U_d/U_f$ provides a reference to the extent of stablisation that can be gained by attaching droplets to the seed particles. As $V_{total}$ increases, $U_d/U_f$ is raised for all $N$. For the curves that satisfy

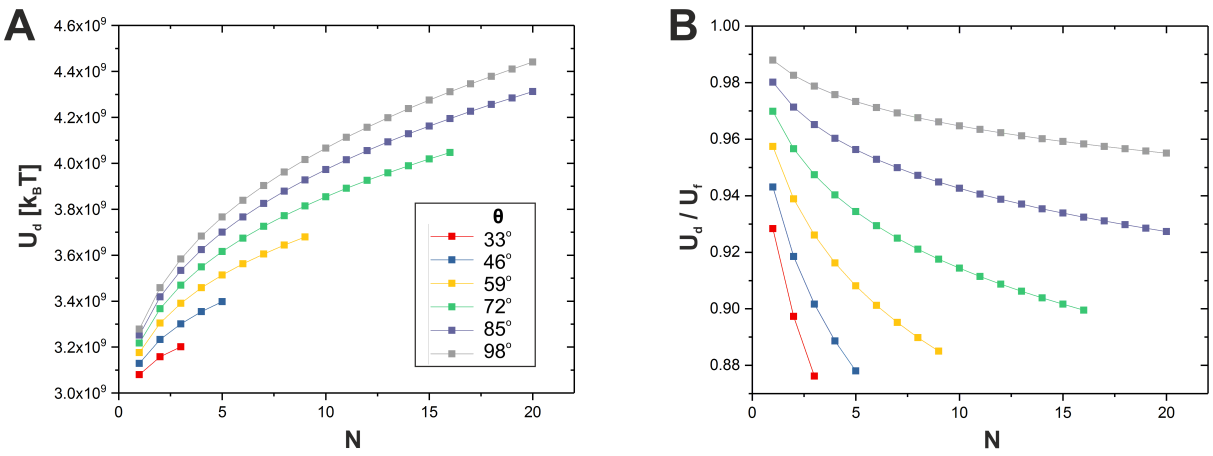


*Figure 6.7: (A) Total surface energy of attached droplets against number of droplets for different contact angles θ, given in the legend. (B) The same $U_d$ values for the attached droplet state shown in (A) but is now normalised with the corresponding free droplet state, $U_f$, plotted for the same θ values.*

$U_d/U_f < 1$, the surface energy of the attached lobes is lower than the free droplets state, so either dumbbells or raspberry particles can form. As $N$ increases, there is an increasing difference between $U_d$ and $U_f$, indicating that the attached lobe state is more stabilising than the free droplets state when $N$ is large compared to when $N$ is small. However it is worth noting that $N = 1$ is still remains the most energetically stable configuration.

### 6.4.3 Effect of seed particle size on surface energy

Next, we address the effects of the radius of the seed particle, $R$, on the total surface energy. By inspecting Eqn. 6.12, we can see that $R^2$ can be factorised out of the expression, which means that $U_d$ is directly proportional to $R^2$. In other words, the size of the seed particles influences the magnitude of the total surface energy, but does not affect the dependence of $U_d$ on $N$. However due to the surface area constraint of Eqn. 6.13, as the radius of the seed particle $R$ increases, a larger range of $N$ is allowed. This is consistent with what has been observed experimentally in Chapter 4, where the change in the size of the PS seed resulted in the same type of raspberry particle under idential reaction conditions.

### 6.4.4 Effect of contact angle on surface energy

Lastly, the effect of the contact angle $\theta$ has a complex connection with $U_d$, as seen from Eqn. 6.12, and it directly influences the two competing surface area contributions ($A_{12}$ and $A_{23}$) to the total surface energy. Fig. 6.7A shows that despite the changes in contact angle, the single lobe state is still the

most energetically favourable. However at lower contact angles, the cost of having more lobes is less than that at higher contact angles, signifying a greater probability of finding multi-lobed particles. Yet, the number of attached droplets is also much more limited for lower $\theta$, because each droplet covers a larger area of the seed particle surface. This is also seen in Fig. 6.7B, where the relative stabilities of the attached and unattached droplets are compared. Although at low contact angles, the attached state becomes more stabilising as $N$ increases, but the maximum number of droplets that can fit onto the seed particle surface is limited. However for the higher contact angles, though the extent of stabilisation is smaller with increasing $N$, it is possible for more droplets to exist on the surface. As such, a multi-lobed state is relatively more stable w.r.t. the free droplets state in a low contact angle system, and is more likely to be observed.

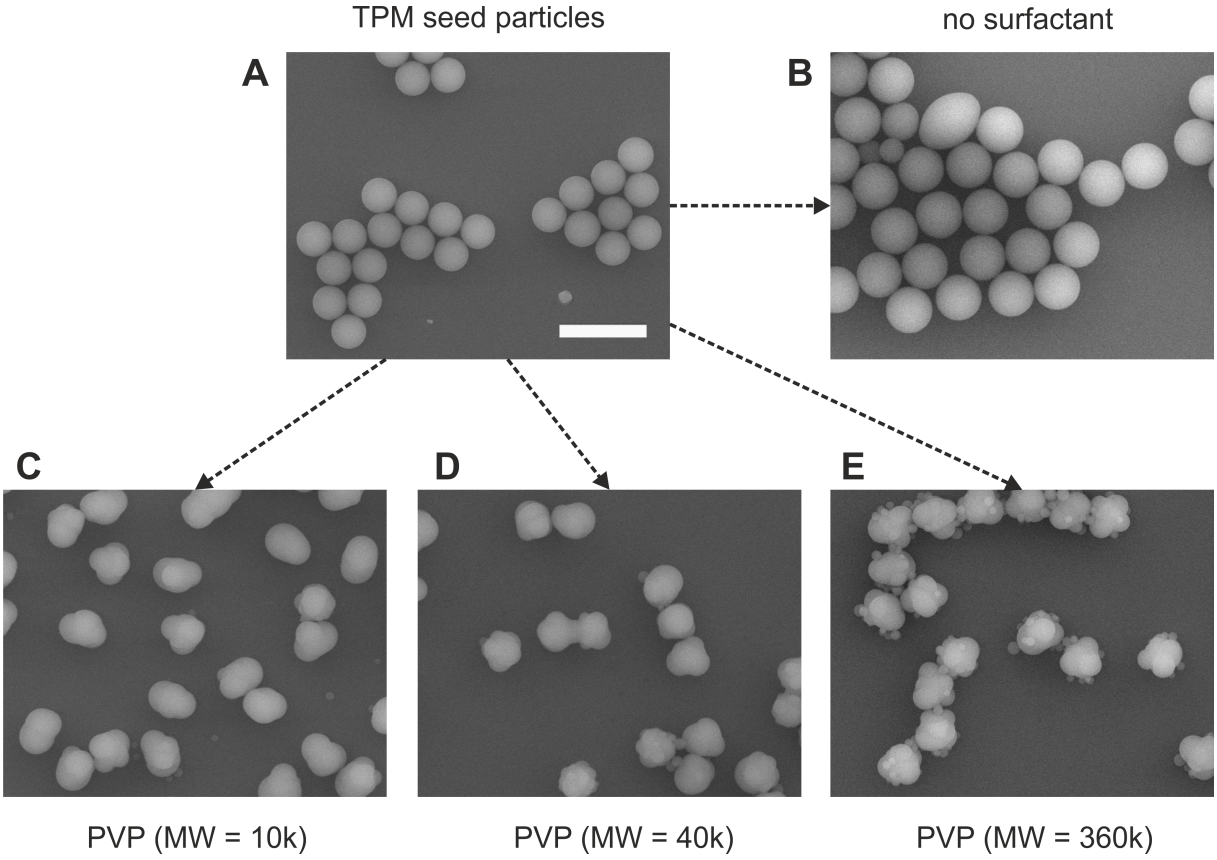


*Figure 6.8: SEM images of TPM seed particles coated with 2ml hTPM in a pH10 solution. The outcome of coating surfactant-free seeds is compared with those of seeds treated with PVP, where different morphologies have formed from the TPM coating. Scale bar = 5$\mu$m.*

Experimentally, we have tested the effect of changing $\theta$ using PVP on surfactant-free TPM seed particles and titania-coated PS seed particles. This is shown in Fig. 6.8 and Fig. 6.9 respectively. The TPM seed particles used here differ from the usual batches used for confocal microscopy in Chapter 3, because they were made without using F108 surfactant to stabilise the surface. Therefore when they are

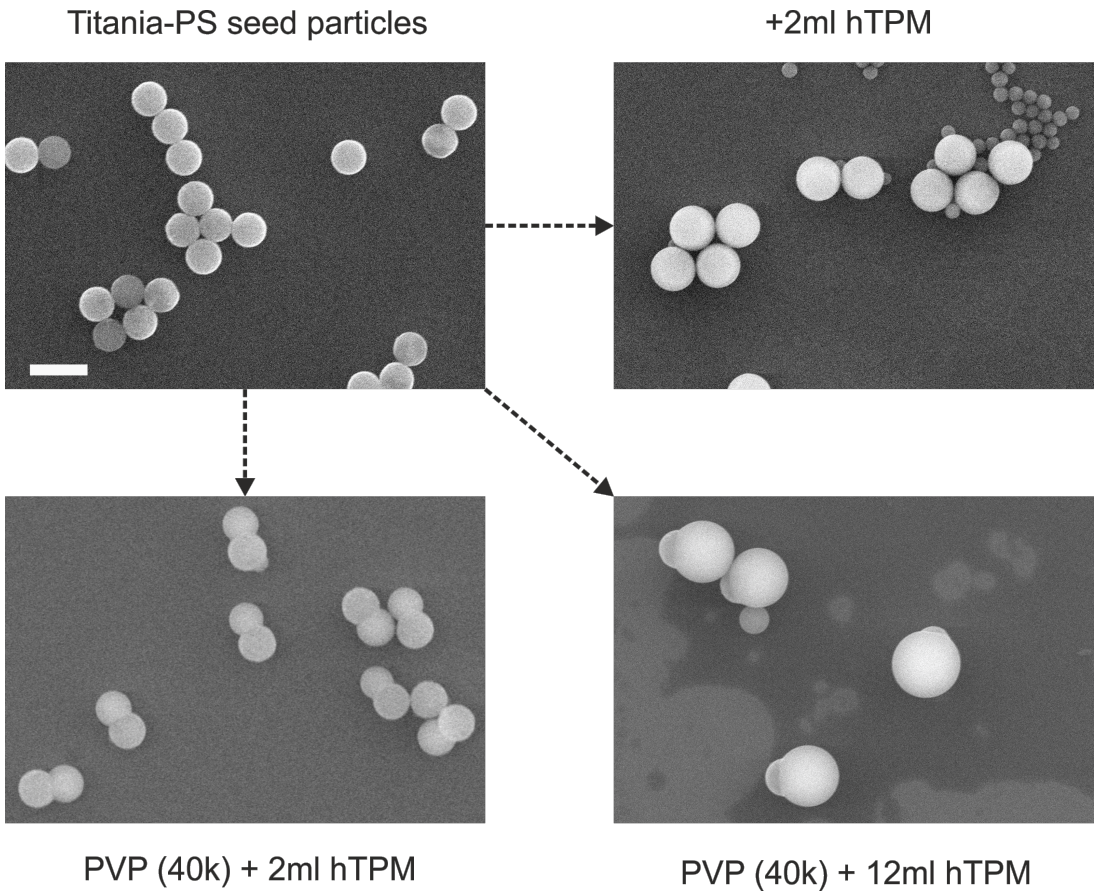


*Figure 6.9: SEM images showing Titania-PS seed particles before and after coating with hTPM. The effects of adding surfactant on the surface is shown, as well as the effects of increase in hTPM volume along with PVP. Scale bar = 2$\mu$m. The small particles seen in the background arise from secondary TPM nucleations.*

coated directly with hTPM solution as shown in Fig. 6.8B, the new TPM layer wets the surface of the seed completely, resulting in spherical particles, where the seed is positioned off-centre and near the surface of the resulting particle. The coating can be observed indirectly through the increase in the particle size, and through the occasional presence of olive-shaped particles (also seen in Fig. 6.8B), which were formed due to the joint coating of two seed particles. In contrast, when PVP surfactant is added during the coating of the seed particles, we observe clear lobes on the seed particle, with a wetting angle $\theta > 0°$ (Fig. 6.8C-E). This is expected as the surfactant decreases the surface tension between the seed and the solution, so the wetting between the seed and the TPM droplet is poorer. We have also noticed a change in the coating of the droplet as the molecular weight of the PVP changed. With increasing molecular weight of the PVP, better defined lobes are formed due to the increase in the contact angle $\theta$, and also more TPM droplets are able to fit onto the surface. This is consistent with the predictions obtained from the calculations in Fig. 6.7, and also explains the formation of TPM-TPM raspberry particles in Chapter 4, as those TPM seeds have F108 on the surface.

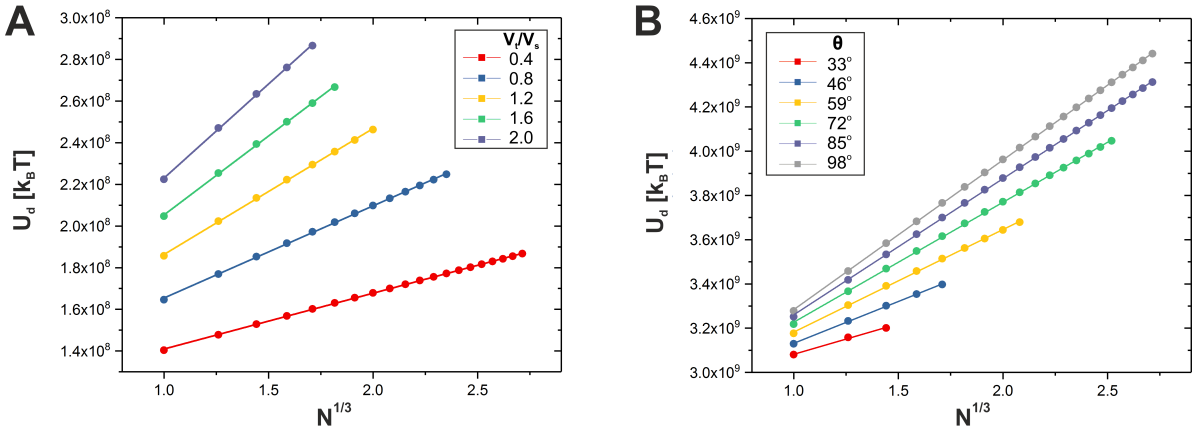


*Figure 6.10: Total surface energy plotted as a function of $N^{1/3}$ for the data in Fig. 6.6A and Fig. 6.7A respectively.*

Similarly, for the titania-PS seed particles, a direct coating with hTPM resulted in a very low contact angle between the TPM phase and the titania surface (Fig. 6.9). Again, the treatment with PVP has made a drastic change in the wetting behaviour of the TPM, resulting in dumbbell particles. By increasing the TPM quantity in the reaction, the lobes on the seed particles are grown to a greater size compared to before and is larger than the titania seeds, but the contact angle has remained the same. This can be seen in the last panel of Fig. 6.9.

### 6.4.5 Total surface energy as a function of droplet number

It is worth noting at this point that the second part of Eqn. 6.12, which represents the contribution to the total surface energy due to the presence of $N$ attached droplets, can be seen as $N\gamma_{23}$ multiplied by a surface area term $A*$. As such, this surface area term $A*$ must depend on the radius $r^2$ of each of the attached droplets. We know that $r \propto V_d^{1/3}$, and that $V_d \propto N^{-1}$, this implies that $A*$ must be proportional to $N^{-2/3}$. Together with $N\gamma_{23}$, this part of the equation indicates that $U_d$ has a $N^{1/3}$ dependence. To test this, Fig. 6.6A and Fig. 6.7A have been replotted in Fig. 6.10. Indeed the linearity of these plots confirm $U_d \propto N^{1/3}$. However we can also see that the degree of the dependence relies on the total volume of TPM $V_d$, as well as the contact angle $\theta$ in the system. At larger volumes and higher contact angles, the total surface energy increases much more rapidly as $N$ goes up.

### 6.4.6 Optical tweezing of dumbbell particles

Finally, we discuss the use of an optically anisotropic dumbbell in an optical tweezing experiment. By controlling the quantity of TPM and adding PVP, we obtained optically anisotropic MF-TPM dumbbell

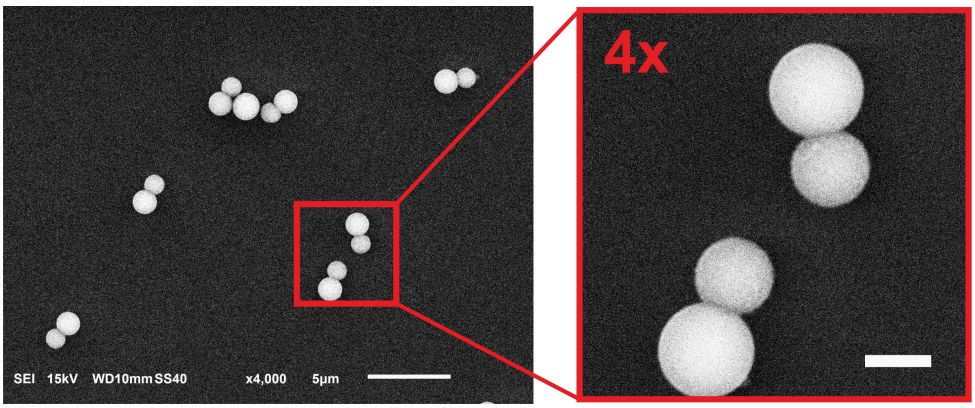


*Figure 6.11: SEM images of a batch of MF-TPM particles made using F108 surfactant addition. An enlarged image is shown on the right (Scale bar = 1 µm). These particles are used for the subsequent optical trapping experiments.*

particles with a large contact angle ($\theta \approx 120°$) and near 1:1 ratio between the two lobes (see Fig. 6.11). Given the refractive index contrast between the seed and the lobe in a MF-TPM dumbbell particle, by immersing these in a medium with $n_{TPM} < n_f < n_{MF}$, they become optically anisotropic. As shown in Fig. 6.3, the MF part has a positive index mismatch with the solvent, whereas the TPM part has a negative index mismatch with the solvent medium. Therefore the MF part of the dumbbell is naturally drawn towards the center of the optical trap. However the TPM lobe, which is repelled away from the focal point of the laser trap, does not reside in the same plane perpendicular to the trapping direction as the MF. Instead it is found at approximately 45° angle away from the incoming direction of the trap (See Fig. 6.3A). This is due to the combination of gravity and scattering forces experienced from incident laser beam. Nevertheless, despite this tilted orientation, we have observed that the TPM lobe undergoes rotational diffusion around the central MF seed that is held by the first optical trap. Due to the fixation of the MF part of the dumbbell, the movement of the TPM lobe is restricted to a ring.

Next, we performed live tracking of the position of the TPM lobe and retraced its trajectory with a second optical trap at a time-delays $\tau$ (FIg. 6.3B). The rate at which the TPM lobe moves away from the center of the second trap depends on its instantaneous distance away from the trap center, as well as the strength of the trap (i.e. the steepness of the repulsive potential). As such, by varying the delay time $\tau$, we can investigate different parts of the repulsive potential that the TPM lobe experiences on average. At short time-delays, we observe that the movement of the TPM lobe is highly oscillatory, as seen in the top row of Fig. 6.12. It is likely that when the chasing trap has been placed onto the $(t - \tau)$ position of the TPM lobe, it has not had sufficient time to diffuse away. As such, the TPM lobe would be near the top of the repulsive potential and may fall on either side of the potential hill, providing that the barrier is $< k_B T$. In contrast, at longer time delays (see bottom row of Fig. 6.12), the dynamics of the lobe becomes driven. This can be rationalised by considering that the average distance between the lobe and

the trap centre of the chasing trap is larger, as a larger $\tau$ means that the lobe is more likely to be found in a region of the trapping potential with the highest gradient. This provides a much greater repulsive force on the lobe, and as the potential barrier is now $> k_BT$, the particle is less likely to change direction. This leads towards a unidirectional driven rotation at large $\tau$, as seen in FIg. 6.12 for $\tau = 200ms$.

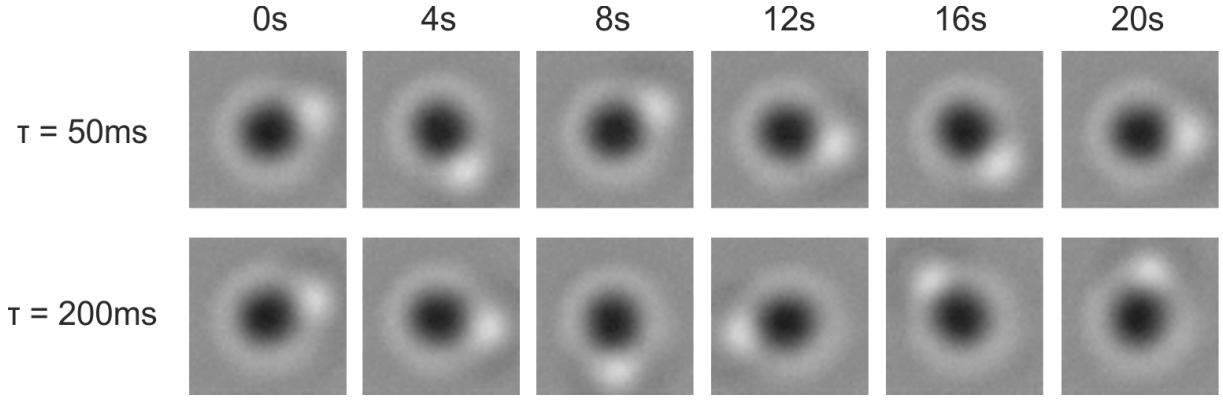


*Figure 6.12: Brightfield snapshots from the time-series of the preliminary two-trap tweezing experiment on a MF-TPM dumbbell particle, imaged in the focal plane the TPM lobe. Two different time-delays $\tau$ are shown here, which had the same trapping intensity of 4A. Oscillatory behaviour is seen for small $\tau$, but driven behaviour is seen for larger $\tau$ where the TPM lobe moves clockwise around the ring.*

The transition between oscillatory behaviour of the TPM lobe at short time-delays and the driven behaviour at larger time-delays is also confirmed by the particle trajectory over the entire time-series, shown in Fig. 6.3. We also observe that for different laser powers, the transition from the oscillatory behaviour to the driven behaviour occur at different $\tau$. With the increase in laser power and trap strength, the steepness of the potential is also increased, and the transition point occurs at shorter time-delays. Therefore we see in Fig. 6.3 that the lobe exhibit an oscillatory trajectory at the low laser power (2A) for $\tau = 100ms$, but instead appears driven at the higher laser power (4A) for the same time-delay.

From these preliminary experiments, it is clear that complex particles with new optical properties can lead to exciting optical trappng experiments. Future investigation could focus on exploring the correlation between the position of the TPM lobe and the position of the repulsive trap as a function of the feedback time-delay. This may lead us to a better understanding of the mutual information between the TPM lobe and the repulsive trap, as provided by the feedback of the lobe's trajectory on the trap's location.

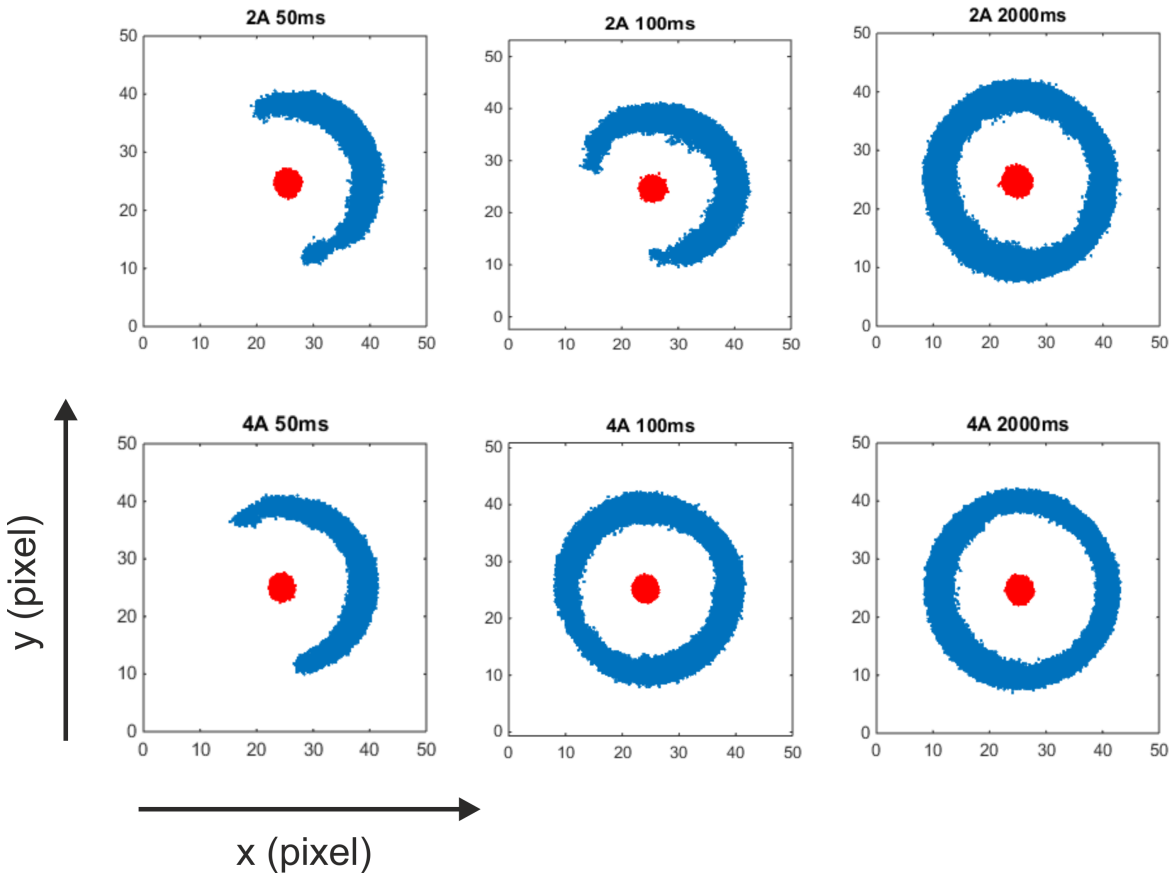


*Figure 6.13: Plots of all the detected MF positions (red) and TPM lobe positions (blue) in the trapping experiment of MF-TPM dumbbell particles using two optical tweezers. The axes are expressed in terms of the pixel values of the raw images. Top row: trap intensity = 2A. Bottom row: trap intensity = 4A. Each plot contains 1.2mil data points from the time series taken over the course of 20mins.*

## 6.5 Conclusion and outlook

In summary, we have investigated the influence of geometry on the total surface energy of a single-droplet and multi-droplet particles, examining in particular the effect of the volume of hTPM, the seed particle size, and the droplet contact angle may have on the total energy. From these numerical models we predicted the preferred particle geometry during a TPM-coating synthesis, and compared the predictions with experimental outcomes tested on titania-PS and TPM-PVP seed particles. Finally using the MF-TPM dumbbell particles that were derived from the surfactant tests, we developed a colloidal system that takes advantage of the optical anisotropy of the particles, and demonstrate their non-equilibrium dynamics when placed in a dual optical tweezing environment. The usual asymmetries observed here underlines the promise of optical tweezing experiments on optically anisotropic dumbbells.

## Acknowledgements

This work was done in collaboration with Dirk Aarts, Arran Curran and Bo Peng.

# Appendix

## A List of abbreviations

| | |
|---|---|
| % v/v | percentage by volume |
| % w/w | percentage by weight |
| $\epsilon$ | absorption coefficient |
| $\lambda$ | wavelength of electromagnetic radiation |
| $\mu$m | micron(s) |
| $\rho$ | density |
| $\phi$ | volume fraction |
| AIBN | $\alpha$-azo-iso-butyronitrile |
| APS | 3 aminopropyl trimethoxysilane |
| $^{\circ}C$ | degree(s) Celsius |
| CSLM | confocal scanning laser microscopy |
| DHM | digital holographic microscopy |
| DLS | dynamic light scattering |
| DMSO | dimethyl sulfoxide |
| e | Euler's number, $e = 2.71828...$ |
| hTPM | hydrolysed TPM |
| m | metre(s) |
| Me | methyl |
| MF | melamine formaldehyde |
| mins | minutes |
| ml | millilitre(s) |
| mol | mole(s) |
| Mol | molarity, $mol/dm^3$ |
| MW | molecular weight |
| $n_f$ | refractive index |
| NBD-MAEM | 4-methylamino ethylmethacrylate-7-nitrobenzo-2-oxa-1,3-diazol |

| | |
|---|---|
| nm | nanometer(s) |
| PEG | poly(ethlene glychol) |
| PERC | tetrachloroethylene |
| PPG | poly(propylene glycol) |
| PS | polystyrene |
| PVP | polyvinylpyrrolidone |
| RITC | rhodamine B isothiocyanate |
| RT | room temperature |
| s | second(s) |
| SEM | scanning electron microscopy |
| SLS | static light scattering |
| TCE | trichloroethylene |
| TPM | 3-(trimethoxysilyl) propyl methacrylate, 3-(methacryloyloxy)propyl trimethoxysilane |
| UV | ultraviolet |

# B Surface energy calculation derivations

The contact angle of a lobe on a spherical surface is defined as the angle nearest to the liquid lobe, and is marked out by the two tangents at the intersection of the contact point (as shown in Figure B.1A). This angle is geometrically identical to the angle $\theta$ shown in Figure 6.4B.

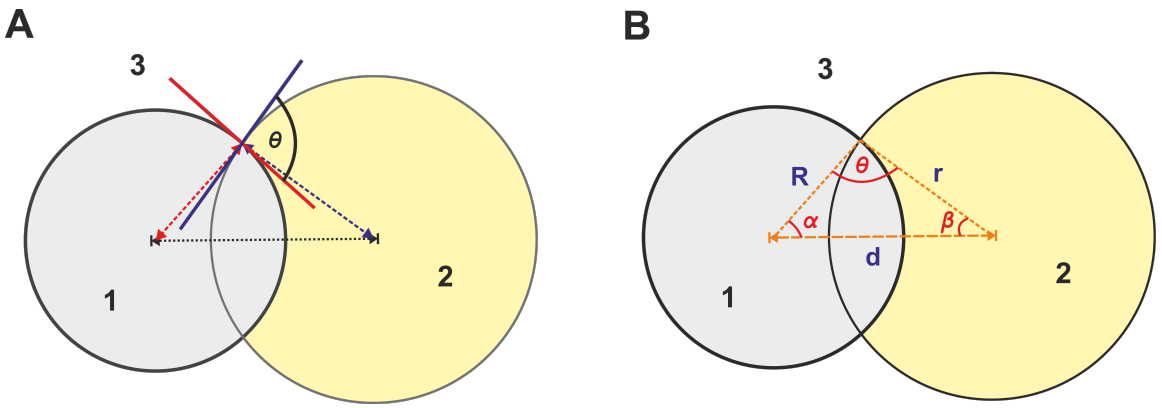


*Figure B.1: (A) The contact angle θ for a droplet on a curved surface (B) Triangular relationship between θ and the radius of phase 1, R, radius of phase 2, r, and the centre-to-centre distance of separation, d. The letters α and β denotes the angles between the centre-to-centre line to the centre-to-intersection point from phase 1 and phase 2 respectively.*

For two intersecting sphere, the volume of their overlap is:

$$V_{ov} = \frac{\pi(R + r - d)^2(d^2 + 2dr - 3r^2 + 2dR + 6rR - 3R^2)}{12d}, \tag{B.1}$$

where $R$ and $r$ are the radius of sphere 1 and sphere 2 respectively, as shown in Fig. B.1, and $d$ is the centre-to-centre distance between the two spheres.

Thus the volume of phase 2 is the difference between sphere 2 and the overlapped volume, $V_{ov}$:

$$V_d = \frac{4}{3}\pi r^3 - \frac{\pi(R + r - d)^2(d^2 + 2dr - 3r^2 + 2dR + 6rR - 3R^2)}{12d}. \tag{B.2}$$

To express $V_d$ in terms of $R$, $\theta$ and $\alpha$, first $r$ and $d$ need to be rewritten using the Sine rule:

$$r = \frac{\sin(\alpha)R}{\sin(\beta)}, \quad \text{and} \tag{B.3}$$

$$d = \frac{\sin(\theta)R}{\sin(\beta)}. \tag{B.4}$$

Here, $\beta = \pi - \theta - \alpha$ as per the geometric condition for a valid triangle. Substituting Eqns.B.3 and B.4

into Eqn.B.2, we obtain the full expression of the volume of phase 2 as:

$$V_{droplet} = \frac{4}{3}\pi R^3 A^3 - \frac{\pi R^3 (1 + A - T)^2 (T^2 + 2AT - 3A^2 + 2T + 6A - 3)}{12T}. \tag{B.5}$$

For clarity, $A$ and $T$ are used in Eqn. B.5 to denote:

$$A = \frac{\sin(\alpha)}{\sin(\theta + \alpha)}, \quad \text{and} \tag{B.6}$$

$$T = \frac{\sin(\theta)}{\sin(\theta + \alpha)}. \tag{B.7}$$

This expression for $V_d$ is used for the analysis of the one-to-one relationship with the angle $\alpha$ in Fig. B.1B. Due to the cyclic nature of the function, $V_d$ always equal zero at $2n\pi$ where $n \in \mathbb{N}$, and is asymptotic at $\alpha = \theta + 2n\pi$.

# C Description of videos

### Dragging core-shell particles though a dense suspension of TPM particles

Confocal time series video of 3$\mu$m diameter PS-TPM core-shell particles embedded in a dense crystalline region of fluorescently labelled TPM host particles, with only a sinlge core-shell particle shown in the field-of-view. The core and the lobes of the core-shell particle are not labelled, while the outer TPM shell is labelled with the same dye as the surrounding TPM host particles. The following three trajectories of the core-shell particle manipulation using an optical tweezer are provided. The data has not been modified from its original form.

**Description for 'timeseries-line-xy.avi' -** A cross-section in the x-y frame from a time series of confocal data in 2D. The core-shell particle is dragged along a straight line in the x-y plane over the duration of the data set.

**Description for 'timeseries-orbit-xy.avi' -** A cross-section in the x-y frame from a time series of z-stacks of confocal data. The core-shell particle is dragged along a circular orbit in the x-y plane over the duration of the data set.

**Description for 'timeseries-xyt-xzt.avi'-** A video of confocal data from a time-series of z-stacks in 3D. The core-shell particle is dragged along a circular orbit in the x-y plane while its z-coordinate is defined by a sine wave as a function of time. The video's two frames contain time-series from cross-sections in the x-y (top) and x-z (bottom) planes, providing tangential perspective from within the same z-stack for each frame. The red line in the top frame indicates the position of the x-z cross-section. The number in the upper left corner indicate the number of the frame, ranging from 0 - 131. This has been trimmed so that a full 360° rotation is shown in the video.

### Time-delay feedback trapping of MF-TPM dumbbell

2D time-series of brightfield images from a preliminary time-delay feedback trapping experiment of a MF-TPM dumbbell particle for three different time-delays, where the oscillation-driven transition delay-time $\tau_c$ is approximately 70ms.

**Description for 'Chase 30ms.avi'-** $\tau < \tau_c$, oscillatory behaviour of lobe is seen.

**Description for 'Chase 70ms.avi'-** $\tau \sim \tau_c$, lobe switches between oscillatory and driven.

**Description for 'Chase 100ms.avi'-** $\tau > \tau_c$, driven behaviour can be seen for lobe.

# Bibliography


[1] J. P. Hirth and J. Lothe, "Theory of dislocations," 1982.

[2] R. G. Larson, *The structure and rheology of complex fluids*, vol. 150. Oxford university press New York, 1999.

[3] R. Phillips, *Crystals, defects and microstructures: modeling across scales*. Cambridge University Press, 2001.

[4] R. Kern and R. Dassonville, "Growth inhibitors and promoters examplified on solution growth of paraffin crystals," *Journal of Crystal Growth*, vol. 116, pp. 191–203, Jan. 1992.

[5] K. J. Davis, P. M. Dove, and J. J. De Yoreo, "The Role of Mg2+ as an Impurity in Calcite Growth," *Science*, vol. 290, pp. 1134–1137, Nov. 2000.

[6] A. J. Malkin, Y. Kuznetsov, T. A. Land, J. J. DeYoreo, and A. McPherson, "Mechanisms of growth for protein and virus crystals," *Nature Structural & Molecular Biology*, vol. 2, pp. 956–959, Nov. 1995.

[7] J. Phillips, *Bonds and bands in semiconductors*. Elsevier, 2012.

[8] S. D. Durbin and G. Feher, "Protein crystallization," *Annual review of physical chemistry*, vol. 47, pp. 171–204, 1996.

[9] A. Cacciuto, S. Auer, and D. Frenkel, "Onset of heterogeneous crystal nucleation in colloidal suspensions," *Nature*, vol. 428, pp. 404–406, Mar. 2004.

[10] V. W. de Villeneuve, R. P. Dullens, D. G. Aarts, E. Groeneveld, J. H. Scherff, W. K. Kegel, and H. N. Lekkerkerker, "Colloidal hard-sphere crystal growth frustrated by large spherical impurities," *Science (New York, N.Y.)*, vol. 309, pp. 1231–1233, Aug. 2005.

[11] T. A. Land, T. L. Martin, S. Potapenko, G. T. Palmore, and J. J. De Yoreo, "Recovery of surfaces from impurity poisoning during crystal growth," *Nature*, vol. 399, pp. 442–445, June 1999.

[12] N. Kubota, "Effect of Impurities on the Growth Kinetics of Crystals," *Cryst. Res. Technol.*, vol. 36, pp. 749–769, Oct. 2001.

[13] B. Li, D. Zhou, and Y. Han, "Assembly and phase transitions of colloidal crystals," *Nature Reviews Materials*, vol. 1, pp. 15011+, Jan. 2016.

[14] E. O. Hall, "The Deformation and Ageing of Mild Steel: III Discussion of Results," *Proceedings of the Physical Society. Section B*, vol. 64, pp. 747–753, Sept. 1951.

[15] N. J. Petch, "The Cleavage Strength of Polycrystals," *Journal of the Iron and Steel Institute*, vol. 174, pp. 25–28, 1953.

[16] J. Schiotz, F. D. Di Tolla, and K. W. Jacobsen, "Softening of nanocrystalline metals at very small grain sizes," *Nature*, vol. 391, pp. 561–563, Feb. 1998.

[17] H. Van Swygenhoven, "Grain Boundaries and Dislocations," *Science*, vol. 296, pp. 66–67, Apr. 2002.

[18] S. Yip, "Nanocrystals: The strongest size," *Nature*, vol. 391, pp. 532–533, Feb. 1998.

[19] G. Duscher, M. F. Chisholm, U. Alber, and M. Ruhle, "Bismuth-induced embrittlement of copper grain boundaries," *Nature Materials*, vol. 3, pp. 621–626, Aug. 2004.

[20] J. J. Hoyt, "On the coarsening of precipitates located on grain boundaries and dislocations," *Acta Metallurgica et Materialia*, vol. 39, pp. 2091–2098, Sept. 1991.

[21] P. N. Pusey, "Liquids, freezing and the glass transition," 1991.

[22] A. J. Liu and S. R. Nagel, "Nonlinear dynamics: Jamming is not just cool any more," *Nature*, vol. 396, pp. 21–22, Nov. 1998.

[23] J. Li, Z. L. Wang, and T. C. Hufnagel, "Characterization of nanometer-scale defects in metallic glasses by quantitative high-resolution transmission electron microscopy," *Physical Review B*, vol. 65, Mar. 2002.

[24] A. Guinier, *X-ray diffraction in crystals, imperfect crystals, and amorphous bodies*. Courier Corporation, 1994.

[25] Z. G. Pinsker, *Dynamical Scattering of X-rays in Crystals*, vol. 3. Springer-Verlag Berlin, 1978.

[26] F. Sette, M. H. Krisch, C. Masciovecchio, G. Ruocco, and G. Monaco, "Dynamics of Glasses and Glass-Forming Liquids Studied by Inelastic X-ray Scattering," *Science*, vol. 280, pp. 1550–1555, June 1998.

[27] T. Graham, "Liquid Diffusion Applied to Analysis," *Philosophical Transactions of the Royal Society of London*, vol. 151, pp. 183–224, Jan. 1861.

[28] R. Brown and J. J. Bennett, *The Miscellaneous Botanical Works of Robert Brown*, vol. 1. Cambridge University Press, 2015.

[29] D. F. Evans and H. Wennerstrom, *Colloidal domain*. Wiley-Vch, 1999.

[30] P. N. Pusey and W. van Megen, "Phase behaviour of concentrated suspensions of nearly hard colloidal spheres," *Nature*, vol. 320, pp. 340–342, Mar. 1986.

[31] E. R. Weeks, *Soft jammed materials*.

[32] M. Sindoro and S. Granick, "Voids and Yolk-Shells from Crystals That Coat Particles," *J. Am. Chem. Soc.*, vol. 136, pp. 13471–13473, Oct. 2014.

[33] A. Kuijk, A. van Blaaderen, and A. Imhof, "Synthesis of Monodisperse, Rodlike Silica Colloids with Tunable Aspect Ratio," *J. Am. Chem. Soc.*, vol. 133, pp. 2346–2349, Mar. 2011.

[34] L. Rossi, S. Sacanna, W. T. M. Irvine, P. M. Chaikin, D. J. Pine, and A. P. Philipse, "Cubic crystals from cubic colloids," *Soft Matter*, vol. 7, no. 9, pp. 4139–4142, 2011.

[35] T. Sugimoto, A. Muramatsu, K. Sakata, and D. Shindo, "Characterization of Hematite Particles of Different Shapes," *Journal of Colloid and Interface Science*, vol. 158, pp. 420–428, July 1993.

[36] J.-G. Park, J. D. Forster, and E. R. Dufresne, "High-Yield Synthesis of Monodisperse Dumbbell-Shaped Polymer Nanoparticles," *J. Am. Chem. Soc.*, vol. 132, pp. 5960–5961, May 2010.

[37] S. Sacanna, M. Korpics, K. Rodriguez, L. Colón-Meléndez, S.-H. H. Kim, D. J. Pine, and G.-R. R. Yi, "Shaping colloids for self-assembly," *Nature communications*, vol. 4, 2013.

[38] K. Zahn, R. Lenke, and G. Maret, "Two-Stage Melting of Paramagnetic Colloidal Crystals in Two Dimensions," *Physical Review Letters*, vol. 82, pp. 2721–2724, Mar. 1999.

[39] B. Liu, T. H. Besseling, M. Hermes, A. F. Demirörs, A. Imhof, and A. van Blaaderen, "Switching plastic crystals of colloidal rods with electric fields," *Nature Communications*, vol. 5, Jan. 2014.

[40] A. Yethiraj and A. van Blaaderen, "A colloidal model system with an interaction tunable from hard sphere to soft and dipolar," *Nature*, vol. 421, pp. 513–517, Jan. 2003.

[41] S. Sacanna, L. Rossi, and D. J. Pine, "Magnetic Click Colloidal Assembly," *J. Am. Chem. Soc.*, vol. 134, pp. 6112–6115, Apr. 2012.

[42] S. Ravaine and E. Duguet, "Synthesis and assembly of patchy particles: Recent progress and future prospects," *Current Opinion in Colloid & Interface Science*, vol. 30, pp. 45–53, July 2017.

[43] M. J. Solomon, "Materials science: Reconfigurable colloids," *Nature*, vol. 464, pp. 496–498, Mar. 2010.

[44] A. L. Thorneywork, J. L. Abbott, D. G. Aarts, and R. P. Dullens, "Two-Dimensional Melting of Colloidal Hard Spheres," *Physical Review Letters*, vol. 118, Apr. 2017.

[45] P. N. Pusey, W. V. Megen, S. M. Underwood, P. Bartlett, and R. H. Ottewill, "Colloidal fluids, crystals and glasses," *Journal of Physics: Condensed Matter*, vol. 2, pp. SA373–SA377, Dec. 1990.

[46] E. Dickinson, G. Stainsby, and Others, *Colloids in food.* Applied Science Publishers, 1982.

[47] V. Schroder, O. Behrend, and H. Schubert, "Effect of Dynamic Interfacial Tension on the Emulsification Process Using Microporous, Ceramic Membranes," *Journal of Colloid and Interface Science*, vol. 202, pp. 334–340, June 1998.

[48] Blaaderen, "MATERIALS SCIENCE: Opals in a New Light," *Science*, vol. 282, pp. 887–888, Oct. 1998.

[49] A. Vonarbourg, C. Passirani, P. Saulnier, and J.-P. Benoit, "Parameters influencing the stealthiness of colloidal drug delivery systems," *Biomaterials*, vol. 27, pp. 4356–4373, Aug. 2006.

[50] S. Rose, A. Prevoteau, P. Elziere, D. Hourdet, A. Marcellan, and L. Leibler, "Nanoparticle solutions as adhesives for gels and biological tissues," *Nature*, vol. 505, pp. 382–385, Jan. 2014.

[51] A. Blanco, E. Chomski, S. Grabtchak, M. Ibisate, S. John, S. W. Leonard, C. Lopez, F. Meseguer, H. Miguez, J. P. Mondia, G. A. Ozin, O. Toader, and H. M. van Driel, "Large-scale synthesis of a silicon photonic crystal with a complete three-dimensional bandgap near 1.5 micrometres," *Nature*, vol. 405, pp. 437–440, May 2000.

[52] T. Ding, Y. Long, K. Zhong, K. Song, G. Yang, and C.-H. Tung, "Modifying the symmetry of colloidal photonic crystals: a way towards complete photonic bandgap," *Journal of Materials Chemistry C*, vol. 2, no. 21, pp. 4100+, 2014.

[53] J. A. Lewis, "Colloidal Processing of Ceramics," *Journal of the American Ceramic Society*, vol. 83, pp. 2341–2359, Oct. 2000.

[54] D. G. Grier, "A revolution in optical manipulation," *Nature*, vol. 424, pp. 810–816, Aug. 2003.

[55] L. G. Wilson, A. W. Harrison, A. B. Schofield, J. Arlt, and W. C. K. Poon, "Passive and Active Microrheology of Hard-sphere Colloids," *J. Phys. Chem. B*, vol. 113, pp. 3806–3812, Mar. 2009.

[56] A. M. Puertas and T. Voigtmann, "Microrheology of colloidal systems," *Journal of Physics: Condensed Matter*, vol. 26, pp. 243101+, June 2014.

[57] K. Yoshizawa, A. Toyotama, T. Okuzono, and J. Yamanaka, "Exclusion of impurity particles in charged colloidal crystals," *Soft Matter*, vol. 10, no. 19, pp. 3357–3361, 2014.

[58] G. Ovarlez, Q. Barral, and P. Coussot, "Three-dimensional jamming and flows of soft glassy materials," *Nature Materials*, vol. 9, pp. 115–119, Jan. 2010.

[59] P. Habdas, D. Schaar, A. C. Levitt, and E. R. Weeks, "Forced motion of a probe particle near the colloidal glass transition," *Europhysics Letters (EPL)*, vol. 67, pp. 477–483, Aug. 2004.

[60] E. R. Weeks, J. C. Crocker, A. C. Levitt, A. Schofield, and D. A. Weitz, "Three-Dimensional Direct Imaging of Structural Relaxation Near the Colloidal Glass Transition," *Science*, vol. 287, pp. 627–631, Jan. 2000.

[61] V. Prasad, D. Semwogerere, and E. R. Weeks, "Confocal microscopy of colloids," *Journal of Physics: Condensed Matter*, vol. 19, pp. 113102+, Mar. 2007.

[62] F. A. Lavergne, S. Diana, D. G. A. L. Aarts, and R. P. A. Dullens, "Equilibrium Grain Boundary Segregation and Clustering of Impurities in Colloidal Polycrystalline Monolayers," *Langmuir*, vol. 32, pp. 12716–12724, Dec. 2016.

[63] V. W. A. D. Villeneuve, D. Verboekend, R. P. A. Dullens, D. G. A. L. Aarts, W. K. Kegel, and H. N. W. Lekkerkerker, "Hard sphere crystal nucleation and growth near large spherical impurities," *Journal of Physics: Condensed Matter*, vol. 17, pp. S3371–S3378, Nov. 2005.

[64] S. E. Skelton Spesyvtseva and K. Dholakia, "Trapping in a Material World," *ACS Photonics*, Apr. 2016.

[65] D. L. J. Vossen, A. van der Horst, M. Dogterom, and A. van Blaaderen, "Optical tweezers and confocal microscopy for simultaneous three-dimensional manipulation and imaging in concentrated colloidal dispersions," *Review of Scientific Instruments*, vol. 75, pp. 2960–2970, Sept. 2004.

[66] H. Hoffmann and F. Steinbauer, "Single domain and vortex state in ferromagnetic circular nanodots," *Journal of Applied Physics*, vol. 92, pp. 5463–5467, Nov. 2002.

[67] Y. Yasuno, S. Makita, T. Yatagai, T. Wiesendanger, A. Ruprecht, and H. Tiziani, "Non-mechanically-axial-scanning confocal microscope using adaptive mirror switching," *Optics Express*, vol. 11, pp. 54+, Jan. 2003.

[68] S. A. Khan and N. A. Riza, "Demonstration of a no-moving-parts axial scanning confocal microscope using liquid crystal optics," *Optics Communications*, vol. 265, pp. 461–467, Sept. 2006.

[69] K. D. Wulff, D. G. Cole, R. L. Clark, R. DiLeonardo, J. Leach, J. Cooper, G. Gibson, and M. J. Padgett, "Aberration correction in holographic optical tweezers," *Optics Express*, vol. 14, pp. 4169–4174, May 2006.

[70] M. Dienerowitz, G. Gibson, R. Bowman, and M. Padgett, "Holographic aberration correction: optimising the stiffness of an optical trap deep in the sample," *Optics Express*, vol. 19, pp. 24589+, Nov. 2011.

[71] A. Curran, S. Tuohy, D. G. A. L. Aarts, M. J. Booth, T. Wilson, and R. P. A. Dullens, "Decoupled and simultaneous three-dimensional imaging and optical manipulation through a single objective," *Optica*, vol. 1, no. 4, pp. 223–226, 2014.

[72] M. Yevnin, D. Kasimov, Y. Gluckman, Y. Ebenstein, and Y. Roichman, "Independent and simultaneous three-dimensional optical trapping and imaging," *Biomedical Optics Express*, vol. 4, pp. 2087+, Sept. 2013.

[73] M. Hermes, E. C. M. Vermolen, M. E. Leunissen, D. L. J. Vossen, P. D. J. van Oostrum, M. Dijkstra, and A. van Blaaderen, "Nucleation of colloidal crystals on configurable seed structures," *Soft Matter*, vol. 7, no. 10, pp. 4623–4628, 2011.

[74] W. T. M. Irvine, V. Vitelli, and P. M. Chaikin, "Pleats in crystals on curved surfaces," *Nature*, vol. 468, pp. 947–951, Dec. 2010.

[75] T. Sugimoto, *Monodispersed particles*. Elsevier, 2001.

[76] D. H. Everett, *Basic principles of colloid science*. Royal Society of Chemistry, 1988.

[77] T. Sugimoto, "Spontaneous nucleation of monodisperse silver halide particles from homogeneous gelatin solution I: silver chloride," *Colloids and Surfaces A: Physicochemical and Engineering Aspects*, vol. 164, pp. 183–203, May 2000.

[78] R. P. A. Dullens, *Structure and dynamics of colloidal hard spheres in real-space*. PhD thesis, 2005.

[79] M. Keating, Y. Chen, I. A. Larmour, K. Faulds, and D. Graham, "Growth and surface-enhanced Raman scattering of Ag nanoparticle assembly in agarose gel," *Measurement Science and Technology*, vol. 23, pp. 084006+, Aug. 2012.

[80] R. A. L. Jones, *Soft condensed matter*. Oxford University Press, 2002.

[81] J. N. Israelachvili, *Intermolecular and surface forces*. Academic press, 2011.

[82] P. S. Yadav, D. Dupre, R. Tadmor, J. S. Park, and D. Katoshevski, "Effective refractive index and intermolecular forces associated with a phase of functional groups," *Surface Science*, vol. 601, pp. 4582–4585, Oct. 2007.

[83] E. J. W. Verwey, "Theory of the Stability of Lyophobic Colloids.," *J. Phys. Chem.*, vol. 51, pp. 631–636, Mar. 1947.

[84] S. K. Sainis, V. Germain, C. O. Mejean, and E. R. Dufresne, "Electrostatic interactions of colloidal particles in nonpolar solvents: role of surface chemistry and charge control agents," *Langmuir : the ACS journal of surfaces and colloids*, vol. 24, pp. 1160–1164, Feb. 2008.

[85] A. Einstein, *Investigations on the Theory of the Brownian Movement*. Courier Corporation, 1956.

[86] J. Perrin, "Mouvement brownien et réalité moléculaire," in *Annales de Chimie et de Physique*, vol. 18, pp. 5–104, 1909.

[87] P. J. Debye, *Polar molecules*. Chemical Catalog Company, Incorporated, 1929.

[88] W. G. Hoover and F. H. Ree, "Melting Transition and Communal Entropy for Hard Spheres," *The Journal of Chemical Physics*, vol. 49, pp. 3609–3617, Oct. 1968.

[89] C. P. Royall, W. C. K. Poon, and E. R. Weeks, "In search of colloidal hard spheres," *Soft Matter*, vol. 9, no. 1, pp. 17–27, 2013.

[90] A.-P. Hynninen and M. Dijkstra, "Phase diagrams of hard-core repulsive Yukawa particles," *Physical Review E*, vol. 68, pp. 021407+, Aug. 2003.

[91] S. R. Williams, I. K. Snook, and W. van Megen, "Molecular dynamics study of the stability of the hard sphere glass," *Phys. Rev. E*, vol. 64, pp. 021506+, July 2001.

[92] I. Moriguchi, K. Kawasaki, and T. Kawakatsu, "The effects of size polydispersity in nearly hard sphere colloids," *Journal de Physique II*, vol. 3, pp. 1179–1184, Aug. 1993.

[93] H. C. Hulst and H. C. van de Hulst, *Light scattering by small particles*. Courier Corporation, 1957.

[94] R. L. Rowell, T. P. Wallace, and J. P. Kratohvil, "Determination of the number concentration of polydisperse colloidal spheres by light scattering," *Journal of Colloid and Interface Science*, vol. 26, pp. 494–499, Apr. 1968.

[95] W. van Megen and P. N. Pusey, "Dynamic light-scattering study of the glass transition in a colloidal suspension," *Physical Review A*, vol. 43, pp. 5429–5441, May 1991.

[96] S.-H. Lee, Y. Roichman, G.-R. Yi, S.-H. Kim, S.-M. Yang, A. van Blaaderen, P. van Oostrum, and D. G. Grier, "Characterizing and tracking single colloidal particles with video holographic microscopy," *Optics Express*, vol. 15, pp. 18275–18282, Dec. 2007.

[97] J. Fung, K. E. Martin, R. W. Perry, D. M. Kaz, R. McGorty, and V. N. Manoharan, "Measuring translational, rotational, and vibrational dynamics in colloids with digital holographic microscopy," *Optics Express*, vol. 19, pp. 8051–8065, Apr. 2011.

[98] H. C. King, *The history of the telescope*. Courier Corporation, 1955.

[99] A. Ashkin, "Acceleration and Trapping of Particles by Radiation Pressure," *Phys. Rev. Lett.*, vol. 24, pp. 156–159, Jan. 1970.

[100] A. Ashkin and J. M. Dziedzic, "Optical Levitation by Radiation Pressure," *Applied Physics Letters*, vol. 19, pp. 283–285, Oct. 1971.

[101] A. Ashkin, J. M. Dziedzic, J. E. Bjorkholm, and S. Chu, "Observation of a single-beam gradient force optical trap for dielectric particles," *Optics Letters*, vol. 11, pp. 288–290, May 1986.

[102] P. A. M. Neto and H. M. Nussenzveig, "Theory of optical tweezers," *Europhysics Letters (EPL)*, vol. 50, pp. 702–708, June 2000.

[103] A. Ashkin, "Forces of a single-beam gradient laser trap on a dielectric sphere in the ray optics regime," *Biophys. J.*, vol. 61, no. 2 I, pp. 569–582, 1992.

[104] J. C. Crocker and D. G. Grier, "Methods of Digital Video Microscopy for Colloidal Studies," *Journal of Colloid and Interface Science*, vol. 179, pp. 298–310, Apr. 1996.

[105] J. Perrin, "Atoms, trans. DL Hammick," 1923.

[106] P. N. Pusey and W. van Megen, "Observation of a glass transition in suspensions of spherical colloidal particles," *Physical Review Letters*, vol. 59, pp. 2083–2086, Nov. 1987.

[107] W. Poon and H. Lekkerkerker, "Colloids in suspense," *Physics World*, vol. 9, no. 4, pp. 27–32, 1996.

[108] W. K. Kegel, "Direct Observation of Dynamical Heterogeneities in Colloidal Hard-Sphere Suspensions," *Science*, vol. 287, pp. 290–293, Jan. 2000.

[109] P. J. Lu, E. Zaccarelli, F. Ciulla, A. B. Schofield, F. Sciortino, and D. A. Weitz, "Gelation of particles with short-range attraction," *Nature*, vol. 453, pp. 499–503, May 2008.

[110] U. Gasser, "Real-Space Imaging of Nucleation and Growth in Colloidal Crystallization," *Science*, vol. 292, pp. 258–262, Apr. 2001.

[111] A. van Blaaderen and P. Wiltzius, "Real-Space Structure of Colloidal Hard-Sphere Glasses," *Science*, vol. 270, pp. 1177–1179, Nov. 1995.

[112] G. Bosma, C. Pathmamanoharan, E. H. A. de Hoog, W. K. Kegel, A. van Blaaderen, and H. N. W. Lekkerkerker, "Preparation of Monodisperse, Fluorescent PMMA-Latex Colloids by Dispersion Polymerization," *Journal of Colloid and Interface Science*, vol. 245, pp. 292–300, Jan. 2002.

[113] S. Sacanna, W. T. M. Irvine, L. Rossi, and D. J. Pine, "Lock and key colloids through polymerization-induced buckling of monodisperse silicon oil droplets," *Soft Matter*, vol. 7, no. 5, pp. 1631–1634, 2011.

[114] S. Sacanna, W. T. M. Irvine, P. M. Chaikin, and D. J. Pine, "Lock and key colloids," *Nature*, vol. 464, pp. 575–578, Mar. 2010.

[115] B. M. Novak, "Hybrid Nanocomposite Materials-between inorganic glasses and organic polymers," *Adv. Mater.*, vol. 5, pp. 422–433, June 1993.

[116] Z. Huang and K. Qiu, "Preparation and thermal property of poly(methyl methacrylate)/silicate hybrid materials by the in-situ sol-gel process," vol. 35, no. 5, pp. 607–613, 1995.

[117] W.-C. Chen, S.-J. Lee, L.-H. Lee, and J.-L. Lin, "Synthesis and characterization of trialkoxysilane-capped poly(methyl methacrylate)-titania hybrid optical thin films," *J. Mater. Chem.*, vol. 9, no. 12, pp. 2999–3003, 1999.

[118] K. Zhang, H. Chen, X. Chen, Z. Chen, Z. Cui, and B. Yang, "Monodisperse Silica-Polymer Core-Shell Microspheres via Surface Grafting and Emulsion Polymerization," *Macromol. Mater. Eng.*, vol. 288, pp. 380–385, Apr. 2003.

[119] T. M. Obey and B. Vincent, "Novel Monodisperse "Silicone Oil"/Water Emulsions," *Journal of Colloid and Interface Science*, vol. 163, pp. 454–463, Mar. 1994.

[120] S. Sacanna and D. J. Pine, "Shape-anisotropic colloids: Building blocks for complex assemblies," *Current Opinion in Colloid & Interface Science*, vol. 16, pp. 96–105, Apr. 2011.

[121] S. J. Ivell, R. P. A. Dullens, S. Sacanna, and D. G. A. L. Aarts, "Emerging structural disorder in a suspension of uniformly dimpled colloidal particles," *Soft Matter*, vol. 9, no. 39, pp. 9361–9365, 2013.

[122] T. J. Barnes and C. A. Prestidge, "PEO-PPO-PEO Block Copolymers at the Emulsion Droplet-Water Interface," *Langmuir*, vol. 16, pp. 4116–4121, Mar. 2000.

[123] M. F. Hsu, E. R. Dufresne, and D. A. Weitz, "Charge Stabilization in Nonpolar Solvents," *Langmuir*, vol. 21, pp. 4881–4887, May 2005.

[124] M. Hannel, C. Middleton, and D. G. Grier, "Holographic characterization of imperfect colloidal spheres," Aug. 2015.

[125] S. Wiederseiner, N. Andreini, G. Epely-Chauvin, and C. Ancey, "Refractive-index and density matching in concentrated particle suspensions: a review," *Experiments in Fluids*, vol. 50, pp. 1183–1206, May 2011.

[126] W. Lechner and C. Dellago, "Accurate determination of crystal structures based on averaged local bond order parameters," *The Journal of Chemical Physics*, vol. 129, pp. 114707+, Sept. 2008.

[127] W. C. K. Poon, E. R. Weeks, and C. P. Royall, "On measuring colloidal volume fractions," June 2011.

[128] S. Buzzaccaro, R. Rusconi, and R. Piazza, ""Sticky" Hard Spheres: Equation of State, Phase Diagram, and Metastable Gels," *Phys. Rev. Lett.*, vol. 99, pp. 098301+, Aug. 2007.

[129] G. L. Hunter and E. R. Weeks, "The physics of the colloidal glass transition," *Reports on Progress in Physics*, vol. 75, pp. 066501+, June 2012.

[130] F. Caruso, "Nanoengineering of Particle Surfaces," *Adv. Mater.*, vol. 13, pp. 11–22, Jan. 2001.

[131] M. S. Fleming, T. K. Mandal, and D. R. Walt, "Nanosphere-Microsphere Assembly: Methods for Core-Shell Materials Preparation," *Chem. Mater.*, vol. 13, pp. 2210–2216, May 2001.

[132] R. P. A. Dullens, Claesson, D. Derks, A. van Blaaderen, and W. K. Kegel, "Monodisperse Core-Shell Poly(methyl methacrylate) Latex Colloids," *Langmuir*, vol. 19, pp. 5963–5966, June 2003.

[133] M. T. Elsesser, A. D. Hollingsworth, K. V. Edmond, and D. J. Pine, "Large Core-Shell Poly(methyl methacrylate) Colloidal Clusters: Synthesis, Characterization, and Tracking," *Langmuir*, vol. 27, pp. 917–927, Feb. 2011.

[134] T.-S. Deng and F. Marlow, "Synthesis of Monodisperse Polystyrene@Vinyl-SiO2 Core-Shell Particles and Hollow SiO2 Spheres," *Chem. Mater.*, vol. 24, pp. 536–542, Feb. 2012.

[135] R. Pelton, "Temperature-sensitive aqueous microgels," *Advances in Colloid and Interface Science*, vol. 85, pp. 1–33, Feb. 2000.

[136] W. Schärtl, "Crosslinked Spherical Nanoparticles with Core-Shell Topology," *Adv. Mater.*, vol. 12, pp. 1899–1908, Dec. 2000.

[137] A. Perro, G. Meng, J. Fung, and V. N. Manoharan, "Design and Synthesis of Model Transparent Aqueous Colloids with Optimal Scattering Properties," *Langmuir*, vol. 25, pp. 11295–11298, Sept. 2009.

[138] S. U. Pickering, "CXCVI.-Emulsions," *J. Chem. Soc., Trans.*, vol. 91, no. 0, pp. 2001–2021, 1907.

[139] D. M. Kaz, R. McGorty, M. Mani, M. P. Brenner, and V. N. Manoharan, "Physical ageing of the contact line on colloidal particles at liquid interfaces," *Nat Mater*, vol. 11, pp. 138–142, Feb. 2012.

[140] T. A. Nieminen, V. L. Y. Loke, A. B. Stilgoe, G. Knöner, A. M. Brańczyk, N. R. Heckenberg, and H. Rubinsztein-Dunlop, "Optical tweezers computational toolbox," *Journal of Optics A: Pure and Applied Optics*, vol. 9, pp. S196–S203, Aug. 2007.

[141] Y. Wu, Y. Li, L. Qin, F. Yang, and D. Wu, "Monodispersed or narrow-dispersed melamine-formaldehyde resin polymer colloidal spheres: preparation, size-control, modification, bioconjugation and particle formation mechanism," *J. Mater. Chem. B*, vol. 1, no. 2, pp. 204–212, 2013.

[142] L. Onsager, "The effects of shape on the interaction of colloidal particles," *Annals of the New York Academy of Sciences*, vol. 51, pp. 627–659, May 1949.

[143] H. N. W. Lekkerkerker and R. Tuinier, *Colloids and the depletion interaction*, vol. 833. Springer, 2011.

[144] M. G. Noro and D. Frenkel, "Extended corresponding-states behavior for particles with variable range attractions," *The Journal of Chemical Physics*, vol. 113, pp. 2941–2944, Aug. 2000.

[145] S. Asakura and F. Oosawa, "On Interaction between Two Bodies Immersed in a Solution of Macromolecules," *The Journal of Chemical Physics*, vol. 22, pp. 1255–1256, July 1954.

[146] S. Asakura and F. Oosawa, "Interaction between particles suspended in solutions of macromolecules," *J. Polym. Sci.*, vol. 33, pp. 183–192, Dec. 1958.

[147] F. K. R. Li-In-On, B. Vincent, and F. A. Waite, "Stability of Sterically Stabilized Dispersions at High Polymer Concentrations," vol. 9, pp. 165–172, June 1975.

[148] A. Vrij, "Polymers at Interfaces and the Interactions in Colloidal Dispersions," *Pure and Applied Chemistry*, vol. 48, pp. 471–483, Jan. 1976.

[149] J. C. Crocker, J. A. Matteo, A. D. Dinsmore, and A. G. Yodh, "Entropic Attraction and Repulsion in Binary Colloids Probed with a Line Optical Tweezer," *Physical Review Letters*, vol. 82, pp. 4352–4355, May 1999.

[150] R. Roth, R. Evans, and S. Dietrich, "Depletion potential in hard-sphere mixtures: theory and applications," *Physical Review E*, vol. 62, pp. 5360–5377, May 2000.

[151] J. N. Israelachvili, "Intermolecular and surface forces: with applications to colloidal and biological systems (Colloid Science)," *London: Academic*, 1992.

[152] M. A. Bevan and D. C. Prieve, "Direct Measurement of Retarded van der Waals Attraction," *Langmuir*, vol. 15, pp. 7925–7936, Nov. 1999.

[153] H.-J. Butt, B. Cappella, and M. Kappl, "Force measurements with the atomic force microscope: Technique, interpretation and applications," *Surface Science Reports*, vol. 59, pp. 1–152, Oct. 2005.

[154] C. R. Iacovella, R. E. Rogers, S. C. Glotzer, and M. J. Solomon, "Pair interaction potentials of colloids by extrapolation of confocal microscopy measurements of collective suspension structure," *The Journal of chemical physics*, vol. 133, Oct. 2010.

[155] B. Götzelmann, R. Evans, and S. Dietrich, "Depletion forces in fluids," *Physical Review E*, vol. 57, pp. 6785–6800, June 1998.

[156] J. Baumgartl, R. P. A. Dullens, M. Dijkstra, R. Roth, and C. Bechinger, "Experimental Observation of Structural Crossover in Binary Mixtures of Colloidal Hard Spheres," *Physical Review Letters*, vol. 98, May 2007.

[157] E. R. Dufresne, T. M. Squires, M. P. Brenner, and D. G. Grier, "Hydrodynamic Coupling of Two Brownian Spheres to a Planar Surface," *Phys. Rev. Lett.*, vol. 85, pp. 3317–3320, Oct. 2000.

[158] D. Roy, D. Mondal, and D. Goswami, "Structure and dynamics of optically directed self-assembly of nanoparticles," *Scientific Reports*, vol. 6, pp. 23318+, Mar. 2016.

[159] A. Ashkin, "Forces of a single-beam gradient laser trap on a dielectric sphere in the ray optics regime," *Biophysical Journal*, vol. 61, pp. 569–582, Feb. 1992.

[160] M. Padgett and R. Bowman, "Tweezers with a twist," *Nature Photonics*, vol. 5, pp. 343–348, May 2011.

[161] S.-H. Lee and D. G. Grier, "Giant Colloidal Diffusivity on Corrugated Optical Vortices," *Physical Review Letters*, vol. 96, pp. 190601+, May 2006.

[162] J. Mikhael, J. Roth, L. Helden, and C. Bechinger, "Archimedean-like tiling on decagonal quasicrystalline surfaces," *Nature*, vol. 454, pp. 501–504, July 2008.

[163] Y. Liu, K. V. Edmond, A. Curran, C. Bryant, B. Peng, D. G. A. L. Aarts, S. Sacanna, and R. P. A. Dullens, "Core-Shell Particles for Simultaneous 3D Imaging and Optical Tweezing in Dense Colloidal Materials," *Adv. Mater.*, pp. 8001–8006, July 2016.

[164] A. Imhof, "Preparation and Characterization of Titania-Coated Polystyrene Spheres and Hollow Titania Shells," *Langmuir*, vol. 17, pp. 3579–3585, June 2001.

[165] J. Brandrup, E. H. Immergut, E. A. Grulke, A. Abe, and D. R. Bloch, *Polymer handbook*, vol. 7. Wiley New York etc, 1989.

# List of publications

To date the following publications based upon work in this thesis have been submitted or are in preparation:

Y. Liu, K.V. Edmond, A. Curran, T. Yanagishima, D.G.A.L. Aarts, S. Sacanna, and R.P.A. Dullens, *Colloidal TPM particles for three-dimensional confocal microscopy*, In preparation (Chapter 3 and 5)

Y. Liu, K.V. Edmond, A. Curran, C. Bryant, B. Peng, D.G.A.L. Aarts, S. Sacanna, and R.P.A. Dullens, *Core-Shell Particles for Simultaneous 3D Imaging and Optical Tweezing in Dense Colloidal Materials*, Adv. Mater. **28**, 36, (2016) (Chapters 3 and 4).

C. Bryant, A. Curran, Y. Liu, P.D.J Van Oostrum, D.G.A.L. Aarts, A. Van Blaaderen, B. Peng, and R.P.A. Dullens, *Melamine-Folmaldehyde colloidal particles: Synthesis, Characterisation and coating with TPM for optical tweezing*, In preparation (Chapter 4)

B. Peng, Y. Liu, and R.P.A. Dullens, *Discontinuously protecting hollow colloidal $TiO_2$: shells towards durably efficient photocatalysts*, In preparation (Chapter 4 and 6)

Y. Liu, A. Curran, A. Balin, D.G.A.L. Aarts, and R.P.A. Dullens, *Dynamics of driven optically anisotropic dumbbells*, In preparation (Chapter 6)

# Acknowledgements

This DPhil has been an incredible journey. I am very grateful to Roel for giving me the chance to prove myself as a soft matter scientist, and for his steady support and good dose of common sense over the last four years. I have been incredibly lucky to have had the chance to live and work in New York for a month during this time, for which I am also grateful for Stefano for hosting me in his lab. I was also very fortunate to have my work recognised at an international soft matter conference in Grenoble, a process which has taught me a lot about myself and the wider world. These would not have been possible without the much needed help and insight from Roel. Thank you.

I would like to thank Dirk for his serious scientific inputs as well as for his more light hearted comments, especially on the eternal struggle between Matlab and Mathematica. Aside from these two great scientists that I have been working alongside everyday, I have also met a number of other famous 'soft matter' people on the way. Yet these things pale in comparison to all the wonderful colleagues and friends from the Oxford Colloid group. In particular, I want to thank Arran for his patience and expertise on all things optical, François for his humour and in-depth knowledge of Matlab, Taiki for his input on soft matter physics, Bo for advice on colloidal chemistry, and Raam, Colin, Josh, Louis and the others for their generosity and friendship.

My final thanks go to my dear parents, who have taught me the value of hard work and perseverance in the face of challenges. Words cannot express sufficiently my gratitude, and so I woruld like to dedicate this work in their honour.